The Pennsylvania State University

The Graduate School

Department of Materials Science and Engineering

THEORETICAL STUDIES OF ALUMINUM AND ALUMINIDE ALLOYS USING CALPHAD AND FIRST-PRINCIPLES APPROACH

A Thesis in

Materials Science and Engineering

by

Chao Jiang

Submitted in Partial Fulfillment
of the Requirements
for the Degree of

Doctor of Philosophy

August 2004

The thesis of Chao Jiang has been reviewed and approved* by the following:

Zi-Kui Liu
Associate Professor of Materials Science and Engineering
Thesis Advisor
Chair of Committee

Long-Qing Chen
Professor of Materials Science and Engineering

Jorge O. Sofo
Associate Professor of Physics

Robert C. Voigt
Professor of Industrial & Manufacturing Engineering

Gary Messing
Distinguished Professor of Ceramic Science and Engineering
Head of the Department of Materials Science and Engineering

*Signatures are on file in the Graduate School.

ABSTRACT

Heat-treatable aluminum alloys have been widely used in the automobile and aerospace industries as structural materials due to their light weight and high strength. To study the age-hardening process in heat-treatable aluminum alloys, the Gibbs energies of the strengthening metastable phases, e.g. θ′ and θ″, are critical. However, those data are not included in the existing thermodynamic databases for aluminum alloys due to the semi-empirical nature of the CALPHAD approach. In the present study, the thermodynamics of the Al-Cu system, the pivotal age-hardening system, is remodeled using a combined CALPHAD and first-principles approach. The formation enthalpies and vibrational formation entropies of the stable and metastable phases in the Al-Cu system are provided by first-principles calculations. Special Quasirandom Structures (SQS's) are applied to model the substitutionally random fcc and bcc alloys. SQS's for binary bcc alloys are developed and tested in the present study. Finally, a self-consistent thermodynamic description of the Al-Cu system including the two metastable θ″ and θ′ phases is obtained.

During welding of heat-treatable aluminum alloys, a detrimental phenomenon called constitutional liquation, i.e. the local eutectic melting of second-phase particles in a matrix at temperatures above the eutectic temperature but below the solidus of the alloy, may occur in the heat-affected zone (HAZ). In the present study, diffusion code DICTRA coupled with realistic thermodynamic and kinetic databases is used to simulate the constitutional liquation in the model Al-Cu system. The simulated results are in

quantitative agreement with experiments. The critical heating rate to avoid constitutional liquation is also determined through computer simulations.

Besides the heat-treatable aluminum alloys, intermetallic compounds based on transition metal aluminides, e.g. NiAl and FeAl, are also promising candidates for the next-generation of high-temperature structural materials for aerospace applications due to their high melting temperature and good oxidation resistance. Many important properties of B2 aluminides are governed by the existences of point defects. In the present study, Special Quasirandom Structures (SQS's) are developed to model non-stoichiometric B2 compounds containing large concentrations of constitutional point defects. The SQS's are then applied to study B2 NiAl. The first-principles SQS results provide formation enthalpies, equilibrium lattice parameters and elastic constants of B2 NiAl which agree satisfactorily with the existing experimental data in the literature. It is unambiguously shown that, at T=0K and zero pressure, Ni vacancies and antisite Ni atoms are the energetically favorable point defects in Al-rich and Ni-rich B2 NiAl, respectively. Remarkably, it is predicted that high defect concentrations can lead to structural instability of B2 NiAl, which explains well the martensitic transformation observed in this compound at high Ni concentrations.

TABLE OF CONTENTS

LIST OF FIGURES

LIST OF TABLES

ACKNOWLEDGEMENTS

First of all, I wish to express my sincere gratitude to my advisor, Dr. Zi-Kui Liu, for his close guidance during my five-year Ph.D. study at Penn State. I also wish to thank Dr. Long-Qing Chen, Dr. Jorge O. Sofo and Dr. Robert C. Voigt for their help and encouragement, and serving in my thesis committee.

Special thanks need to be given to Dr. Chris Wolverton of Ford Research Laboratory for his many help to me during my Ph.D. research.

I would also take the opportunity to thank all members of the Phases Research Lab, as well as the faculty and staff of the Materials Science and Engineering department, for their help to me during the my stay at Penn State.

Finally, I would like to thank my family, my wife and my parents, for their constant encouragement and invaluable support without which this thesis could not have come true.

Chapter 1. INTRODUCTION

1.1. Background

1.1.1. Heat-Treatable Aluminum Alloys

Aluminum is the second most plentiful metallic element on earth. Due to its low density ($2.70 g/cm^3$), aluminum alloys have been widely used in the automobile and aerospace industries as light-weight high-strength structural materials. Although pure aluminum is too soft and weak for structural applications, the strength of aluminum alloys can be greatly enhanced by a process called age or precipitation hardening.

During age hardening, the aluminum alloy containing small amounts of other strengthening elements, e.g. Cu, Zn or Mg, is first homogenized into a single-phase fcc solid solution at a high temperature. This is followed by a rapid quenching to room temperature, which produces a supersaturated fcc solid solution. The alloy is then isothermally aged either at room temperature (natural aging) or at elevated temperatures (artificial aging) for a certain amount of time in order to attain its maximum strength. The strengthening of the alloy is due to the formation of a fine dispersion of metastable precipitates from the supersaturated Al matrix. Coherent or semi-coherent precipitates have the maximum strengthening effect since their surrounding strain field can interfere with the motion of dislocations. Due to the large number of thermal vacancies quenched

from high temperatures, the age hardening process is greatly accelerated and can occur at low temperatures.

Al-Cu has a pivotal role as the prototype age hardening system in the development of heat-treatable aluminum alloys. Historically, age hardening was first accidentally discovered in the Al-Cu system. However, the reason was not elucidated until in 1938 Guinier [1] and Preston [2] independently discovered the existence of Guinier-Preston (GP) zones. There are actually two types of GP zones, namely GP-I and GP-II. As illustrated in Figure 1.1, during the age hardening of Al-Cu alloys, the precipitation process usually starts with the formation of GP-I zones, a monolayer of pure Cu atoms on the {100} plane of the Al matrix. The GP-I zones are fully coherent with the Al matrix and therefore have the lowest nucleation barrier. With longer aging time, the GP-I zones will gradually transform into its more thermodynamically stable form, namely GP-II zones, or θ″ (Al_3Cu). θ″ is actually two layers of Cu atoms separated by three layers of Al atoms (Cu/Al/Al/Al/Cu) and is also fully coherent with the Al matrix. Wolverton [3] recently found that GP-I and GP-II zones are *not* thermodynamically distinct phases, but rather the GP-I to GP-II transition is merely due to a size-effect: the critical size for GP-I zones is about 150Å, beyond which they will change into GP-II zones. With even longer aging time, θ″ will then evolve into semi-coherent θ′ (Al_2Cu) and eventually the equilibrium non-coherent θ (Al_2Cu).

During the welding of many commercial heat-treatable aluminum alloys, the strengthening precipitates such as θ′ may however lead to severe heat-affected zone

(HAZ) damage, which makes HAZ the weakest link in the weldment. One possible reason for such loss of strength is due to the dissolution or coarsening of the strengthening precipitates in the HAZ. However, much more severely, due to the rapid heating and cooling rate experienced during normal welding operations, liquid may form in the HAZ due to the local melting of those precipitates. This process is called constitutional liquation as proposed by Pepe and Savage [4]. The liquid formed by constitutional liquation may spread along the grain boundaries through the intersection of grain boundaries with the liquated regions in the matrix. This may lead to intergranular HAZ hot cracking during welding due to the inability of the intergranular liquid films to sustain thermal stresses within the weldment. The solidified liquid may also embrittle the grain boundaries and lead to intergranular fracture and cold cracking during service. Interestingly, the absence of strengthening precipitates in the non-heat-treatable aluminum alloys, which prevents them from achieving the same high strength as the heat-treatable aluminum alloys, turns out to be an advantageous factor when considering weldability. The HAZ damage incurred during welding of non-heat-treatable aluminum alloys is much less severe and reasonable joint strengths can be obtained in the as-welded condition without the need for post-weld heat treatment.

1.1.2. B2 Aluminides

Besides the heat-treatable aluminum alloys, intermetallic compounds based on transition metal aluminides, e.g. NiAl and FeAl, have also recently attracted much attention. Those intermetallic compounds possess excellent properties such as low density, high melting

temperature and good oxidation resistance, making them promising candidates for the next-generation of high-temperature structural materials for aerospace applications [5-7]. Compared with the currently used Ni-based superalloys, NiAl has a lower density, higher thermal conductivity and an over 200°C higher melting temperature. NiAl has an ordered CsCl-type B2 structure consisting of two interpenetrating simple cubic sublattices. In the perfectly ordered state at the 50/50 stoichiometric composition, the two sublattices are entirely occupied by Al atoms and Ni atoms, respectively. Deviations from the ideal stoichiometry are accommodated by the existences of constitutional point defects. The point defect structure of NiAl is known to be of triple-defect type, i.e. Al-rich NiAl is accommodated by the formation of Ni vacancies while Ni-rich NiAl is accommodated by the formation of antisite Ni atoms [8].

The existences of point defects in B2 compounds are of great technological importance. It is now well established that many important properties of B2 compounds, e.g. mechanical properties and diffusion mechanisms, are largely dependent on the types and concentrations of those point defects [9-11]. A full knowledge of those point defects is therefore essential for the development of B2 aluminides. Unfortunately, direct experimental determination of the concentrations of those point defects, e.g. using positron annihilation method [6], is still difficult and the results are often quite controversial [12]. This is partly due to the difficulty in creating an “ideal” homogeneous sample. In view of this, it is highly desirable to investigate them using first-principles approach.

1.1.3. Computational Materials Science

In the development of alloys with better properties to meet today's increasingly demanding applications, the traditional experimental trial-and-error approach becomes more and more insufficient. This is due to the fact that most commercial alloys are multi-component in nature and may contain as many as 10 alloying elements. It is impractical to explore such a high dimensional composition space by experimental means. Fortunately, with the rapidly increasing computing power we have, it is now possible to use computers to predict the properties of alloys without the need to do experiments.

Based on computational thermodynamics, the CALPHAD (CALculation of Phase Diagrams) [13] approach has been very successful in modeling phase equilibria and phase transformations in complex multi-component alloys. Commercial computer programs like Thermo-Calc [14] and DICTRA [15] have been widely used for such purposes and sophisticated thermodynamic and kinetic databases have also been developed using the CALPHAD approach.

Recent advances in *ab-initio* or first-principles calculations based on the density functional theory (DFT) [16] have made it possible to predict from scratch the various thermodynamic and structural properties of alloys. Combined with the cluster expansion technique [17, 18], alloy phase diagrams can also be calculated by performing Monte-Carlo simulations [19, 20]. These methods are truly predictive since only the atomic numbers and crystal structure information are needed as the inputs. Actually the word

"*ab-initio*" means "from beginning". Nevertheless, at the present stage, there still exist several limitations that hinder the straightforward applications of the first-principles approach to the design of alloys:

1) Despite its importance in determining finite-temperature phase stabilities [21], first-principles calculations of vibrational entropies, e.g. using the linear-response theory [22], are still very computationally demanding. Even so, other contributions to entropy may also exist, such as configurational and electronic excitation. Calculating all of these contributions and considering the coupling between them is an even more challenging task.

2) When treating fully ordered compounds, the capability of first-principles calculations is only limited by the total number of atoms in one unit cell and not by the number of constituents in the compound. However, when treating multi-component disordered phases, e.g. solution phases and compounds showing homogeneity ranges, due to the "combinatorial explosion", it is not computationally tractable in the foreseeable future to directly use first-principles calculations to treat those phases.

3) Although the cluster expansion technique has been developed to treat the disordered phases, it is typically only applied to binary systems with very simple underlying lattices, e.g. fcc and bcc. It is currently not directly applicable to describe more complicated multi-component phases.

4) Even though a recent comparison between first-principles calculated formation enthalpies and those in existing COST 507 [23] thermodynamic database demonstrates that the accuracy of first-principles calculations is within a few kJ/mol, first-principles calculations still do not have the accuracy required to predict phase diagrams to within a few degrees to meet the industrial's needs. This is due to the fact that, the energy difference between two competing phases is actually only a tiny fraction of their total energies.

1.2. Research Objectives and Thesis Outline

In heat-treatable aluminum alloys, the thermodynamically stable phases, e.g. θ, are of no interest for industrial applications. It is the metastable phases, e.g. θ″ and θ′, which actually contribute to the improvement of the mechanical properties of the aluminum alloys. However, due to its semi-empirical nature, the CALPHAD method alone can not treat metastable phases simply due to insufficient experimental data. As the consequence, the Gibbs energies of those metastable phases are not included in the existing thermodynamic databases for aluminum alloys, e.g. COST 507 [23]. To study the age-hardening process in aluminum alloys, those data are however critical. Although θ′ has been incorporated into the existing COST 507 database in a straightforward way by Wolverton *et al.* [24], doing so for θ″ is not possible as COST 507 database predicts a metastable fcc miscibility gap thermodynamically more stable than θ″, as shown in Figure 1.2. In the present study, a thermodynamic modeling of the Al-Cu system will be performed using a combined CALPHAD and first-principles approach. In Chapter 4,

first-principles calculations are performed to provide the formation enthalpies of the stable and metastable phases in Al-Cu system. Special Quasirandom Structures (SQS's) are applied to model the substitutionally random fcc and bcc alloys (SQS's for binary bcc alloys are developed and tested in Chapter 3). Those SQS's are rather general and can be applied to study other systems as well. A self-consistent thermodynamic description of the Al-Cu system including the two metastable θ″ and θ′ phases is obtained in Chapter 5.

Due to its detrimental effect during welding of heat-treatable aluminum alloys, constitutional liquation in the model Al-Cu system will also be studied. In Chapter 6, using the DICTRA program coupled with realistic thermodynamic and kinetic databases, all stages of the constitutional liquation are quantitatively simulated. The critical heating rate to avoid constitutional liquation is obtained through computer simulations. The computational procedures developed in the present study is rather general and can be readily extended to predict the susceptibility of commercial multi-component aluminum alloys to constitutional liquation during welding.

Finally, due to their technological importance, SQS's will also be developed in the present study to model non-stoichiometric B2 compounds containing large concentrations of constitutional point defects. In Chapter 7, such SQS's are developed and employed to investigate the point defects in B2 NiAl. It is unambiguously shown that, at T=0K and zero pressure, Ni vacancies and antisite Ni atoms are the energetically favorable point defects in Al-rich and Ni-rich B2 NiAl, respectively. The predicted formation enthalpies, equilibrium lattice parameters and elastic constants of non-stoichiometric B2 NiAl are in

good agreement with experiments. Remarkably, it is found that high defect concentrations can lead to structural instability of B2 NiAl, which explains well the martensitic transformation observed in this compound at high Ni concentrations. Since the SQS's are rather general, they can be applied to study other B2 alloys as well.

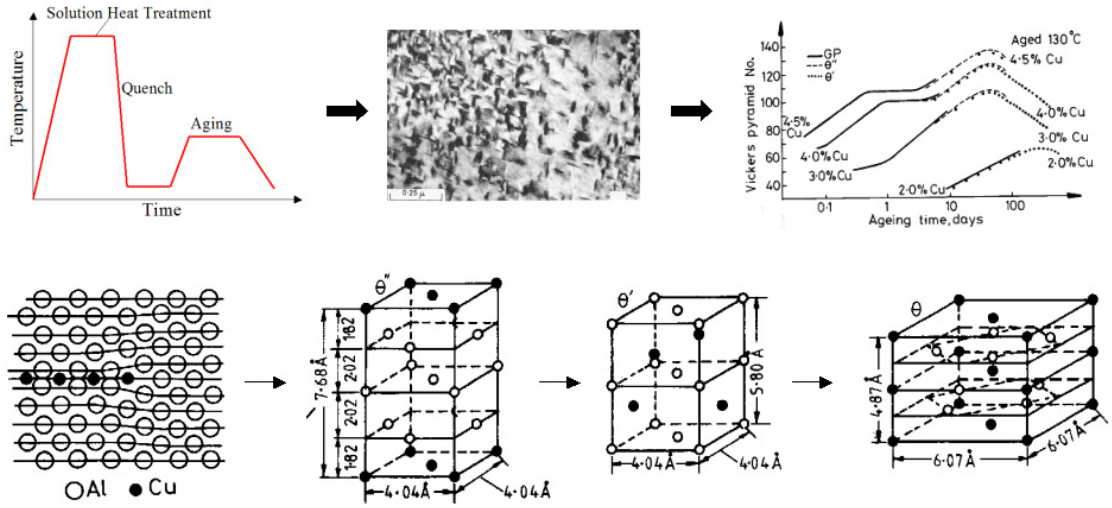

Figure 1.1. The age-hardening process in Al-Cu alloys [25].

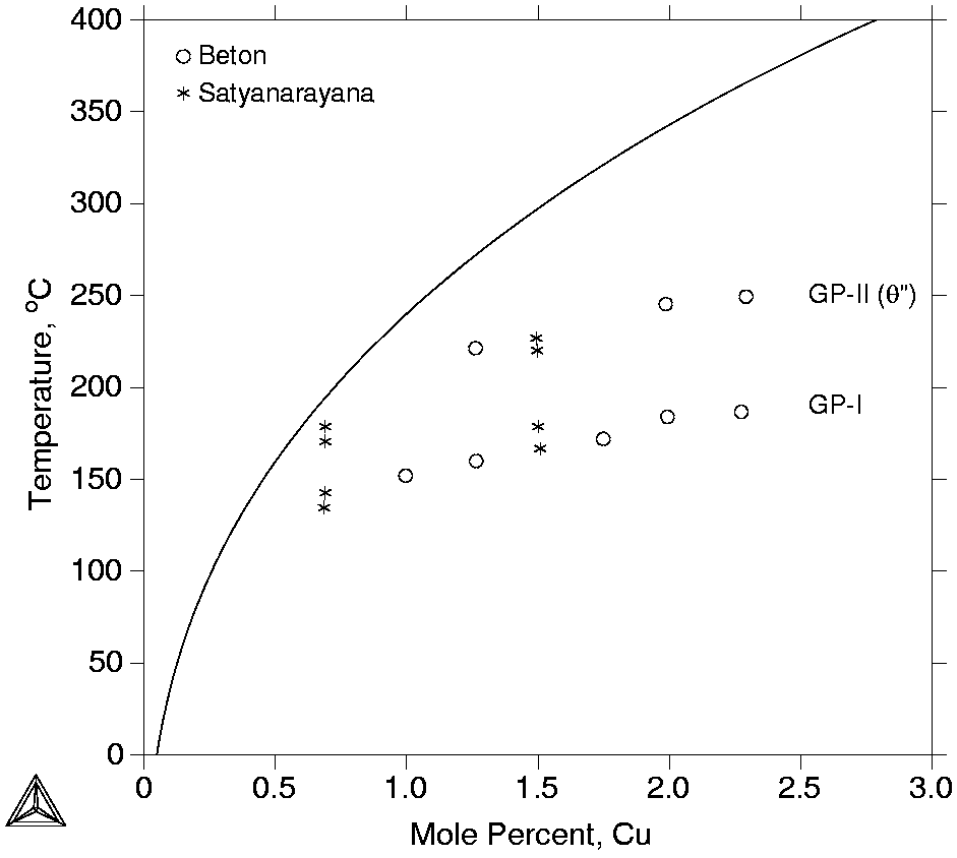

Figure 1.2. The metastable fcc miscibility gap calculated using the COST 507 database. The experimental solvus data from Beton and Rollason [26] and Satyanarayana *et al.* [27] are also shown.

Chapter 2. METHODOLOGY

2.1. The CALPHAD Approach

Phase diagrams are visual representations of the equilibrium state of a system as a function of composition, temperature and pressure. They are the "roadmap" for alloys design. Nevertheless, experimental determinations of phase diagrams are both expensive and time-consuming. The CALPHAD approach was introduced by Kaufman [13] to model the complex phase equilibria in multi-component alloys. Its theoretical basis is computational thermodynamics: given the Gibbs energies of all the competing phases in a system, the final equilibrium state at a given composition, temperature and pressure can be calculated by minimizing the total Gibbs energy of the system:

$$G = \sum_p n_p G_p = \min \tag{2.1}$$

where n_p is the number of moles of phase p and G_p is its Gibbs energy. By keeping the stable phases from appearing, metastable phase equilibrium can also be calculated.

In the CALPHAD approach, different thermodynamic models are used to describe different types of phases. The Gibbs energies of pure elements in their stable, metastable or even unstable states, the so-called "lattice-stabilities", are taken from the SGTE pure element database [28]. The reference state is chosen to be the enthalpies of the pure elements in their stable states at 298.15K, commonly referred to as Standard Element

Reference (SER). For stoichiometric compounds with negligible homogeneity ranges, when experimental heat capacity data are available, it is preferable to express their Gibbs energies directly referred to the SER as follows:

$$^{\circ}G_m^{A_{1-x}B_x} - (1-x)H_A^{SER} - xH_B^{SER} = a + bT + cT\ln(T) + dT^2 + \cdots \quad (2.2)$$

where the coefficients *c* and *d* are related to heat capacity as $C_p = -c - 2dT + \cdots$. For compounds with no heat capacity data, assuming the Neumann-Kopp rule holds, i.e. $\Delta C_p = 0$, their Gibbs energies can be expressed as:

$$^{\circ}G_m^{A_{1-x}B_x} = (1-x)^{\circ}G_A^{\Phi_A} + x^{\circ}G_B^{\Phi_B} + a + bT \quad (2.3)$$

where $^{\circ}G_i^{\Phi}$ is the molar Gibbs energy of pure element *i* in structure Φ, *a* and *b* are the enthalpy and entropy of formation of the compound with respect to A and B in structure Φ_A and Φ_B, respectively.

For solution phases such as liquid, fcc and bcc, the substitutional solution model is usually used. Taking a binary A-B solution phase Φ for example, its Gibbs energy is written as:

$$G_m^{\Phi} = G^{ref} + G^{ideal} + G^{excess} \quad (2.4)$$

where $G^{ref} = x_A {}^{\circ}G_A^{\Phi} + x_B {}^{\circ}G_B^{\Phi}$ is the Gibbs energy of mechnical mixture of pure elements A and B, both in structure Φ. G^{ideal} denotes the contribution from configurational entropy of mixing. Assuming random mixing of A and B atoms on a lattice and neglecting short-range ordering (SRO), G^{ideal} can be treated by the Bragg-Williams approximation as:

$$G^{ideal} = -TS^{ideal} = RT\left(x_A \ln x_A + x_B \ln x_B\right) \tag{2.5}$$

The excess term G^{excess} is used to characterize the deviation of real alloys from the ideal solution behaviour, which is usually expressed as a Redlich-Kister [29] polynomial:

$$G^{excess} = x_A x_B \sum_{k=0}^{n} {}^{k}L_{A,B}^{\Phi}\left(x_A - x_B\right)^k \tag{2.6}$$

where ${}^{k}L_{A,B}^{\Phi}$ is the k_{th} interaction parameter between the A and B atoms and can be temperature-dependent in the form ${}^{k}L_{A,B}^{\Phi} = a_k + b_k T + c_k T \ln T$. a_k, b_k and c_k are model parameters to be evaluated from experimental data.

To model complex phases containing multiple sublattices, the compound energy formalism (CEF) [30] is usually used. As an example, to model the A2→B2 order-disorder transformation in a binary A-B system, a $(A,B)_{0.5}(A,B)_{0.5}$ two-sublattice model will be used. Its Gibbs energy per mole of formula units can be written in the same form as Eq. (2.4):

$$G_m^{B2} = G^{ref} + G^{ideal} + G^{excess} \tag{2.7}$$

Now the first term G^{ref} represents the contributions from all its four end-members:

$$G^{ref} = y_A^I y_A^{II} {}^\circ G_{A:A} + y_A^I y_B^{II} {}^\circ G_{A:B} + y_B^I y_A^{II} {}^\circ G_{B:A} + y_B^I y_B^{II} {}^\circ G_{B:B} \tag{2.8}$$

where y_i^I and y_i^{II} are the site fractions of element i on the first and second sublattices, respectively. ${}^\circ G_{i:j}$ is the Gibbs energy of the compound with the first sublattice entirely occupied by element *i* and the second entirely by *j*, be it real or hypothetical. The second term represents contribution from configurational entropy, treated by the the Bragg-Williams approximation assuming random mixing inside each sublattice:

$$G^{ideal} = 0.5RT(y_A^I \ln y_A^I + y_B^I \ln y_B^I) + 0.5RT(y_A^{II} \ln y_A^{II} + y_B^{II} \ln y_B^{II}) \tag{2.9}$$

Finally, the third term represents the contribution due to interactions within the same sublattice:

$$G_m^{B_2} = y_A^I y_B^I (y_A^{II} L_{A,B:A} + y_B^{II} L_{A,B:B}) + y_A^{II} y_B^{II} (y_A^I L_{A:A,B} + y_B^I L_{B:A,B}) \tag{2.10}$$

L's are the interaction parameters and can be both composition and temperature dependent in the Redlich-Kister [29] form (see Eq. (2.6)).

As illustrated in Figure 2.1, the development of thermodynamic databases using the CALPHAD approach is usually carried out in the following four steps:

1) Do an exhaustive search for all available experimental data, e.g. thermochemical and phase equilibrium ones, of the system to be studied. When experimental data are insufficient, first-principles results can be used as if they are experiments.

2) Critically assess the validity of each piece of data and assign it a certain weight according to its experimental uncertainty and relative importance.

3) Based on the crystal structure information, choose a suitable thermodynamic model to represent each of the phases in the system. Those models generally include some unknown phenomenological model parameters that need to be determined.

4) Adjust all the unknown model parameters to obtain the best possible fit between model calculations and experimental data.

The final obtained model parameters are stored in computerized databases. Once the Gibbs energies of all the constituent subsystems have been assessed, those data can be extrapolated to predict phase equilibria in higher-order systems.

2.2. First Principles Calculations

2.2.1. Fundamentals

A solid can be thought of as a collection of interacting positively charged nuclei and negatively charged electrons. Theoretically, an exact treatment of solids can be obtained by solving the following many-body Schrödinger's equation involving both the nuclei and the electrons:

$$\hat{H}\Psi(\vec{R}_1,\vec{R}_2,...\vec{R}_N,\vec{r}_1,\vec{r}_2,...\vec{r}_n) = E\Psi(\vec{R}_1,\vec{R}_2,...\vec{R}_N,\vec{r}_1,\vec{r}_2,...\vec{r}_n) \tag{2.11}$$

where R_I's are the nuclei coordinates, r_i's are the electron coordinates, $\hat{H}$ is the Hamiltonian operator, E is the total energy of the system, N is the total number of nuclei and n is the total number of electrons in the system. However, although theoretically exact, it is extremely difficult to solve Eq. (2.11) due to its many-body nature. In fact, the only system that can be solved analytically is the single-electron hydrogen atom. In general, the Schrödinger's equation has to be solved numerically. In the following, several levels of approximations will be introduced.

2.2.1.1. Born-Oppenheimer Approximation

Since the nuclei are much heavier than the electrons, it can be assumed that the electrons are always in instantaneous ground state with the nuclei. In other words, we can fix the

positions of the nuclei and only solve the many-body Schrödinger's equation for the electrons:

$$\hat{H}\Psi(\vec{r}_1,\vec{r}_2,...\vec{r}_n) = E\Psi(\vec{r}_1,\vec{r}_2,...\vec{r}_n) \tag{2.12}$$

Since the nuclei are "frozen", they only contribute to an external potential for the electrons.

2.2.1.2. Density Functional Theory

Even after the simplification by the Born-Oppenheimer approximation, the Schrödinger's equation in essence is still a many-body problem due to the interactions between electrons: each electron will interact with every other electron in the system. Most modern electronic calculations for solids are based on the density functional theory (DFT) proposed by Kohn and Sham [16]. According to DFT, the total energy of a system can be uniquely defined by the electron charge density, i.e. $E = E[\rho(\vec{r})]$. The original many-electron Schrödinger's equation is then converted into a set of one-electron Schrödinger's equations, one for each electron in the system:

$$\left[-\frac{\hbar^2}{2m_e}\nabla_i^2 - \frac{e^2}{4\pi\varepsilon_0}\sum_{I=1}^{N}\frac{Z_I}{\left|\vec{r}-\vec{R}_I\right|} + \frac{e^2}{4\pi\varepsilon_0}\int\frac{\rho(\vec{r}')}{\left|\vec{r}-\vec{r}'\right|}d^3\vec{r}' + V_{XC}[\rho(\vec{r})]\right]\psi_i(\vec{r}) = \varepsilon_i\psi_i(\vec{r}) \tag{2.13}$$

The exchange correlation potential $V_{XC}[\rho(\vec{r})]$ is given by the functional derivative:

$$V_{XC}[\rho(\vec{r})] = \frac{\delta}{\delta\rho(\vec{r})} E_{XC}[\rho(\vec{r})] \tag{2.14}$$

Nevertheless, the exact form of the exchange correlation energy $E_{XC}[\rho(\vec{r})]$ is unknown. The most widely used approximation is the so-called Local Density Approximation (LDA), which assumes that the exchange correlation energy $E_{XC}[\rho(\vec{r})]$ is only a function of the local charge density in the form:

$$E_{XC}[\rho(\vec{r})] = \int \rho(\vec{r}) \varepsilon_{XC}[\rho(\vec{r})] d^3\vec{r} \tag{2.15}$$

where $\varepsilon_{XC}[\rho(\vec{r})]$ is the exchange-correlation energy of homogeneous electron gas of the same charge density. LDA is expected to work well for systems with a slowly varying charge density, but surprisingly, LDA works quite well for realistic systems as well.

One significant limitation of LDA is its overbinding of solids: lattice parameters are usually underpredicted while cohesive energies are usually overpredicted. In an effort to rectify the inaccuracies of LDA, the Generalized Gradient Approximation (GGA) was introduced. GGA is a natural improvement on LDA by considering not only the local charge density, but also its gradient. The lattice parameters calculated by GGA generally agree noticeably better with experiments than LDA. It is worth noting here that, there is only one LDA exchange correlation functional, i.e. the one by Ceperley and Alder [31,

32]. Nevertheless, there exist many versions of GGA due to the freedom in how to incorporate the gradient term in the exchange correlation energy.

The actual first-principles total energy calculations are performed in a self-consistent cycle. We first "guess" the initial charge density function. By solving Eq. (2.13), a new charge density is obtained. This loop is repeated until the new charge density (or the new total energy) does not differ much from the old one, i.e. the iteration has converged. In practice, the nuclei also need to be relaxed into their equilibrium positions such that the quantum-mechanical forces acting on each of them vanish. Such structural relaxations are usually performed using a conjugate-gradient or a quasi-newton scheme. The final obtained total energies can be used to extract the formation enthalpies of stable, metastable or even unstable structures at T=0K using the following equation:

$$\Delta H(A_{1-x}B_x) = E(A_{1-x}B_x) - (1-x)E(A) - xE(B) \tag{2.16}$$

where *E*'s are the first-principles calculated total energies of structure $A_{1-x}B_x$ and pure elements A and B, each fully relaxed to their equilibrium (zero-pressure) geometries, respectively.

2.2.2. Treating Disordered Alloys

Since first-principles DFT calculations rely on the construction of cells with periodic boundary conditions, the calculations are fairly straightforward for perfectly-ordered

stoichiometric compounds. However, the situation is more complicated when treating disordered alloys.

2.2.2.1. Cluster Expansions

For a binary $A_{1-x}B_x$ substitutional alloy, many properties such as energy are dependent on the *configuration*, or the substitutional arrangement of A and B atoms on the lattice. The configuration dependence of properties can be characterized very efficiently by a "lattice algebra" [17, 18, 33-35]. As illustrated in Figure 2.2, the actual substitutional configuration of a binary $A_{1-x}B_x$ alloy is mapped into an Ising-like lattice model: A atoms are represented by the "down" spins (S_i=-1) and B atoms are represented by the "up" spins (S_i=+1). For a binary $A_{1-x}B_x$ alloy with N atoms, there can be 2^N possible number of configurations, which is an astronomically large number when N is large. It is an impossible task to explore such a huge configuration space, even with today's fastest supercomputer. Fortunately, using the cluster expansion technique, the total energy of any alloy configuration (S_1, S_2,…, S_n) can be conveniently calculated using the following Ising-like Hamiltonian:

$$E(S_1, S_2, \cdots, S_N) = J_0 + \sum_i J_i S_i + \sum_{i,j} J_{ij} S_i S_j + \sum_{i,j,k} J_{ijk} S_i S_j S_k + \cdots \qquad (2.17)$$

where J's are the so-called effective cluster interactions (ECI's). Taking into consider the symmetry of the underlying lattice, Eq. (2.17) can be rewritten in the following more compact form:

$$E(S_1, S_2, \cdots, S_N) = \sum_f D_f J_f \left\langle \prod_{i \in f} S_i \right\rangle = \sum_f D_f J_f \overline{\Pi}_f \tag{2.18}$$

where figures *f* are symmetry-related groupings of lattice sites, e.g., single site, nearest-neighbor pair, three-body figures, etc. These figures, *f*=(*k*, *m*) can have *k* vertices and span a maximum distance of *m* (*m*=1, 2, 3… are the first, second and third-nearest neighbors, etc.). D_f denotes the degeneracy factor of figure *f*. $\overline{\Pi}_f$ is the so-called correlation function defined as the product of the spin variable over all sites of a figure, averaging over all symmetry-equivalent figures of the lattice. The expansion in Eq. (2.18) is exact as long as *all* the figures are included. However, since the interactions between widely separated atoms are expected to be weaker than the interactions between nearer atoms, the expansion in Eq. (2.18) is usually truncated at certain distance to include only a few short-ranged pair and multisite clusters.

In practice, as illustrated in Figure 2.3, the total energies of a few (30~50) pre-selected ordered structures based on a common underlying parent lattice are first calculated by some first-principles code like VASP. Those total energies are then used to fit all the unknown pair and multi-body ECI's. Subjecting the cluster expansions to Monte-Carlo simulations, thermodynamic properties, e.g. formation enthalpies, of the alloys over the whole composition range can be efficiently obtained.

2.2.2.2. Mead-Field Approach

The coherent potential approximation [36] (CPA) treats random $A_{1-x}B_x$ alloys by considering the *average* occupations of lattice sites by A and B atoms. Since it is a mean-field approach, dependence of properties on the *local* environments surrounding atoms is not treated explicitly in CPA. However, in a real (non-mean-field) random alloy, there exists a distribution of local environments (e.g., A or B surrounded by the various A_mB_{8-m} coordination shells with *m* between 0 and 8 in bcc alloys), resulting in local environmentally-dependent quantities such as charge transfer and local displacements of atoms from their ideal lattice positions [34, 35, 37-39]. Experimental observations [40] also show that, even in random $A_{1-x}B_x$ solid solutions, the average A-A, A-B and B-B bond lengths are generally different. In size-mismatched semiconductor alloys, such local atomic relaxations have been shown to significantly affect their thermodynamic and electronic properties [34, 35, 37, 38].

2.2.2.3. Special Quasirandom Structures (SQS's)

The third way to treat random $A_{1-x}B_x$ solid solutions would be to directly construct a large supercell and randomly decorate the host lattice with A and B atoms. Such an approach would necessarily require very large supercells to adequately mimic the statistics of the random alloys. Since density functional methods are computationally constrained by the number of atoms that one can treat, this brute-force approach could be computationally prohibitive. The concept of special quasirandom structures (SQS's) was

proposed by Zunger *et al.* [34, 35, 41] to overcome the limitations of mean-field theories, but without the prohibitive computational cost associated with directly constructing large supercells with random occupancy of atoms. SQS's are specially designed *small-unit-cell* periodic structures with only a few (2~32) atoms per unit cell, which closely mimic the most relevant, near-neighbor pair and multisite correlation functions of the random substitutional alloys. Since the SQS approach is not a mean-field one, a distribution of distinct local environments is maintained, the average of which corresponds to the random alloy. Thus, a single DFT calculation of an SQS can give many important alloy properties [34, 35, 41] (e.g. equilibrium bond lengths, charge transfer, formation enthalpies, etc.) which depend on the existence of those distinct local environments. Furthermore, since the SQS approach is geared towards relatively small-unit-cells, essentially any DFT method can be applied to this approach, including full-potential methods capable of accurately capturing the effects of atomic relaxation.

The advantage of the SQS approach is that, in order to obtain a fully converged cluster expansion for a given alloy, the energies of about 30~50 ordered structures have to be obtained in their fully relaxed geometries, which is still a quite laborious task. In contrast, using SQS's, only one *single* calculation is required to obtain the various properties of a random alloy. The SQS approach has been used extensively to study the formation enthalpies, bond length distributions, density of states, band gaps and optical properties in semiconductor alloys [34, 35, 41]. They have also been applied to investigate the local lattice relaxations in size-mismatched transition metal alloys [37-39, 42] and to predict the formation enthalpies of Al-based fcc alloys [43]. However, to date, all the

applications of the SQS methodology are for systems in which the substitutional alloy problem is fcc-based (e.g., fcc-based metals, zinc-blende-based semiconductors, or rock-salt-based oxides). No SQS's for the bcc structure exist in the literature. Therefore, in Chapter 3, SQS's will be developed for binary bcc alloys at compositions x=0.25, 0.50 and 0.75, respectively. Since these SQS's are quite general, they can be applied to any binary bcc alloy.

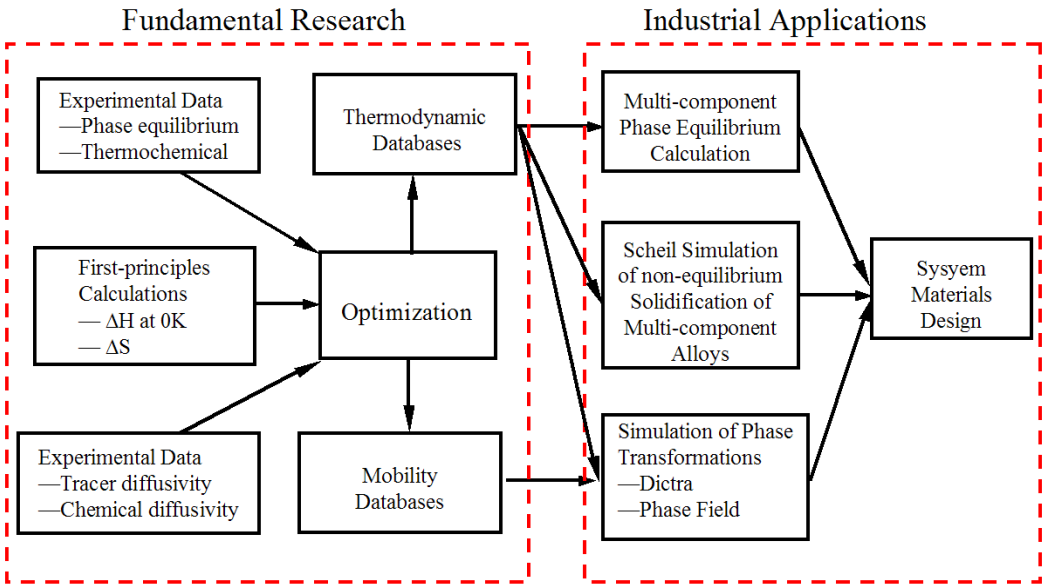

Figure 2.1. Thermodynamic database development using CALPHAD.

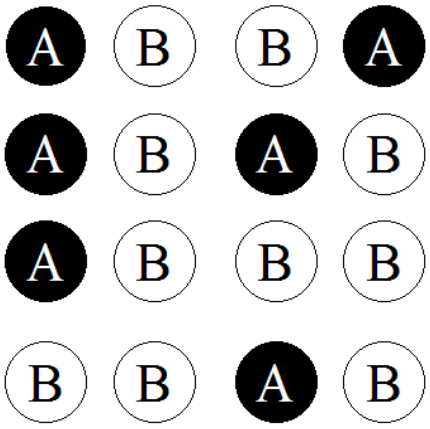

(a) Alloy configuration

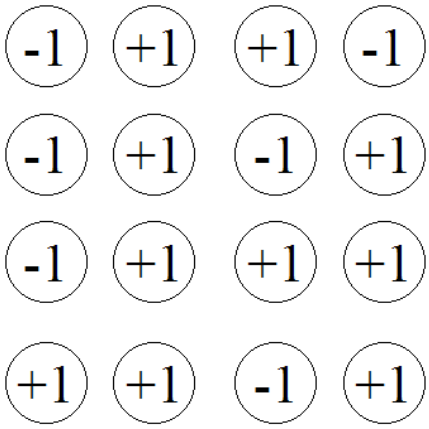

(b) Lattice model

Figure 2.2. Mapping substitutional $A_{1-x}B_x$ alloy into a Ising-like lattice model.

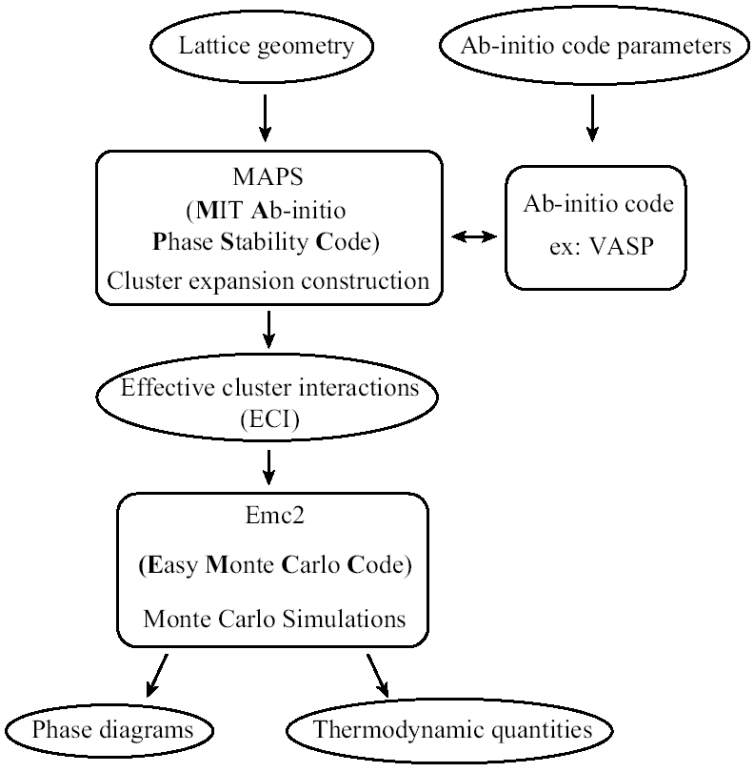

Figure 2.3. The flowchart of Alloy-Theoretic Automated Toolkit (ATAT) [20, 44].

Chapter 3. SPECIAL QUASIRANDOM STRUCTURES FOR BINARY BCC ALLOYS

3.1. Theoretical Basis of SQS's

For the perfectly random $A_{1-x}B_x$ bcc alloys, there is no correlation in the occupation between various sites, and therefore correlation function $\overline{\Pi}_{k,m}$ simply becomes the product of the lattice-averaged site variable, which is related to the composition by $< S_i > = 2x-1$. Thus, for the perfectly random alloy, the pair and multisite correlation functions $\overline{\Pi}_{k,m}$ are given quite simply as:

$$\left\langle \overline{\Pi}_{k,m} \right\rangle_R = (2x-1)^k \tag{3.1}$$

The SQS approach amounts to finding small-unit-cell ordered structures that possess $\left(\overline{\Pi}_{k,m}\right)_{SQS} \cong \left\langle \overline{\Pi}_{k,m} \right\rangle_R$ for as many figures as possible. Admittedly, describing random alloys by small unit-cell periodically-repeated structures will surely introduce erroneous correlations beyond a certain distance. However, as already mentioned, since interactions between nearest neighbors are generally more important than interactions between more distant neighbors, the SQS's can be constructed in such as way that they exactly reproduce the correlation functions of a random alloy between the first few nearest neighbors, deferring errors due to periodicity to more distant neighbors.

3.2. Generation of the SQS's

In the present study, various SQS-*N* structures (with *N*=2, 4, 8 and 16 atoms per unit cell) are generated for the random bcc alloys at composition *x*=0.50 and 0.75 using the *gensqs* code in ATAT [20, 44]. For each composition *x*, the procedure can be described as follows:

1) Using *gensqs,* exhaustively generate all structures based on the bcc lattice with *N* atoms per unit cell and composition *x*.

2) Construct the pair and multisite correlation functions $\overline{\Pi}_{k,m}$ for each structure.

3) Finally, search for the structure(s) that best match the correlation functions of random alloys over a specified set of pair and multisite figures.

The SQS-16 structure for *x*=0.5 is obtained by requiring that its pair correlation functions be identical to those of the random alloy up to the fifth-nearest neighbor. Nevertheless, for *x*=0.75, no SQS-16 structures satisfy this criterion. Therefore, we instead choose a structure whose pair correlation functions are identical to the random alloy up to the fourth-nearest neighbor. The other SQS-*N* structures with *N*=2, 4 and 8 atoms per unit cell are generated using an analogous approach. Of course, in general, the smaller the unit cell, the fewer pair correlations that match those of the random alloy.

The lattice vectors and atomic positions of the obtained SQS-*N* structures in their ideal, unrelaxed forms are given in Table 3.1, all in Cartesian coordinates. The definitions of the multisite figures considered here are given in Table 3.2. In Table 3.3, the pair and multisite correlation functions of the SQS-*N* structures presented in Table 3.1 are compared with those of the corresponding random alloys. We also give an estimate of the errors due to periodicity, estimated as $\sum_{m=1}^{4}(\overline{\Pi}_{2,m} - (2x-1)^2)^2$, over the first four neighbor pairs. These errors are also shown in Table 3.3, and they rapidly decrease with increasing *N*. We note that the SQS-*N* structures for x=0.25 are obtained simply by switching the A and B atoms in SQS-*N* for x=0.75. Since this amounts to replacing all of the spin variables by $S_i \rightarrow -S_i$, all even-body correlations are equivalent for x=0.25 and x=0.75, while all odd-body correlations simply change sign. Thus, the three-body figures are largely responsible for asymmetries in the formation energies between x=0.25 and x=0.75.

In all calculations in the present study, unless specifically noted, we use the 16-atom SQS's to represent the random bcc alloys. The extent to which they match the random alloy correlations is comparable to those of the existing 16-atom SQS's for the fcc structure (see Appendix A), which reproduce the pair correlation functions of perfectly random fcc alloys accurately up to the seventh-nearest neighbor at x=0.5 and third-nearest neighbor at x=0.75 [43]. SQS-16 for x=0.5 is a triclinic-type structure with space group $P\bar{1}$ (space group No. 2 in the International Tables of Crystallography), and SQS-16 for x=0.75 is a monoclinic-type structure with space group Cm (space group No. 8 in

the International Tables of Crystallography) [45]. Their pictures are also given in Figure 3.1 in their ideal, unrelaxed forms.

3.3. Testing the SQS's

In this section, the qualities of the obtained SQS's are tested via first-principles calculations in the bcc-forming Mo-Nb, Ta-W and Cr-Fe systems, in which the bcc solid solution is observed to be stable over the whole composition range. The predicted formation enthalpies, equilibrium lattice parameters and magnetic moments of these bcc alloys are then compared with the existing experimental data in the literature. The convergence of the SQS's and the effects of local atomic relaxations are also studied.

3.3.1. First-Principles Method

First-principles calculations are performed using the plane wave method with Vanderbilt ultrasoft pseudopotentials [46, 47], as implemented in the highly-efficient Vienna *ab initio* simulation package (VASP) [48, 49]. The generalized gradient approximation (GGA) [50] is used since we have included Cr-Fe in our list of systems to test the SQS's: The local density approximation (LDA) is known to incorrectly predict the ground state of Fe to be a non-magnetic close-packed phase, whereas GGA calculations correctly predict the ground state to be the ferromagnetic bcc phase [51]. The *k*-point meshes for Brillouin zone sampling are constructed using the Monkhorst–Pack scheme [52] and the total number of *k*-points times the total number of atoms per unit cell is at least 6000 for

all systems. A plane wave cutoff energy E_{cut} of 233.1, 235.2 and 296.9 eV are used for Mo-Nb, Ta-W and Cr-Fe system, respectively. All calculations include scalar relativistic corrections (i.e., no spin-orbit interaction).

Spin-polarized calculations are performed for the Cr-Fe alloys, whereas all other calculations are nonmagnetic. Pure bcc Fe is ferromagnetic while pure bcc Cr is antiferromagnetic with incommensurate spin density waves [53]. This leads to a quite complicated magnetic structure in the $Cr_{1-x}Fe_x$ bcc alloys at low temperatures [54], which will not be investigated in the present study. Instead, since our SQS calculations are performed at compositions x=0.25, 0.5 and 0.75, all larger than the critical composition x=0.2 beyond which the $Cr_{1-x}Fe_x$ bcc alloy becomes ferromagnetic [55], we assume a ferromagnetic structure for the Cr-Fe bcc alloys in our spin-polarized calculations.

By computing the quantum-mechanical forces and stress tensor, structural and atomic relaxations are performed and all atoms are relaxed into their equilibrium positions using a conjugate-gradient scheme. For the bcc alloys considered in the present study, the SQS's are fully relaxed with respect to both the volume and shape of the unit cell as well as all the atomic positions. In all our calculations, the magnitudes of cell vector distortions of the fully relaxed SQS's with respect to their ideal, unrelaxed unit cells are very small, indicating structural stability of the bcc lattice for these systems.

The formation enthalpies of the random bcc alloys are obtained as:

$$\Delta H(x) = E(A_{1-x}B_x) - (1-x)E(A) - xE(B) \quad (3.2)$$

where E(A), E(B), and E($A_{1-x}B_x$) are the first-principles calculated total energies of the constituent pure elements A and B and the corresponding SQS, respectively, each relaxed to their equilibrium geometries. In the present study, all elements considered are observed at low temperature in the bcc structure, and thus, pure element bcc energies are used as reference states in Eq. (3.2).

To study the local atomic relaxations, the distributions of nearest neighbor bond lengths in the random bcc alloys were also obtained from the relaxed SQS's. Since in a perfect bcc structure each atom is coordinated by eight nearest neighbors, we have taken the smallest eight interatomic distances of each atom in the relaxed SQS's to be representative of the nearest neighbor bonds.We then categorized the bond distances into different bond types, e.g. A-A, A-B and B-B, and computed the average bond lengths for each type.

3.3.2. Pure Elements

The first-principles calculated T=0K lattice parameters of bcc Nb, Mo, Ta, W, Cr and Fe, each relaxed to their equilibrium volumes, are given in Table 3.4. Both spin-polarized and non-spin-polarized calculations are performed for bcc Cr and Fe. Consistent with previous DFT studies, ferromagnetism substantially stabilizes the bcc Fe (energy is decreased by ~0.56 eV/atom upon inclusion of spin polarization), making it the ground

state of Fe. Spin-polarized, ferromagnetic calculations for Cr resulted in a non-magnetic solution. According to Table 3.4, the lattice mismatch (defined as $\Delta a/\overline{a}$) in the Mo-Nb, Ta-W, and Cr-Fe alloy systems are found to be 4.3%, 3.7% and 0%, respectively.

3.3.3. Mo-Nb Bcc Alloys

Mo and Nb form a continuous bcc solid solution. No intermediate phases have been reported in this system [56]. The equilibrium lattice parameters of Mo-Nb bcc alloys obtained from the relaxed SQS's are plotted in Figure 3.2 together with those of the pure bcc Mo and Nb given in Table 3.4. The experimental measurements by Goldschmidt and Brand [57] and Catterall and Barker [58] are also included for comparison. Our calculations are in good agreement with experiments. Both show a small negative deviation from the Vegard's law, i.e.

$$a(A_{1-x}B_x) = (1-x)a(A) + xa(B) \tag{3.3}$$

where $a(A_{1-x}B_x)$, $a(A)$ and $a(B)$ are the equilibrium lattice parameter of alloy $A_{1-x}B_x$ and constituent pure elements A and B, respectively. In Figure 3.3, the predicted formation enthalpies of random Mo-Nb bcc alloys are compared with the experimental measurements by Singhal and Worrell [56] at 1200K using a solid state galvanic cell. Fairly satisfactorily agreement has been reached with the largest discrepancy less than 2kJ/mol. Sigli *et al.* [59] also calculated the formation enthalpies of Mo-Nb bcc alloys using the TB-CPA-GPM approach. For the purpose of comparison, their results are also

show in Figure 3.3, which agree quite well with our SQS's results. In all three cases, the asymmetry of the formation enthalpy with respect to x=0.50 is quite small.

The negative formation enthalpies indicate that Mo-Nb is an ordering-type system. Sigli *et al.* [59] predicted that an ordered B2 structure is stable in Mo-Nb below 830K. Neglecting the effects of vibrational entropy and assuming ideal configurational entropy of mixing for the $Mo_{1-x}Nb_x$ bcc solid solution, i.e.:

$$\Delta S_{ideal} = -R\big(x\ln(x) + (1-x)\ln(1-x)\big) \tag{3.4}$$

We obtain a crude estimate the A2-B2 order-disorder transition temperature at composition x=0.5 in Mo-Nb using the following equation:

$$T_c \approx \frac{\Delta H_{bcc}^{SQS}(x=0.5) - \Delta H_{B2}}{R\ln 2} \tag{3.5}$$

Our first-principles calculation of the formation enthalpy of the fully ordered MoNb B2 structure gives –13.1 kJ/mol. Using Eq. (3.5), we thus obtain Tc≈731K, in good agreement with the temperature of 830K predicted by Sigli *et al.* [59] Since this temperature is relatively low compared with the melting temperature of Mo (2896K) and Nb (2750K), sluggish kinetics might explain why the B2 structure or other ordered phases have not been observed experimentally. However, our results do predict the existence of ordered structures in Mo-Nb which to date, have not yet been observed.

Therefore, we assert that experimental re-examination of the low-temperature phase stability of Mo-Nb would be of interest.

3.3.4. Ta-W Bcc Alloys

Ta and W also form a continuous bcc solid solution with no intermediate phases [60]. The predicted equilibrium lattice parameters of Ta-W bcc alloys are shown in Figure 3.4, in good agreement with the existing experimental measurements [61]. Both show a negative deviation from the Vegard's law. In Figure 3.5, the predicted formation enthalpies of random Ta-W bcc alloys are compared with the experimental solid state galvanic cell measurements of Singhal and Worrell [60]. In Figure 3.4 and Figure 3.5 we also show the formation enthalpies of random Ta-W bcc alloys calculated by Turchi *et al.* [62] using the TB-LMTO-ASA-CPA approach. Interestingly, although experimental formation enthalpies exhibit a strong asymmetry towards the Ta-rich side, both SQS and CPA calculated formation enthalpies exhibit a strong asymmetry towards the W-rich side. Such large discrepancies between our calculations and experimental measurements on the W-rich side may be due to the slow kinetics at the experimental temperature of 1200K, which makes thermodynamic equilibrium difficult to reach, as was also pointed out by Turchi *et al.* [62] To ascertain this, we examined the tracer diffusivity of Ta in bcc W at 1200K using the Arrhenius relation obtained by Arkhipova *et al.* [63]:

$$D_{Ta}^{W} = 6.2 \times 10^{-4} Exp(-601241/RT) \tag{3.6}$$

and we obtained an extremely low value of 4.186×10^{-30} m^2/s. The fact that D_{Ta}^{W} dominates the interdiffusion coefficients in the W-rich Ta-W bcc alloys could explain why the discrepancies between SQS calculations and experiments are largest on the W-rich side. However, we should also note other possibilities to explain this discrepancy:

1) Our SQS are constructed to mimic the perfectly random state, and thus short-range order in these alloys could also contribute to the discrepancy.

2) Although the SQS possess many pair and multi-body correlations that match the random alloy statistics, there are deviations from the random alloy correlations for longer-ranged pair and other multi-body interactions. If some of these interactions are significant, they could contribute to the discrepancy.

3) Finally, we should note that experimental measurements of formation enthalpies down to an accuracy of 1 kJ/mol are quite difficult, and it is possible that the experimental data is partly responsible for the discrepancy.

It is interesting that the results of Turchi *et al.* [62] overestimate the formation enthalpies relative to our SQS results even though their CPA calculations ignore such important physical effects as atomic relaxations, which will lower the formation enthalpy. We attribute such apparent discrepancies to the atomic sphere approximation (ASA) employed in their CPA calculations.

The negative formation enthalpies indicate that Ta-W is also an ordering-type system. Turchi *et al.* [62] predicted that the Ta-W bcc alloys have a strong tendency toward B2 ordering. In the present study, we obtained via first-principles calculations the formation enthalpy of the fully ordered TaW B2 structure to be –11.2 kJ/mol. Assuming ideal configurational entropy of mixing, the A2-B2 order-disorder transition temperature at composition x=0.5 in Ta-W is thus estimated using Eq. (3.5) to be Tc≈552K, which is substantially lower than the temperatures predicted by Turchi *et al.* [62]. The low order-disorder transition temperature could again explain why the B2 structure has not been observed experimentally in Ta-W. But again, our calculations predict the (low temperature) existence of ordered structures in the Ta-W system that have previously not been reported, and therefore future experimental work on this system would be of interest.

3.3.5. Cr-Fe Bcc Alloys

Cr and Fe form a continuous bcc solid solution with a miscibility gap appearing at low temperatures [64]. A sigma phase also forms at intermediate temperatures [64]. In Figure 3.6, the predicted equilibrium lattice parameters of ferromagnetic Cr-Fe bcc alloys are compared with available experiments [65]. Figure 3.7 also gives the predicted magnetic moments (in μ_B per atom) of random ferromagnetic Cr-Fe bcc alloys together with the available experiments [66, 67] and the calculated KKR-CPA results by Kulikov and Demangeat [68]. In both cases, the discrepancies near the Cr corner are due to the fact that we treat Cr as ferromagnetic instead of antiferromagnetic. In Figure 3.6, we also

include our calculated equilibrium lattice parameter of antiferromagnetic bcc Cr with a commensurate wave vector using a B2 unit cell, which is in good agreement with the measured value. We found that antiferromagnetism lowers the energy of bcc Cr by ~0.046 eV/atom.

Dench [69] experimentally measured the formation enthalpies of bcc Cr-Fe alloys at 1400K. This temperature is well above the Curie (or Néel) temperature of Cr-Fe bcc alloys [64], therefore, the measured alloys are all in the paramagnetic state. However, the present spin-polarized calculations correspond to the ferromagnetic state of the alloys. Akai and Dederichs [70] and Olsson *et al.* [71] calculated using the KKR-CPA and FCD-EMTO-CPA approach, respectively, the structural energy differences between the paramagnetic and ferromagnetic states of random Cr-Fe bcc alloys, $\Delta E^{FM\to PM}$, which are found to be substantial in the Cr-Fe system. In both studies, the disordered local moment (DLM) model was used, which treats the paramagnetic $Cr_{1-x}Fe_x$ alloy as a random quaternary $(Cr\uparrow,Cr\downarrow)_{1-x}(Fe\uparrow,Fe\downarrow)_x$ system with equal number of up-spin and down-spin atoms. Since the Cr-Fe system is a perfectly lattice-matched system with $\Delta a/\bar{a}$ <1%, one might expect that the atomic relaxations are small, and that the neglect of them in the CPA should represent only a minor approximation. We will investigate more the relaxation behavior of this alloy below.

Figure 3.8 shows the CPA calculated formation enthalpy difference between the paramagnetic and ferromagnetic states of Cr-Fe bcc alloys [70, 71] defined as:

$$\Delta H^{FM\to PM}(x) = \Delta E^{FM\to PM}(A_{1-x}B_x) - (1-x)\Delta E^{FM\to PM}(A) - x\Delta E^{FM\to PM}(B) \quad (3.7)$$

By adding $\Delta H^{FM\to PM}$ to our SQS calculated formation enthalpies of ferromagnetic Cr-Fe bcc alloys, we obtain the formation enthalpy in the paramagnetic state. Our results are shown in Figure 3.9 together with the corresponding experimental data [69] and the CPA DLM results by Olsson *et al.* [71]. We find good agreement between the theoretical and experimental formation enthalpies with the largest discrepancy less than 1kJ/mol. We also note that the positive formation enthalpy for the random alloy is normally an indication of (but does not guarantee) a phase-separating tendency in this system, consistent with the observed miscibility gap [64].

Non-spin-polarized calculations are also performed on the present SQS's, which, however, predicted the wrong sign of the formation enthalpies, as shown in Figure 3.9. Thus, we can conclude that the non-magnetic calculations are a particularly poor representation of the paramagnetic state for these alloys.

3.3.6. Convergence of SQS's

Figure 3.10 gives the formation enthalpies of various SQS-*N* structures for x=0.5 with N=2, 4, 8 and 16 atoms per unit cell, respectively. For all three systems considered in the present study, we observed a rapid convergence of the SQS calculated formation enthalpies with respect to N. Remarkably, in Mo-Nb and Ta-W, even calculations on SQS-2 predicted well within 1kJ/mol the results obtained using SQS-16. From Table 3.3,

we see that even the SQS-2 has a nearest-neighbor correlation which matches that of the random alloy precisely. Thus, the rapid convergence of SQS-*N* with respect to *N* in for Mo-Nb and Ta-W could be an indication that the energetics of these alloy systems are dominated by nearest-neighbor pair interactions. In Cr-Fe, the convergence is still rapid, though somewhat less so, possibly due to the magnetic effects. Similar rapid convergence behavior of the fcc SQS's were also observed by Zunger *et al.* [34, 35].

3.3.7. Bond Lengths in Random Bcc Alloys

In Figure 3.11, the average nearest neighbor A-A, A-B and B-B bond lengths in random Mo-Nb, Ta-W and Cr-Fe bcc alloys are presented. In all systems, our results clearly show three distinct nearest neighbor bond lengths R_{A-A}, R_{A-B} and R_{B-B} at all compositions, all deviating from that of the average lattice, i.e. $R = \sqrt{3}/2\, a$, a being the equilibrium lattice parameter of the alloy. Nevertheless, the weighted average of these bond lengths, i.e. $x_A^2 R_{A-A} + 2x_A x_B R_{A-B} + x_B^2 R_{B-B}$, do follow R, as shown by the dashed lines in Figure 3.11. In the Mo-Nb and Ta-W systems, the bond lengths follow the "expected" behavior in that the bonds between unlike atoms are intermediate between the large-large and small-small like atom bonds.

However, the relaxation behavior of Cr-Fe is somewhat unexpected: Even though the Cr-Fe system is a perfectly lattice-matched system, the average Cr-Cr, Cr-Fe and Fe-Fe bond lengths are actually quite different. Thus, in this system, the atomic relaxation is not simply mediated by traditional atomic size mismatch considerations, but must also have a

contribution due to electronic or band structure effects. We see that a small lattice-mismatch does not necessarily guarantee small atomic relaxation, as is often asserted. We find the average Cr-Fe bond length to be larger than those of both Cr-Cr and Fe-Fe bonds. To further investigate this issue, we also give in Figure 3.12 the predicted nearest neighbor bond length distributions in Cr-Fe bcc alloys. The horizontal lines correspond to the average bcc lattice. As shown, there exists a dispersion of bond lengths for all three types of bonds, i.e. Cr-Cr, Cr-Fe and Fe-Fe, indicating the existence of local lattice relaxations. This unusual structural behavior of the Cr-Fe bcc alloys is interesting in light of the phase-separating tendency in this system: a miscibility gap is experimentally observed in this system at low temperatures [64].

3.4. Summary

In this chapter, three 16-atom SQS supercells are proposed to mimic the pair and multisite correlation functions of random binary bcc substitutional alloys at compositions x=0.25, 0.50 and 0.75, respectively. In each of them, a distribution of distinct local environments is created, the average of which corresponds to the random alloy. Those SQS's are then applied to predict the lattice parameters, formation enthalpies, magnetic moments and bond lengths of Mo-Nb, Ta-W and Cr-Fe bcc alloys, and the results are in good agreement with the experimental data in the literature, when available. The magnetic effects were found to be significant in Cr-Fe, and a combination of our ferromagnetic SQS calculations with previous calculations on the paramagnetic state result in formation energies that agree well with experimental measurements. The

convergence tests showed that 16-atom SQS's provide good approximations of the real random solutions, and even very small 2-atom SQS's provide reasonably accurate energetics. Thus, this two-atom structure could be used as a very simple "screen" for bcc random alloy energetics. The calculated nearest neighbor bond lengths showed that, even in perfectly lattice-matched systems such as Cr-Fe, the average A-A, A-B and B-B bond lengths can be quite different. Since the presently proposed SQS's are quite general, they can be applied to other binary bcc alloys.

Table 3.1. Structural descriptions of the SQS-*N* structures. Lattice vectors and atomic positions are given in Cartesian coordinates, in units of a, the bcc lattice parameter. Atomic positions are given for the ideal, unrelaxed bcc sites.

	x=0.5	x=0.75
SQS-16	Lattice vectors $\vec{a}_1$=(-0.5, -1.5, -2.5), $\vec{a}_2$=(-0.5, 2.5, 1.5) $\vec{a}_3$=(1.5, 0.5, -0.5) Atomic positions A - (0.0, 0.0, -2.0), A - (0.5, 1.5, -0.5) A - (1.0, 0.0, -2.0), A - (0.5, 0.5, -0.5) A - (0.5, -0.5, -2.5), A - (-0.5, 1.5, -0.5) A - (0.0, 2.0, 0.0), A - (0.5, 2.5, 0.5) B - (1.0, 2.0, 0.0), B - (-0.5, 0.5, -1.5) B - (1.0, 1.0, -1.0), B - (0.0, 1.0, 0.0) B - (0.5, 1.5, -1.5), B - (0.0, 1.0, -1.0) B - (0.0, 0.0, -1.0), B - (0.5, 0.5, -1.5)	Lattice vectors $\vec{a}_1$=(1.0, -2.0, 0.0), $\vec{a}_2$=(0.0, -2.0, 1.0) $\vec{a}_3$=(-2.0, 0.0, -2.0) Atomic positions A - (0.0, -4.0, 0.0), A - (0.0, -2.0, 0.0) A - (0.5, -2.5, 0.5), A - (0.5, -3.5, 0.5) B - (-1.5, -0.5, -1.5), B - (-1.5, -1.5, -1.5) B - (-1.0, -1.0, -1.0), B - (-0.5, -0.5, -0.5) B - (-1.0, -4.0, -1.0), B - (-1.0, -2.0, -1.0) B - (-0.5, -1.5, -0.5), B - (0.0, -1.0, 0.0) B - (-1.0, -3.0, -1.0), B - (-0.5, -2.5, -0.5) B - (-0.5, -3.5, -0.5), B - (0.0, -3.0, 0.0)
SQS-8	$\vec{a}_1$=(0.5, 0.5, -1.5), $\vec{a}_2$=(1.5, 0.5, -0.5) $\vec{a}_3$=(0.0, -2.0, 0.0) A - (2.0, 0.0, -2.0), A - (0.5, -1.5, -0.5) A - (1.0, -1.0, -1.0), A - (1.5, -0.5, -1.5) B - (2.0, -1.0, -2.0), B - (0.5, -0.5, -0.5) B - (1.0, 0.0, -1.0), B - (1.5, 0.5, -1.5)	$\vec{a}_1$=(-1.0, 0.0, 0.0), $\vec{a}_2$=(0.0, 1.0, -1.0) $\vec{a}_3$=(0.0, -2.0, -2.0) A - (-0.5, -0.5, -1.5), A - (-1.0, -1.0, -2.0) B - (-0.5, -1.5, -2.5), B - (-0.5, 0.5, -1.5) B - (-1.0, -1.0, -3.0), B - (-1.0, 0.0, -1.0) B - (-0.5, -0.5, -2.5), B - (-1.0, 0.0, -2.0)
SQS-4	$\vec{a}_1$=(-0.5, 0.5, 0.5), $\vec{a}_2$=(0.0, -1.0, 1.0) $\vec{a}_3$=(1.5, 0.5, 0.5) A - (0.5, -0.5, 1.5), A - (1.0, 0.0, 1.0) B - (0.0, 0.0, 1.0), B - (1.0, 0.0, 2.0)	$\vec{a}_1$=(-0.5, 0.5, 0.5), $\vec{a}_2$=(0.0, -1.0, 1.0) $\vec{a}_3$=(1.5, 0.5, 0.5) A - (1.0, 0.0, 1.0), B - (0.0, 0.0, 1.0) B - (1.0, 0.0, 2.0), B - (0.5, -0.5, 1.5)
SQS-2	$\vec{a}_1$=(-0.5, 0.5, -0.5), $\vec{a}_2$=(-0.5, -0.5, 0.5) $\vec{a}_3$=(0.0, 1.0, 1.0) A - (-1.0, 1.0, 1.0), B - (-0.5, 0.5, 0.5)	

Table 3.2. Vertices of the multisite figures, given in units of a, the bcc lattice parameter.

Type	Figure designation	Vertices			
Triplets	(3,2)	(0, 0, 0)	(0.5, 0.5, 0.5)	(0.5, -0.5, 0.5)	
	(3,3)	(0, 0, 0)	(0.5, 0.5, 0.5)	(1, 0, 1)	
Quadruplets	(4,2)	(0, 0, 0)	(0.5, 0.5, 0.5)	(0.5, -0.5, 0.5)	(1, 0, 0)

Table 3.3. Pair and multisite correlation functions of SQS-*N* structures. The number in the square brackets next to $\overline{\Pi}_{k,m}$ gives the degeneracy factor of the corresponding figure.

	x=0.5					x=0.75			
	Random	SQS-16	SQS-8	SQS-4	SQS-2	Random	SQS-16	SQS-8	SQS-4
$\overline{\Pi}_{2,1}$ [4]	0	0	0	0	0	0.25	0.25	0.25	0.25
$\overline{\Pi}_{2,2}$ [3]	0	0	0	-0.3333	-0.3333	0.25	0.25	0.3333	0
$\overline{\Pi}_{2,3}$ [6]	0	0	-0.1667	0	-0.3333	0.25	0.25	0.1667	0.1667
$\overline{\Pi}_{2,4}$ [12]	0	0	0	0	0	0.25	0.25	0.25	0.25
$\overline{\Pi}_{2,5}$ [4]	0	0	-0.5	0	1	0.25	0.125	0.5	0.5
$\overline{\Pi}_{2,6}$ [3]	0	-0.3333	0.3333	-0.3333	1	0.25	0.0833	0.3333	0.3333
$\overline{\Pi}_{2,7}$ [12]	0	0	0	0	0	0.25	0.25	0.25	0.25
$\overline{\Pi}_{3,2}$ [12]	0	0	0	0	0	0.125	0.1667	0.1667	0
$\overline{\Pi}_{3,3}$ [12]	0	0	0	0	0	0.125	0.0833	0.1667	0.1667
$\overline{\Pi}_{4,2}$ [6]	0	0	-0.3333	-0.3333	-0.3333	0.0625	0.1667	0	0
Error	0	0	0.0278	0.1111	0.2222	0	0	0.0139	0.0694

Table 3.4. First principles (VASP-GGA) calculated equilibrium lattice parameter for pure elements in the bcc structure. Spin-polarized calculations were performed for Cr and Fe in their ferromagnetic (FM) state.

Element	Mo	Nb	Ta	W	Cr (FM)	Fe (FM)
a (Å)	3.15	3.29	3.29	3.17	2.85	2.85

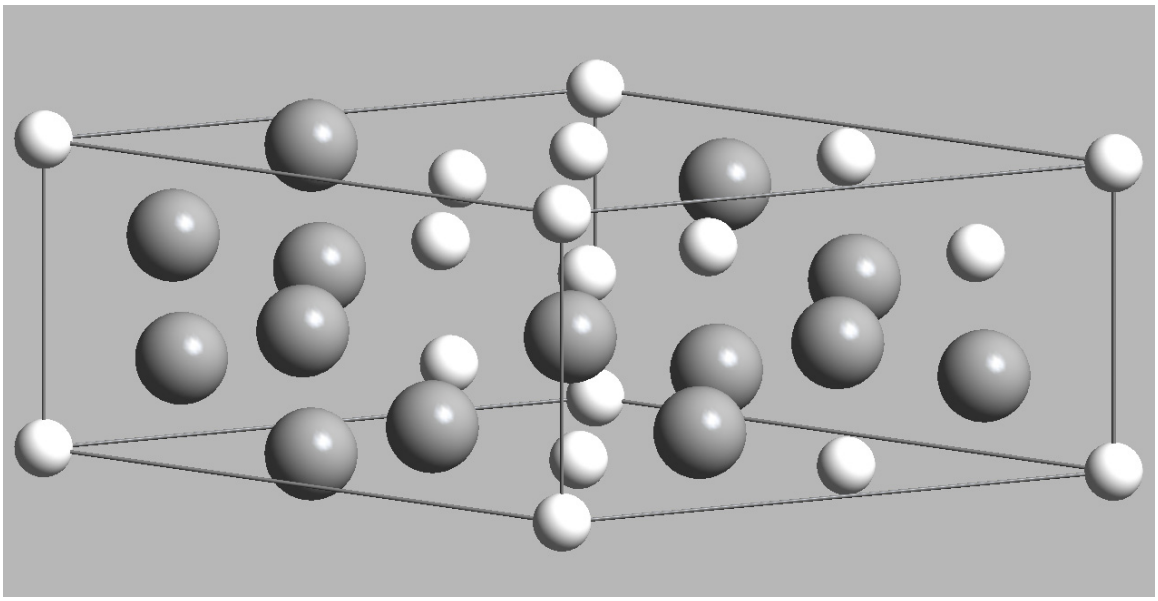

(a) SQS-16 for x=0.5

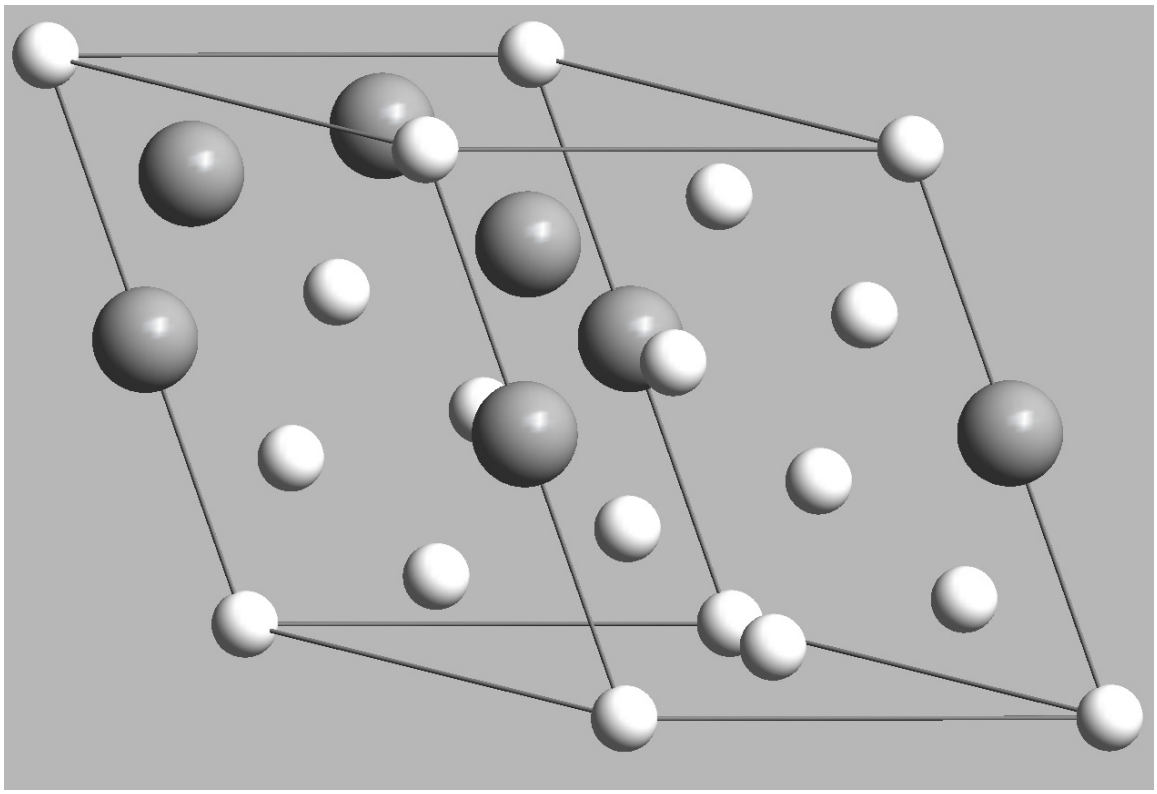

(b) SQS-16 for x=0.75

Figure 3.1. Crystal structure of the SQS-16 structures in their ideal, unrelaxed forms. Dark and light spheres represent A and B atoms, respectively.

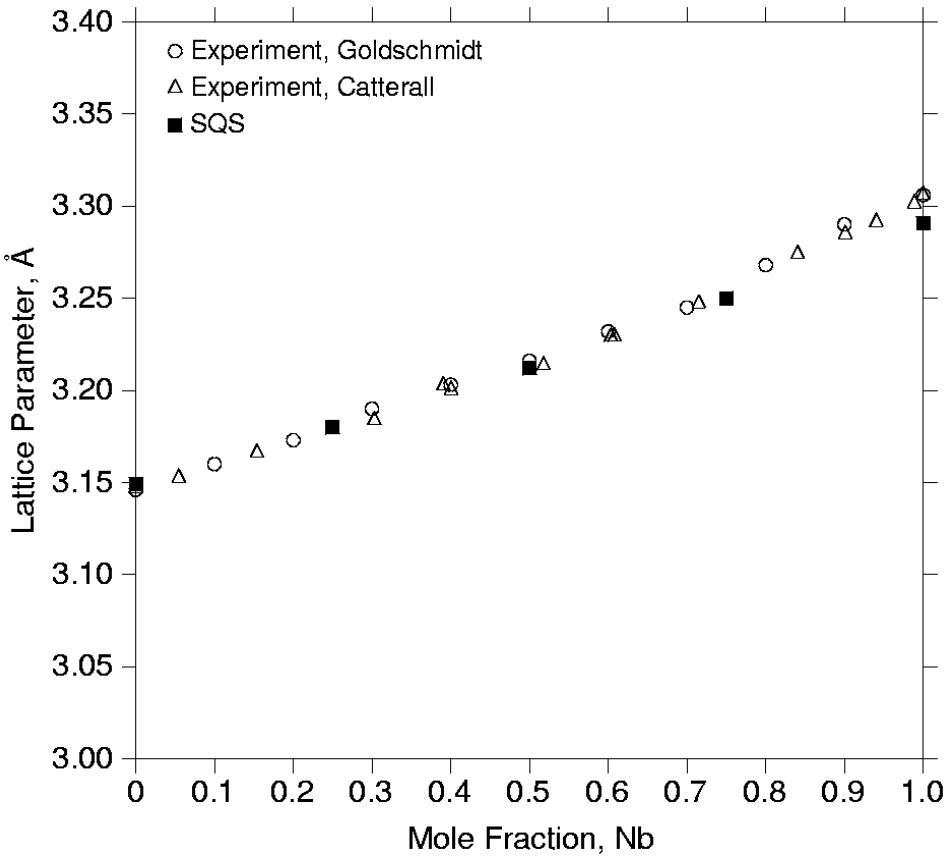

Figure 3.2. Equilibrium lattice parameters of Mo-Nb bcc alloys as a function of composition in comparison with the experimental data from Goldschmidt and Brand [57] and Catterall and Barker [58].

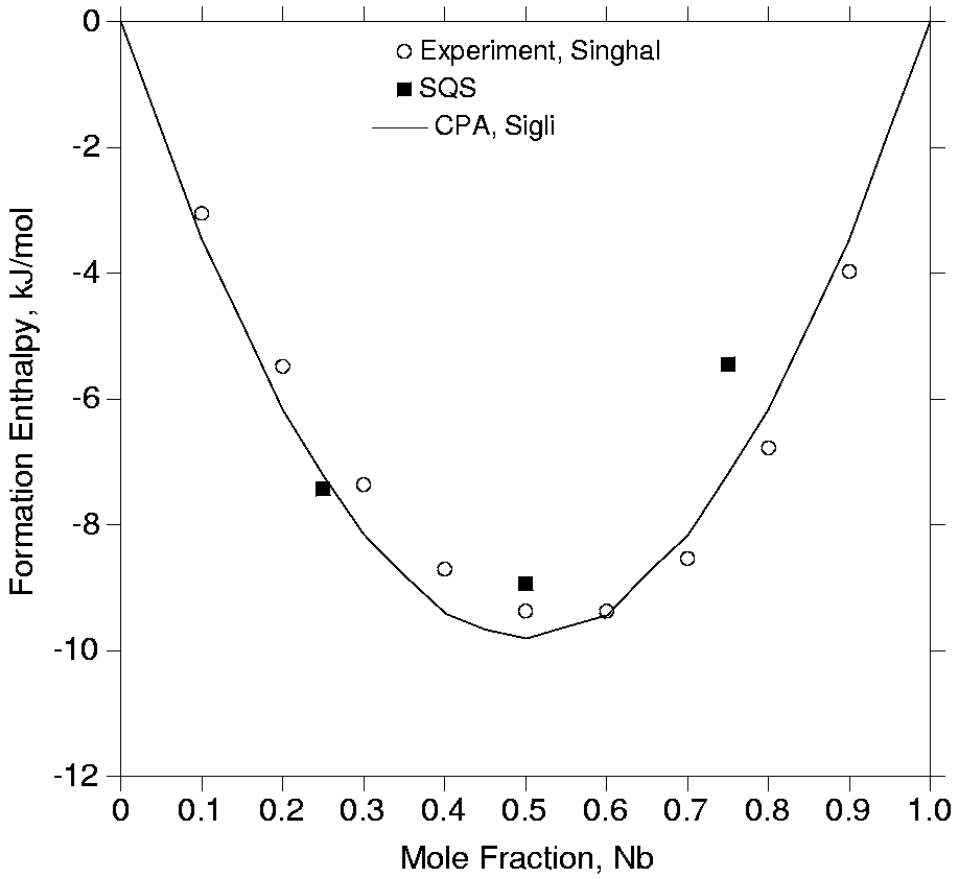

Figure 3.3 Formation enthalpies of Mo-Nb bcc alloys as a function of composition in comparison with the experimental data from Singhal and Worrell [56] and CPA calculations from Sigli *et al.* [59].

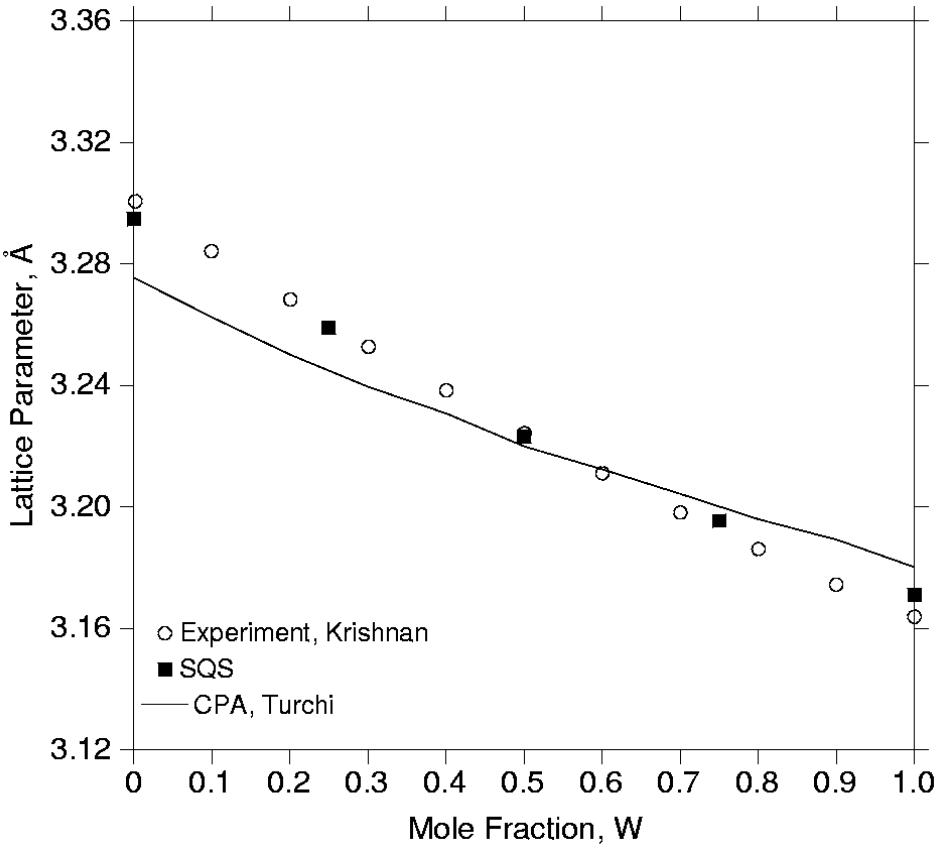

Figure 3.4. Equilibrium lattice parameters of Ta-W bcc alloys as a function of composition in comparison with the experimental data from Krishnan *et al.* [61] and CPA calculations from Turchi *et al.* [62].

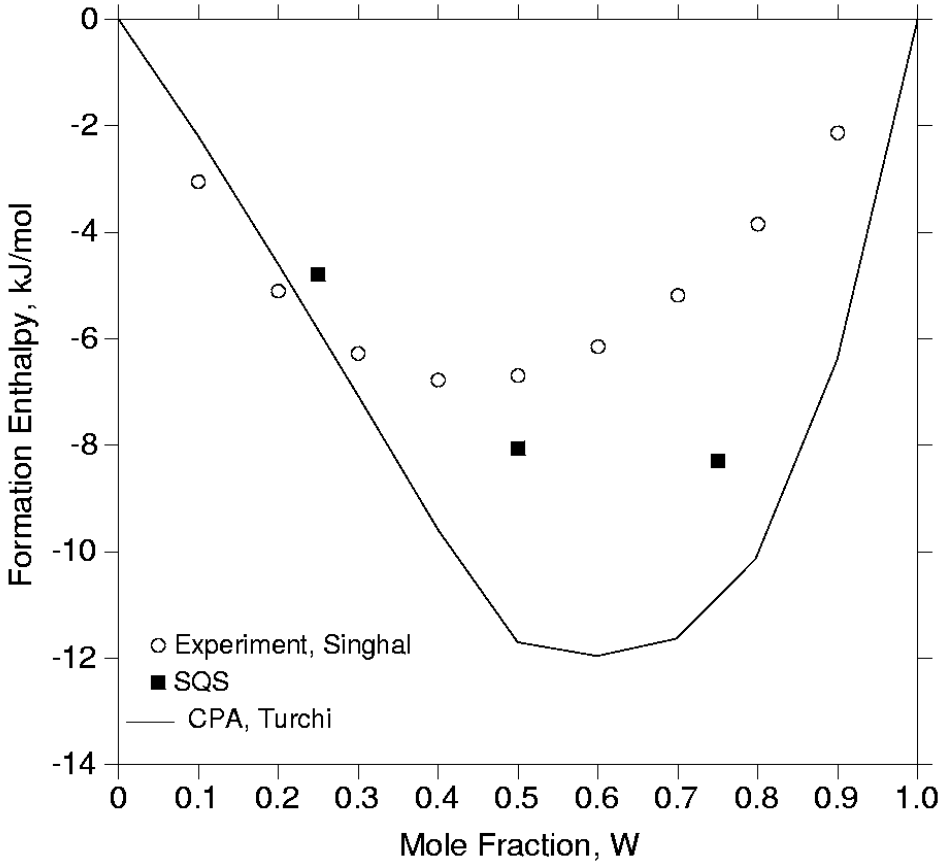

Figure 3.5. Formation enthalpies of Ta-W bcc alloys as a function of composition in comparison with the experimental data from Singhal and Worrell [60] and CPA calculations from Turchi *et al.* [62].

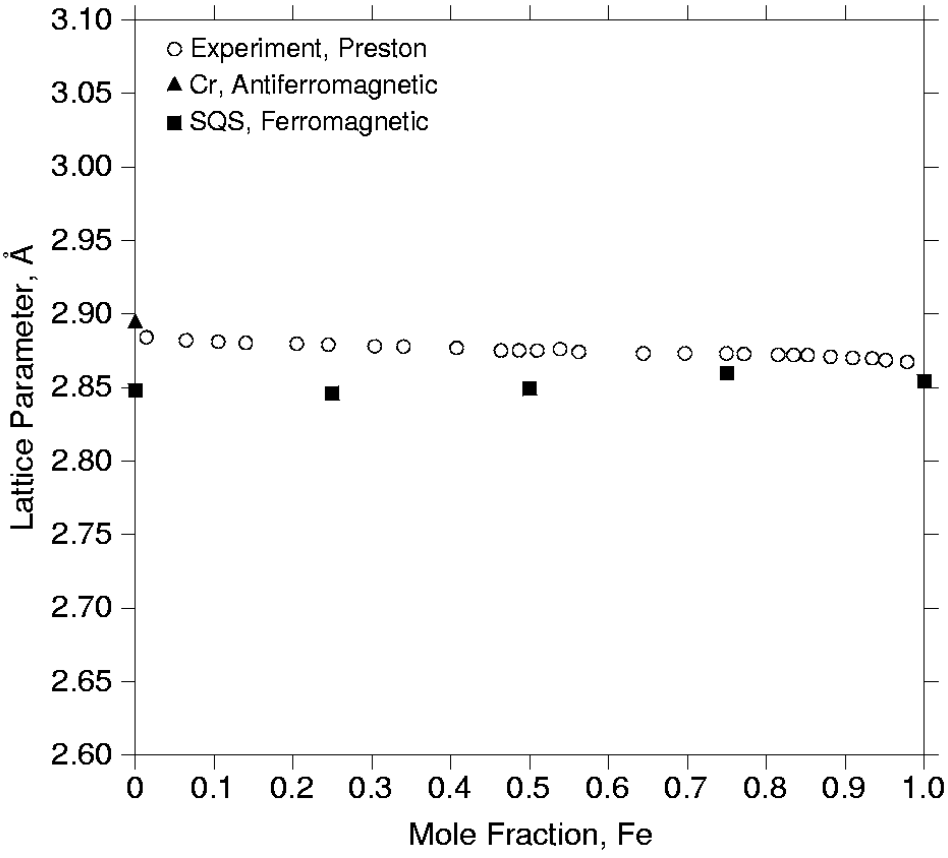

Figure 3.6. Equilibrium lattice parameters of Cr-Fe bcc alloys as a function of composition in comparison with the experimental data from Preston [65].

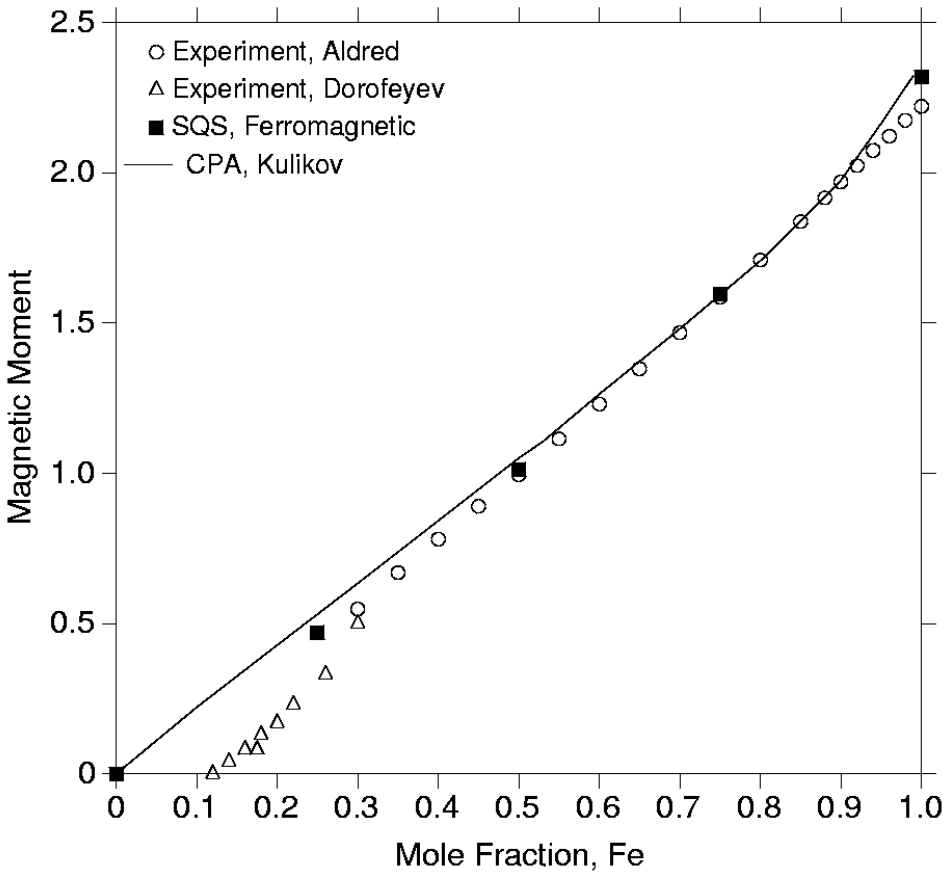

Figure 3.7. Magnetic moment of Cr-Fe bcc alloys as a function of composition in comparison with the experimental data from Aldred [66] and Dorofeyev *et al.* [67] and CPA calculations from Kulikov and Demangeat [68].

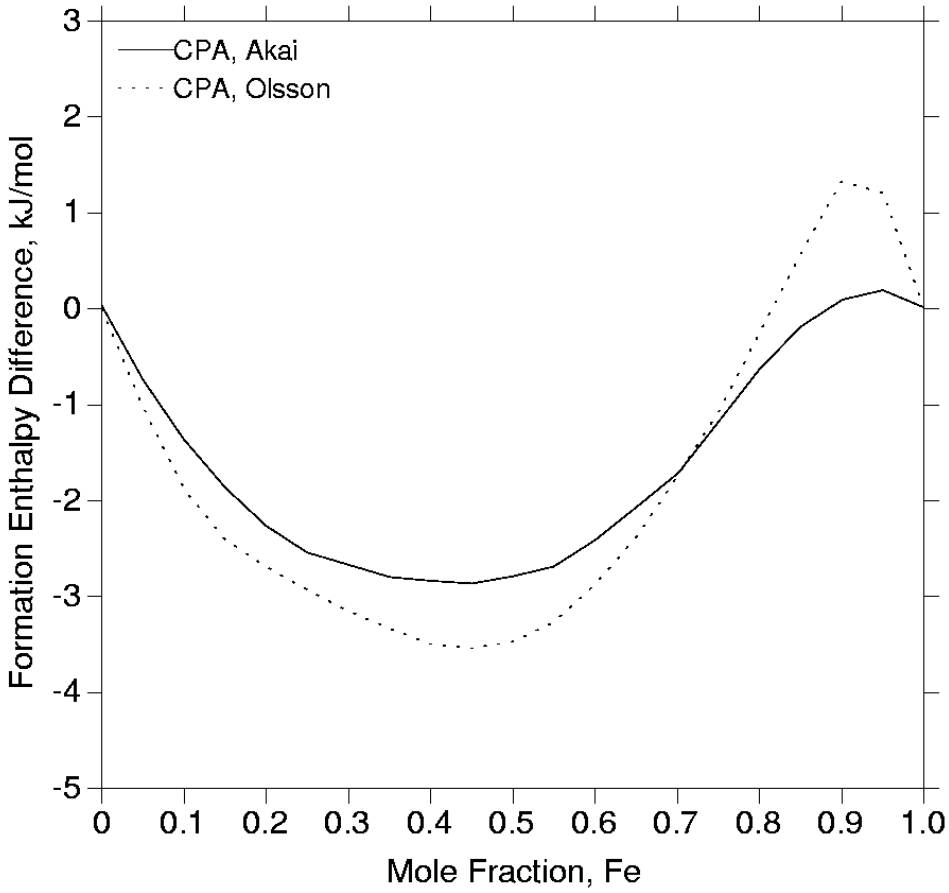

Figure 3.8. CPA calculated formation enthalpy difference between the paramagnetic and ferromagnetic states of Cr-Fe bcc alloys. Data are from Akai and Dederichs [70] and Olsson *et al.* [71].

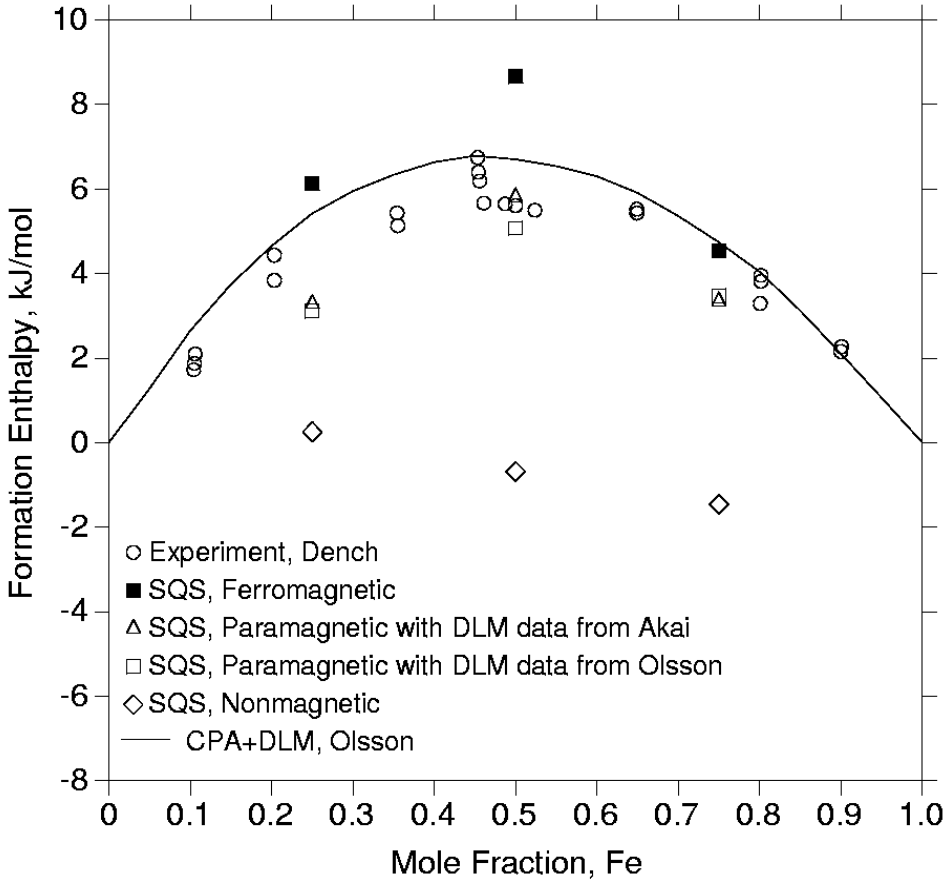

Figure 3.9. Theoretical and experimental formation enthalpies of Cr-Fe bcc alloys as a function of composition. The SQS paramagnetic results are obtained by adding the $\Delta H^{FM \to PM}$ from Akai and Dederichs [70] and Olsson *et al.* [71] to our SQS calculated formation enthalpies of ferromagnetic Cr-Fe bcc alloys. Experimental data are from Dench [69].

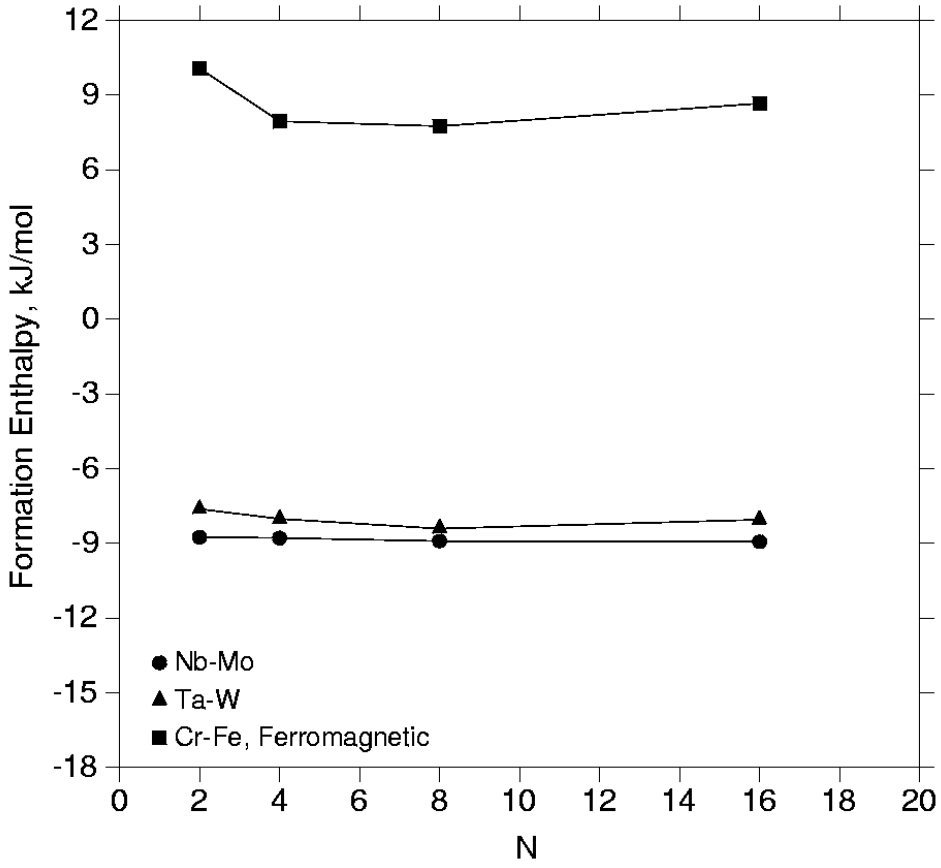

Figure 3.10. SQS calculated formation enthalpies of Nb-Mo, Ta-W and Cr-Fe bcc alloys at x=0.5 as a function of N, the number of atoms per unit cell.

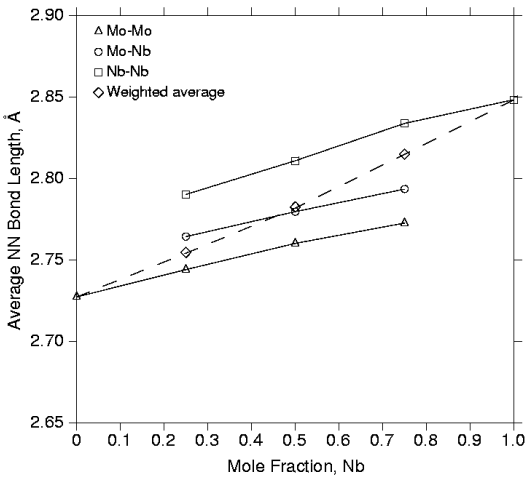

(a) Mo-Nb

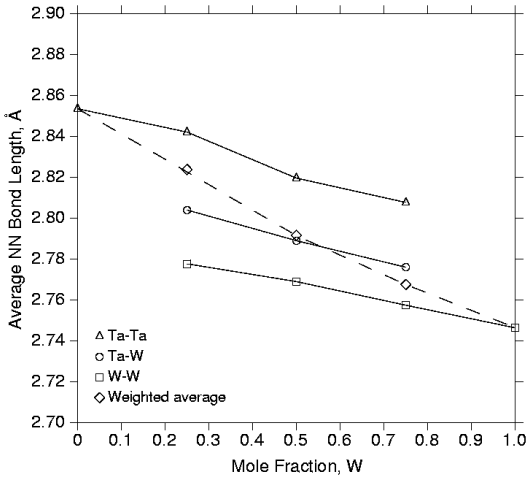

(b) Ta-W

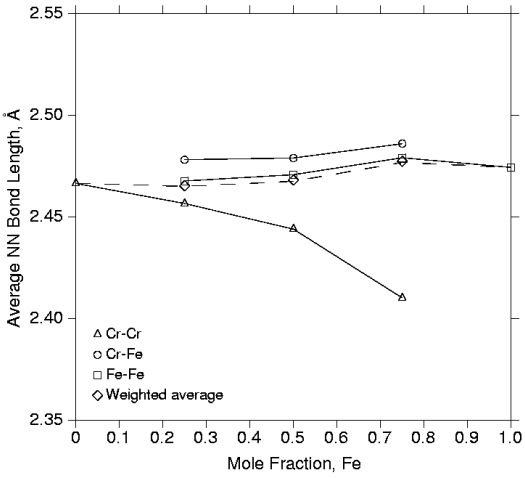

(c) Cr-Fe

Figure 3.11. SQS calculated average nearest-neighbor bond lengths as a function of composition in random (a) Mo-Nb, (b) Ta-W and (c) Cr-Fe bcc alloys. The dashed lines represent the average lattice.

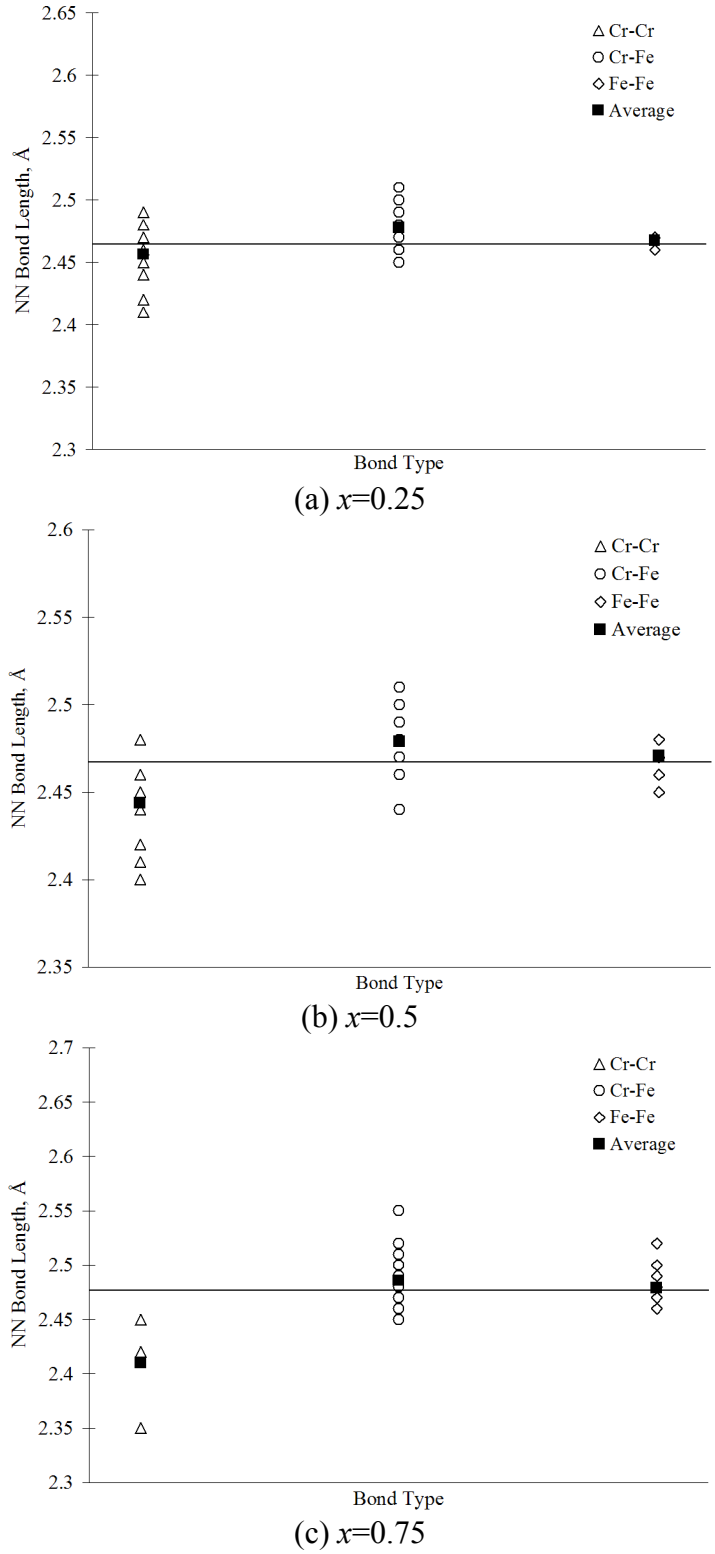

Figure 3.12. SQS calculated nearest neighbor bond length distributions in random $Cr_{1-x}Fe_x$ bcc alloys at composition (a) x=0.25, (b) x=0.5 and (c) x=0.75. The horizontal lines correspond to the average bcc lattice.

Chapter 4. FIRST-PRINCIPLES STUDY OF THE AL-CU SYSTEM

4.1. First-Principles Method

First-principles calculations are performed using the plane wave method with Vanderbilt ultrasoft pseudopotentials [46, 47], as implemented in the highly-efficient Vienna *ab initio* simulation package (VASP) [48, 49]. Calculations using both the local density approximation (LDA) and the generalized gradient approximation (GGA) are performed. The *k*-point meshes for Brillouin zone sampling are constructed using the Monkhorst–Pack scheme [52] and the total number of *k*-points times the total number of atoms per unit cell is at least 6000 for all structures. A plane wave cutoff energy E_{cut} of 292.2 eV is used for Al-Cu. According to our *k*-point and E_{cut} convergence tests, those parameters are more than enough to guarantee that the total energies are converged to well within 1 kJ/mol.

All structures are fully relaxed with respect to the volume and shape of the unit cell as well as all the internal atomic positions. By computing the quantum-mechanical forces and stress tensor, structural and atomic relaxations are performed and all atoms are relaxed into their equilibrium positions using a conjugate-gradient scheme. However, when treating the Al-Cu bcc phase, there exist special difficulties associated with the presence of structural instabilities: Al and Cu are stable in their fcc structure, but they are both mechanically unstable in their bcc structure when tetragonally deformed along the Bain path [72-74]. The total energy vs. c/a ratio curve exhibits a maximum at the bcc

structure (c/a=1), as shown in Figure 4.1. The bcc-based Al-Cu B2 structure is also found to be unstable with respect to Bain distortions. Interestingly, the Al-Cu B2 structure relaxes into fcc-based $L1_0$ with c/a=1.18, but not 1.414. This is because, for compounds, some symmetry-dictated extrema in pure elements will be lost as the symmetry is now determined by both structural parameters and atomic ordering [72, 73]. At higher temperatures, the bcc phase in the Al-Cu system is stabilized due to the vibrational entropy effect. Since all the present first-principles calculations are performed at T=0K where the bcc lattice is unstable, we artificially "force" those bcc-based structures to stay bcc by only relaxing their unit cell volumes but not the shape of the unit cell or the cell-internal atomic positions.

4.2. Results

4.2.1. Formation Enthalpies of Compounds

The formation enthalpies of the stable and metastable phases in the Al-Cu system are calculated by VASP in the present study using both LDA and GGA and the results are summarized in Table 4.1. The experimental data and previous first-principles calculated results in the literature are also included for comparison, when available. As shown, the GGA results are in consistently better agreement with experiments. As the result, GGA will be used in studying the Al-Cu system.

Very interestingly, contrary to the common belief that the energetic ground state of Al_2Cu is the θ phase, both the present LDA and GGA calculations show that θ′ is actually energetically more stable than θ. This is in accordance with the conclusions arrived by Wolverton and Ozolins [21]. Their calculations also show that the θ phase is stabilized at higher temperatures due to its high vibrational entropy.

4.2.2. SQS Results

SQS calculations are also performed for the fcc and bcc phases (the 16-atom fcc SQS's are given in Appendix A). Due to issue of structural instabilities, we only relaxed the volume of the bcc SQS's. The results are also given in Table 4.1.

4.2.3. Cluster Expansions

The cluster expansions of Al-Cu fcc alloys have been constructed by Muller *et al.* [75] using the full-potential linearized augmented plane-wave method (LAPW) and LDA. Using their cluster expansions, Muller *et al.* [75] obtained the formation enthalpies of random Al-Cu fcc alloys from Monte-Carlo simulations. In Figure 4.2, their results are compared with the present SQS calculations with good agreements.

In this chapter, to validate our SQS results, we further construct the cluster expansions of Al-Cu bcc alloys. The total energies of 45 bcc-based structures are calculated by VASP using GGA. Due to the structural instabilities, only the unit cell volumes are relaxed.

Those total energies are then used by the MAPS code in ATAT [20, 44] to automatically construct the cluster expansions of the Al-Cu bcc alloys. The final obtained pair and multi-body ECI's are shown in Figure 4.3. 9 pair interactions and 13 triple interactions are used in constructing the cluster expansions. The large number of triple interactions is necessary in order to account for the largely unsymmetrical formation enthalpies of the Al-Cu bcc alloys. For example, $\Delta H(Al_3Cu, D0_3)$=0.25 kJ/mol while $\Delta H(AlCu_3, D0_3)$=-21.1 kJ/mol. For sake of simplicity, the formation enthalpies of bcc-based structure in this section are all referred to bcc Al and bcc Cu.

In Figure 4.5, the formation enthalpies of the bcc-based structures predicted from the present cluster expansions are compared with the direct first-principles calculated results. The root mean square error of our fit, defined as:

$$RMS = \sqrt{\frac{1}{N}\sum_{i=1}^{N}(E_i^{Fit} - E_i^{Calc})^2} \tag{4.1}$$

is found to be 4.3 meV/atom, or 0.4 kJ/mol. The cross-validation score, which measures the predictive power of the cluster expansions, is found to be 13.4 meV/atom, or 1.3 kJ/mol. It is defined as:

$$CV = \sqrt{\frac{1}{N}\sum_{i=1}^{N}(E_i - \hat{E}_i)^2} \tag{4.2}$$

where E_i is the calculated energy of structure *i*, while $\hat{E}_i$ is the energy of structure *i* predicted from a cluster expansion constructed using the energies of the other *N*-1 structures.

Finally, Monte-Carlo simulations are performed in a canonical ensemble using a 12x12x12 simulation cell. An extremely high temperature of 50000K is used to simulate the truly random state of the alloy since at such high temperature, almost all the atom exchanges in the Metropolis algorithm will be accepted. The final results are given in Figure 4.6 in excellent agreement with the present SQS calculations.

4.3. Summary

In this chapter, the formation enthalpies of the stable and metastable phases in the Al-Cu system are calculated by VASP using both LDA and GGA. SQS calculations are performed for the Al-Cu fcc and bcc phases. The cluster expansions for the Al-Cu bcc alloys are also constructed. For both Al-Cu fcc and bcc alloys, the SQS predicted formation enthalpies of the random alloys agree rather well with the results obtained from cluster expansions.

Table 4.1. First-Principles calculated formation enthalpies (in kJ/mol) of phases in Al-Cu system. The reference states are: fcc Al and fcc Cu.

Phases		Space Group	VASP (LDA)	VASP (GGA)	FLAPW (LDA)	Experiments
Al Bcc		$Im\bar{3}m$ (229)	9.4	9.0		-
Cu Bcc		$Im\bar{3}m$ (229)	3.9	3.4		-
θ″ (Al_3Cu)		P4/mmm (123)	-10.3	-9.6	-9.3 [75]	-
θ′ (Al_2Cu)		$Fm\bar{3}m$ (225)	-20.8	-20.5	-19.2 [21]	-
θ (Al_2Cu)		I4/mcm (140)	-18.3	-16.2	-17.8 [21]	-13.1 [76] -13.4 [77]
η_2 (AlCu)		C/2m (12)	-24.0	-21.9	-	-19.9 [76] -20.0 [77]
γ_1 (Al_4Cu_9)		$P\bar{4}3m$ (215)	-22.9	-20.7	-	-20.3 [76]
Fcc SQS	$Al_{0.75}Cu_{0.25}$	-	-5.1 [43]	-5.9	-5.1 [75]	-
	$Al_{0.5}Cu_{0.5}$	-	-9.6 [43]	-9.5	-	-
	$Al_{0.25}Cu_{0.75}$	-	-	-11.3	-11.5 [75]	-
Bcc SQS	$Al_{0.75}Cu_{0.25}$	-	-	7.3	-	-
	$Al_{0.5}Cu_{0.5}$	-	-	-0.3	-	-
	$Al_{0.25}Cu_{0.75}$	-	-	-7.5	-	-

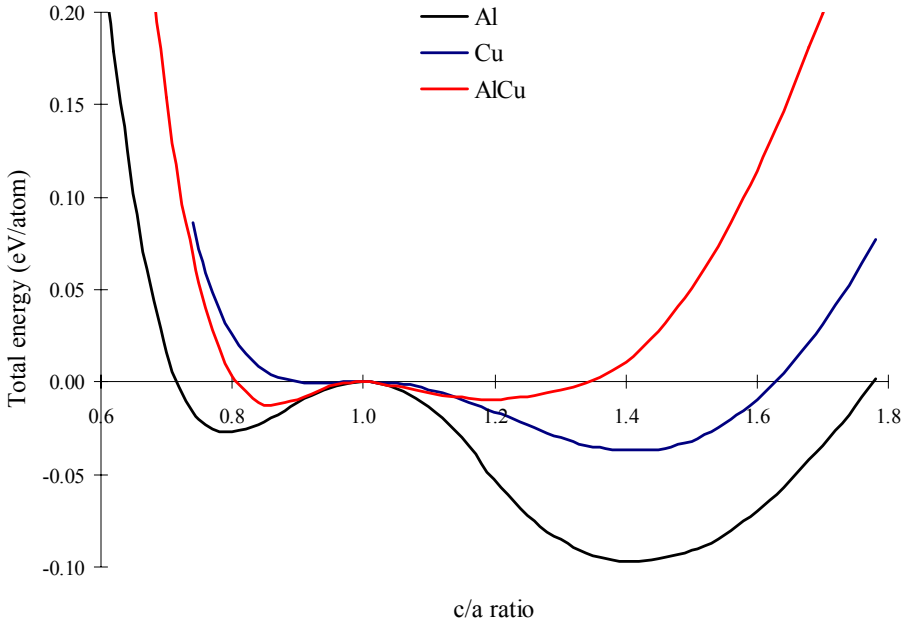

Figure 4.1. Total energy vs. c/a ratio along the tetragonal Bain path. c/a=1 corresponds to bcc and c/a=1.414 corresponds to fcc.

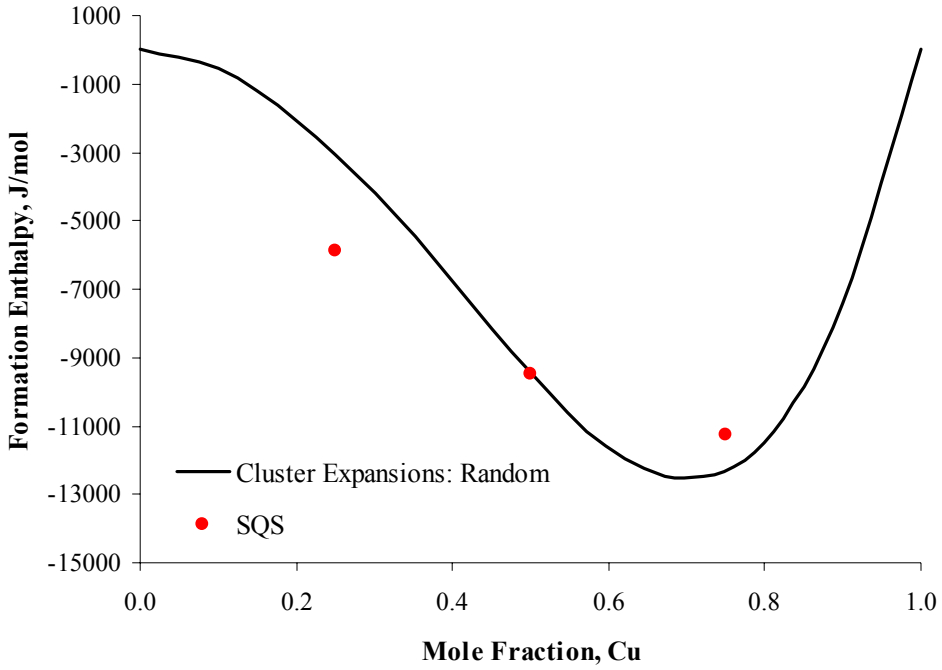

Figure 4.2. Formation enthalpies of random Al-Cu fcc alloys obtained from the present SQS calculations in comparison with the cluster expansions results from Muller *et al.* [75].

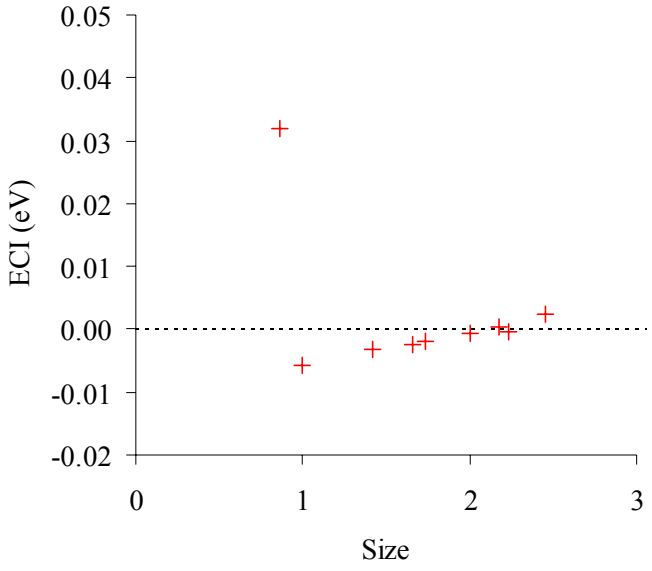

(a) Pair Interactions

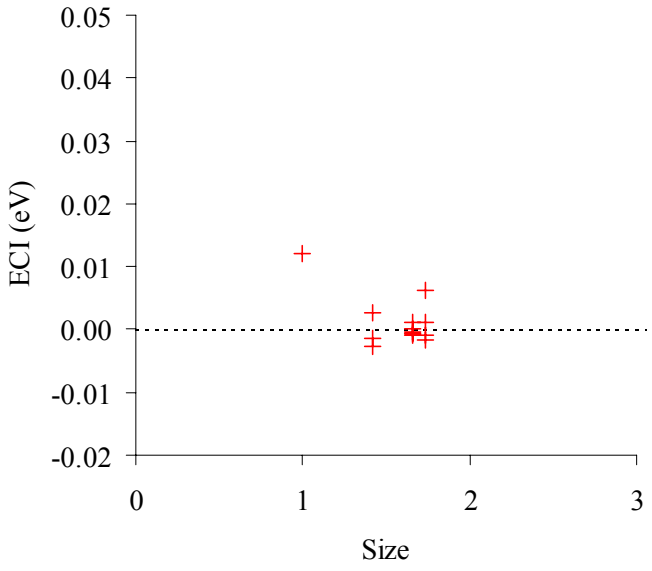

(b) Triple Interactions

Figure 4.3. The obtained (a) pair and (b) triple ECI's of Al-Cu bcc alloys.

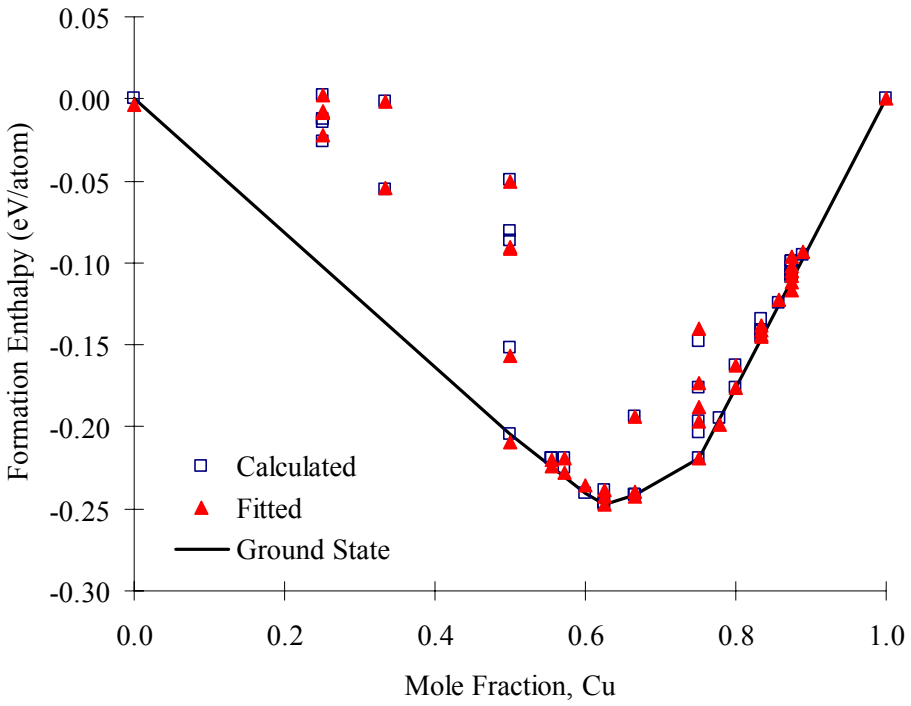

Figure 4.4. The calculated and fitted formation enthalpies of bcc-based structures as a function of composition. The calculated ground state convex hull is also shown.

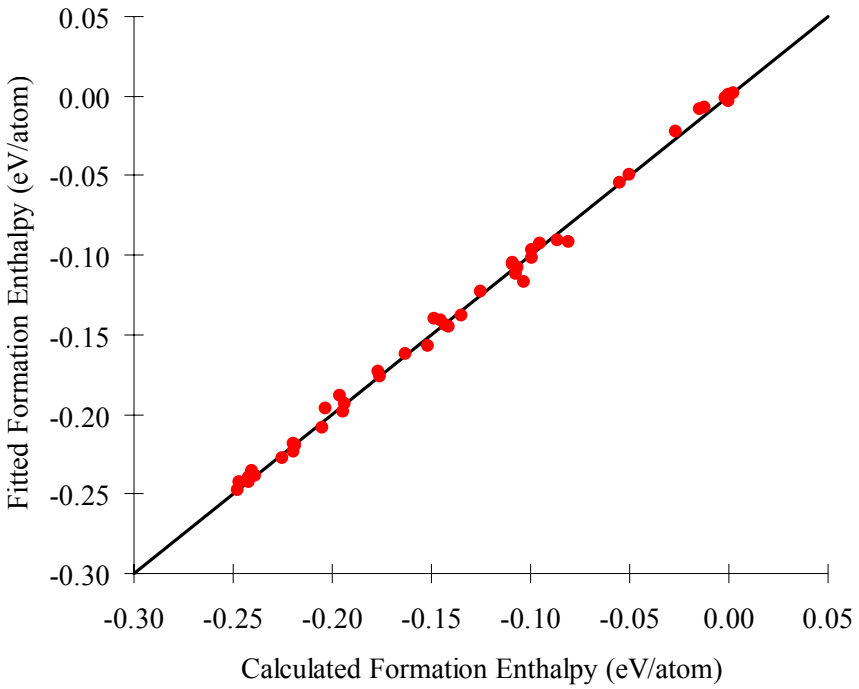

Figure 4.5. Comparisons between calculated and fitted formation enthalpies.

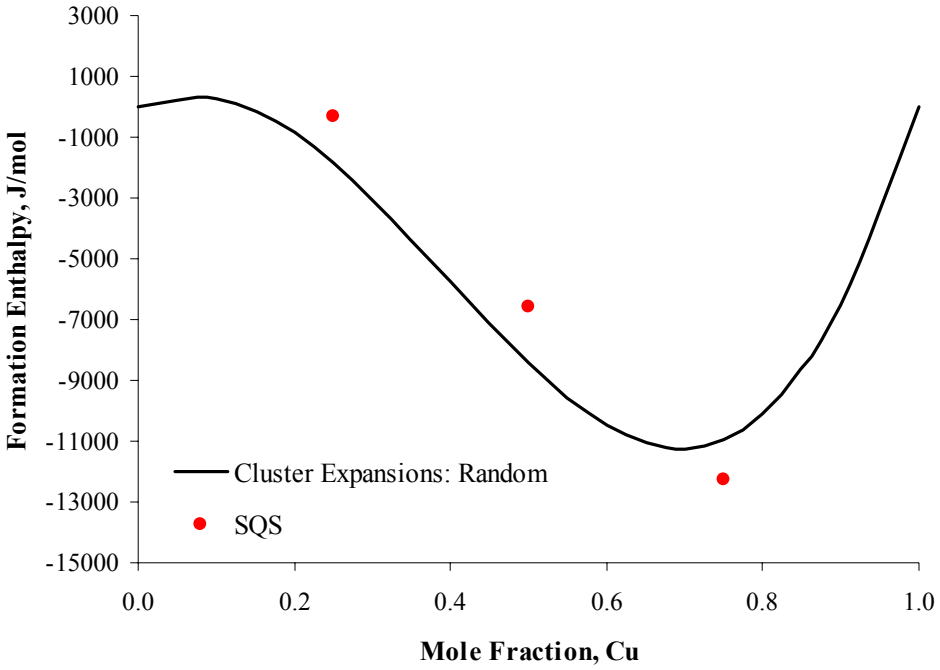

Figure 4.6. Formation enthalpies of random Al-Cu bcc alloys obtained from the present SQS calculations in comparison with the Monte-Carlo simulated results using the present cluster expansions.

Chapter 5. THERMODYNAMIC REMODELING OF THE AL-CU SYSTEM INCOPORATING FIRST-PRINCIPLES ENERGETICS

5.1. Literature Review

A comprehensive review of the phase equilibria and thermochemical data of the Al-Cu binary system has been given by Murray [78] and will not be repeated here. Following are the new experimental data not included by Murray [78].

5.1.1. Phase Equilibrium Data

Recently, Liu *et al.* [79] reinvestigated the phase equilibria in the Al–Cu system over the temperature range 500~1000°C and composition range 40~85at.% Cu using diffusion couple, differential scanning calorimetry (DSC) and high temperature X-ray diffraction (XRD) methods. Liu *et al.* [79]'s data are used in the present optimization process.

5.1.2. Thermochemical Data

Recently, Stolz *et al.* [80], Witusiewicz [81] and Kanibolotsky *et al.* [82] redetermined the enthalpy of mixing of the liquid Al-Cu alloys using a high-temperature calorimeter. Surprisingly, their data are much more negative than adopted by Murray [78]. The new data by Stolz *et al.* [80] and Witusiewicz [81] are used in the present optimization process.

5.2. First-Principles Data

The first-principles data in Chapter 4 are used in the present CALPHAD optimization process together with the existing experimental thermochemical and phase equilibria data. In addition, the vibrational formation entropies of θ and θ′ calculated by Wolverton and Ozolin [21] using the linear-response theory [22] are also used.

5.3. Thermodynamic Modeling

5.3.1. Pure Elements

Solid Al and Cu both have the face-centered cubic (fcc) structure. The Gibbs energies of pure Al and Cu in their stable, metastable and unstable states are directly taken from the SGTE pure element database.

5.3.2. Solution Phases

The liquid, fcc and bcc phases are treated using substitutional solution model (Eq. (2.4)).

5.3.3. θ phase

The θ phase is described by an $(Al)_{0.667}(Al,Cu)_{0.333}$ two-sublattice model. Its Gibbs energy per mole of formula units is written as:

$$G_m = y_{Al}^{II\,\circ}G_{Al:Al} + y_{Cu}^{II\,\circ}G_{Al:Cu} + 0.333RT(y_{Al}^{II}\ln y_{Al}^{II} + y_{Cu}^{II}\ln y_{Cu}^{II}) + y_{Al}^{II}y_{Cu}^{II}L_{Al:Al,Cu} \quad (5.1)$$

where $L_{Al:Al,Cu}$ is the interaction parameter in the second sublattice.

5.3.4. The η and ε phase

The η and ε phase are described by an $(Cu)_{0.5}(Al,Cu)_{0.5}$ two-sublattice model. Its Gibbs energy per mole of formula units is written as:

$$G_m = y_{Al}^{II\,\circ}G_{Cu:Al} + y_{Cu}^{II\,\circ}G_{Cu:Cu} + 0.5RT(y_{Al}^{II}\ln y_{Al}^{II} + y_{Cu}^{II}\ln y_{Cu}^{II}) + y_{Al}^{II}y_{Cu}^{II}L_{Cu:Al,Cu} \quad (5.2)$$

where $L_{Cu:Al,Cu}$ is the interaction parameter in the second sublattice.

5.3.5. The γ_0 and γ_1 Phase

The γ_0 and γ_1 phase are described by an $(Al)_{0.3077}(Al,Cu)_{0.0769}(Cu)_{0.6154}$ three-sublattice model. Their Gibbs energies per mole of formula units are written as:

$$G_m = y_{Al}^{II\,\circ}G_{Al:Al:Cu} + y_{Cu}^{II\,\circ}G_{Al:Cu:Cu} + 0.0769RT(y_{Al}^{II}\ln y_{Al}^{II} + y_{Cu}^{II}\ln y_{Cu}^{II}) + y_{Al}^{II}y_{Cu}^{II}L_{Cu:Al,Cu} \quad (5.3)$$

where $L_{Al:Al,Cu:Cu}$ is the interaction parameter in the second sublattice. ${}^{\circ}G_{i:j:k}$ is the Gibbs energy of the compound with the first sublattice entirely occupied by element i, the second entirely by j, and the third entirely by k, be it real or hypothetical.

5.3.6. Stoichiometric Compounds

Compounds ξ-Al_9Cu_{11}, δ-Al_2Cu_3, θ′ and θ″ with negligible homogeneity ranges are modeled as stoichiometric compounds in the present assessment. Their Gibbs energies are expressed as:

$$ {}^{\circ}G_m^{Al_{1-x}Cu_x} = (1-x)\,{}^{\circ}G_{Al}^{fcc} + x\,{}^{\circ}G_{Cu}^{fcc} + A + BT \qquad (5.4) $$

where A and B are the enthalpy and entropy of formation of the compound, respectively.

5.4. Optimization Procedures

Evaluation of the model parameters is performed using the PARROT program [83] in Thermo-Calc [14], which works by minimizing the weighted sum of differences between calculated and experimentally measured values using nonlinear least-square regression. Different types of experimental data can be optimized simultaneously (the original input file for Thermo-Calc used in the present assessment is listed in Appendix B). The weight for each piece of experimental data is chosen according to its experimental uncertainty

and relative importance, and will be changed repeatedly during the assessment until most of the experimental data are reasonably reproduced.

Since thermodynamic properties are generally explicitly related to model parameters, e.g. the enthalpies of formation of liquid and solid phases, they are optimized first in the present optimization. Phase equilibrium data, such as liquidus and invariant reaction measurements, are then gradually incorporated into the optimization with more and more model parameters introduced.

At the final stage of assessment, global optimization is performed. All parameters are optimized simultaneously with all experimental data included, which ensures the best possible agreement between model calculations and experimental data. The adjustments of model parameters are rather small after the global optimization. The final obtained model parameters are given in Table 5.1. The parameters from the COST 507 database are also shown. In Table 5.2, the present optimized parameters are compared with the first-principles results with good agreements. The final Thermo-Calc database file for Al-Cu system is given in Appendix C.

5.5. Results and Discussions

Figure 5.1 shows the calculated formation enthalpy of the liquid phase using the present model parameters in good agreement with experimental measurements. The calculated activities of Al and Cu in liquid are also in good agreement with experiments, as shown

in Figure 5.2 and Figure 5.3. Figure 5.4 gives the calculated formation enthalpies of solid phases at 298K. Figure 5.5 and Figure 5.6 also give the calculated formation enthalpies of Al-Cu fcc and bcc solution phases in comparison with the experimental and first-principles data. The agreements between model calculations, experimental measurements and first-principles calculations are quite good, except for the bcc solution phase, where large discrepancies exist between model calculations and first-principles results. We attribute such large discrepancies to the mechanical instability of the bcc structure in Al-Cu system rather than the failure of SQS. In fact, the large discrepancies between CALPHAD and first-principles when treating unstable structures have been a long-standing issue, as is discussed in a recent paper by Wang *et al.* [84].

Figure 5.7 shows the calculated Al-Cu phase diagram in comparison with experimental measurements. All of the phase equilibria data are well reproduced. Figure 5.8 also gives the blowup of the Al-rich and Cu-rich part of the calculated phase diagram. The $\theta' \rightarrow \theta$ transition temperature is predicted in the present study to be 279K, somewhat lower than the 423~473K temperature range predicted by Wolverton and Ozolins [21]. At such low temperatures, although thermodynamically favorable, the $\theta' \rightarrow \theta$ transition is actually not possible due to the extremely slow kinetics.

In Figure 5.9, the metastable solvus of θ' and θ'' in Al-Cu system are calculated and compared with experimental measurements. The calculated incoherent metastable fcc miscibility gap is also shown. Very interestingly, even without considering the elastic energy, the incoherent metastable fcc miscibility gap predicted in the present work is

already much lower than the experimentally measured GP-I Zone solvus, as shown in Figure 5.9. This well suggests that GP-I zone formation in Al-Cu may not be due to the metastable miscibility gap, the "traditional" explanation of GP-I zones, but rather due to the metastable coherent ordering, as proposed by Wolverton [3].

It may be asked why the present model parameters and the COST 507 database give similar equilibrium phase diagram but quite different metastable one, e.g. metastable fcc miscibility gap. This is actually due to semi-empirical "fitting" nature of CALPHAD. In the present study, with the integration of first-principles energetics into the CALPHAD framework, the previously semi-empirical CALPHAD approach is now on solid physical ground and its predictive power is greatly enhanced.

Table 5.1. Assessed thermodynamic parameters of the Al-Cu system (in SI units).

Phase	Model	Parameter	Present	COST 507
Liquid	(Al,Cu)	${}^{0}L_{Al,Cu}$	-66054+8.363T	-66622+8.1T
		${}^{1}L_{Al,Cu}$	32489-8.524T	46800-90.8T+10TlnT
		${}^{2}L_{Al,Cu}$	7420-10.702T	-2812
Fcc	(Al,Cu)	${}^{0}L_{Al,Cu}$	-43205-4.630T	-53520+2T
		${}^{1}L_{Al,Cu}$	45224-6.789T	38590-2T
		${}^{2}L_{Al,Cu}$	-16747+11.614T	1170
Bcc	(Al,Cu)	${}^{0}L_{Al,Cu}$	-73083+4.810T	-73554+4T
		${}^{1}L_{Al,Cu}$	48345-7.216T	51500-11.84T
θ	$(Al)_{0.667}(Al,Cu)_{0.333}$	${}^{\circ}G_{Al:Al}$	${}^{\circ}G_{Al}^{bcc}$	${}^{\circ}G_{Al}^{bcc}$
		$\Delta G_{Al,Cu}$	-16025+2.719T	-15802+2.25T
		${}^{0}L_{Al:Al,Cu}$	0	737
θ′	$(Al)_{0.667}(Cu)_{0.333}$	$\Delta G_{Al,Cu}$	-16783+5.434T	-
θ″	$(Al)_{0.75}(Cu)_{0.25}$	$\Delta G_{Al,Cu}$	-8389+0.385T	-
ξ	$(Al)_{0.45}(Cu)_{0.55}$	$\Delta G_{Al,Cu}$	-21384+1.960T	-21000+0.9T
δ	$(Al)_{0.4}(Cu)_{0.6}$	$\Delta G_{Al,Cu}$	-22278+1.702T	-21340+0.6T
η	$(Cu)_{0.5}(Al,Cu)_{0.5}$	${}^{\circ}G_{Cu:Cu}$	${}^{\circ}G_{Cu}^{bcc}$	${}^{\circ}G_{Cu}^{bcc}$
		$\Delta G_{Cu:Al}$	-20315+2.079T	-20280+1.57T
		${}^{0}L_{Cu:Al,Cu}$	-17953	-12870-10T
ε	$(Cu)_{0.5}(Al,Cu)_{0.5}$	${}^{\circ}G_{Cu:Cu}$	$22019+{}^{\circ}G_{Cu}^{fcc}$	${}^{\circ}G_{Cu}^{bcc}$
		$\Delta G_{Cu:Al}$	-20313+3.000T	-18488+0.6T
		${}^{0}L_{Cu:Al,Cu}$	-29635-27.517T	3800-12T
		${}^{1}L_{Cu:Al,Cu}$	0	-36000
γ_1	$(Al)_{0.3077}(Al,Cu)_{0.0769}(Cu)_{0.6154}$	$\Delta G_{Al:Al:Cu}$	-24185+31T-4TlnT	-23132+30T-4TlnT
		$\Delta G_{Al:Cu:Cu}$	-20622+28.5T-4TlnT	-21577+29.2T-4TlnT
γ_0	$(Al)_{0.3077}(Al,Cu)_{0.0769}(Cu)_{0.6154}$	$\Delta G_{Al:Al:Cu}$	-16339-4T	-16866-3.5T
		$\Delta G_{Al:Cu:Cu}$	-15185-4.5T	-15420-4.5T

Table 5.2. Comparisons between optimized parameters with first-principles calculated results. For the formation enthalpies, only GGA results are shown.

Phases	Source	ΔH (kJ/mol)	ΔS (J/mol/K)
Al_2Cu (θ)	Present Assessment	-16.0	-2.719
	First-Principles	-16.2 (Present)	-2.079 [21]
Al_2Cu (θ′)	Present Assessment	-16.8	-5.434
	First-Principles	-20.5 (Present)	-5.155 [21]
Al_3Cu (θ″)	Present Assessment	-8.4	-0.385
	First-Principles	-9.6 (Present)	-

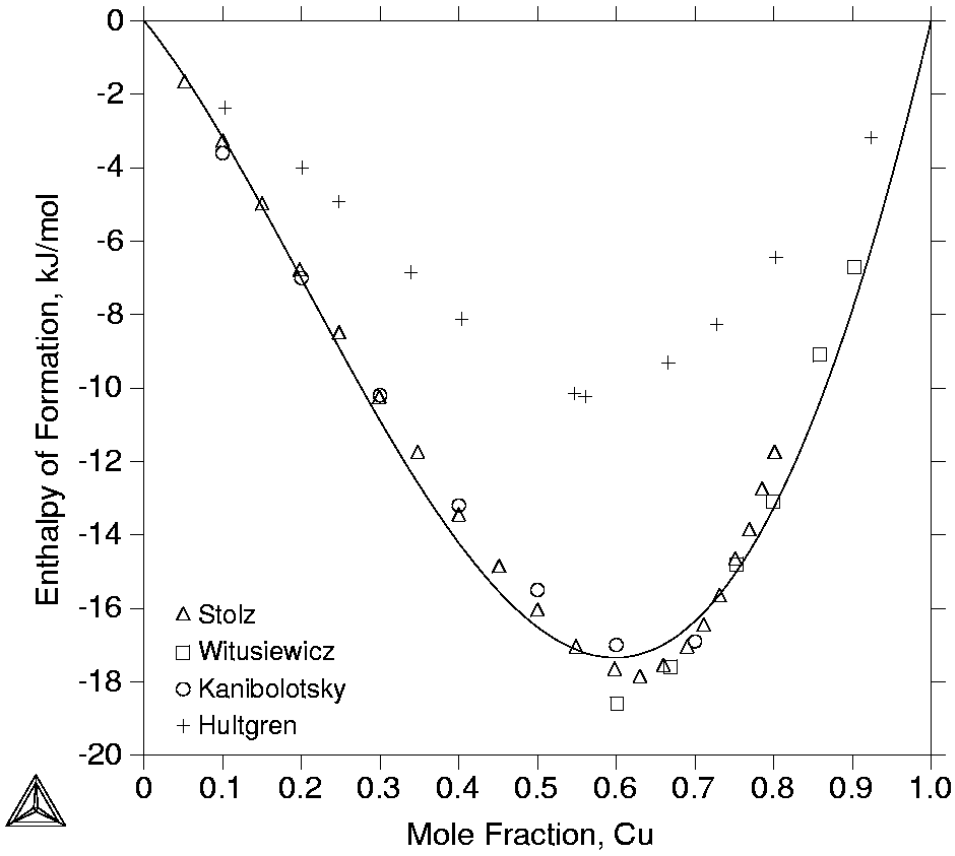

Figure 5.1. The calculated enthalpy of formation of liquid in comparison with the experimental data from Stolz *et al.* [80], Witusiewicz [81], Kanibolotsky *et al.* [82] and Hultgren *et al.* [85]. Reference states: liquid Al and liquid Cu.

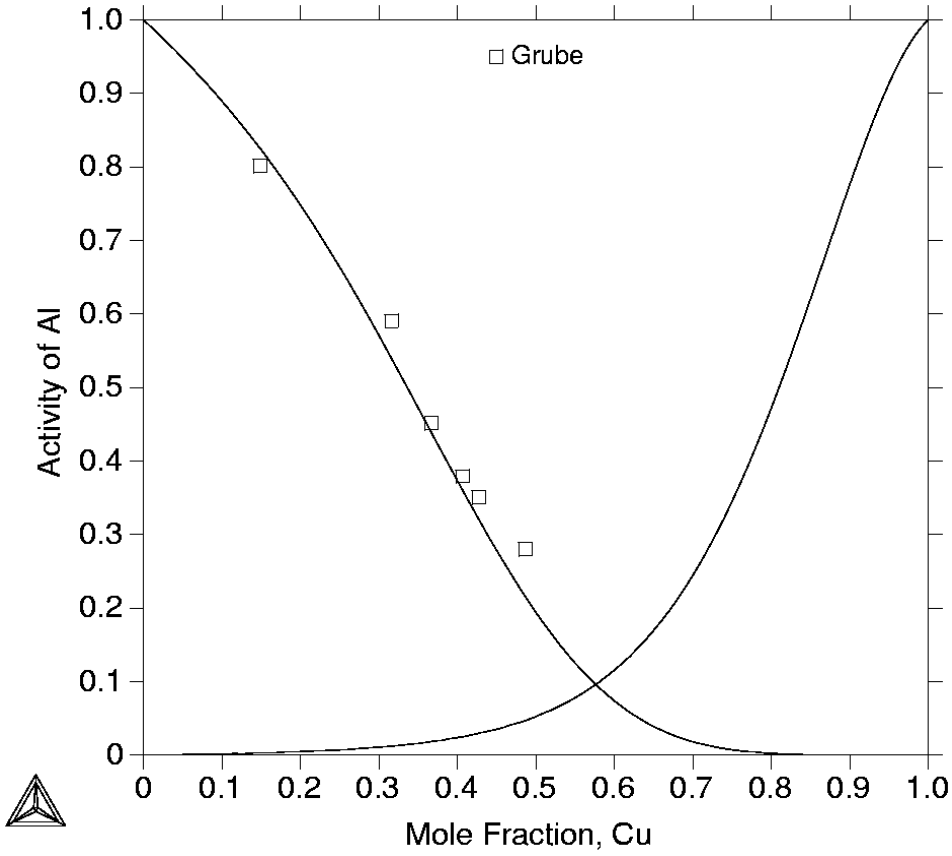

Figure 5.2. The calculated activities of Al in liquid at T=1073K in comparison with the experimental data from Grube and Hantelmann [86]. Reference states: liquid Al.

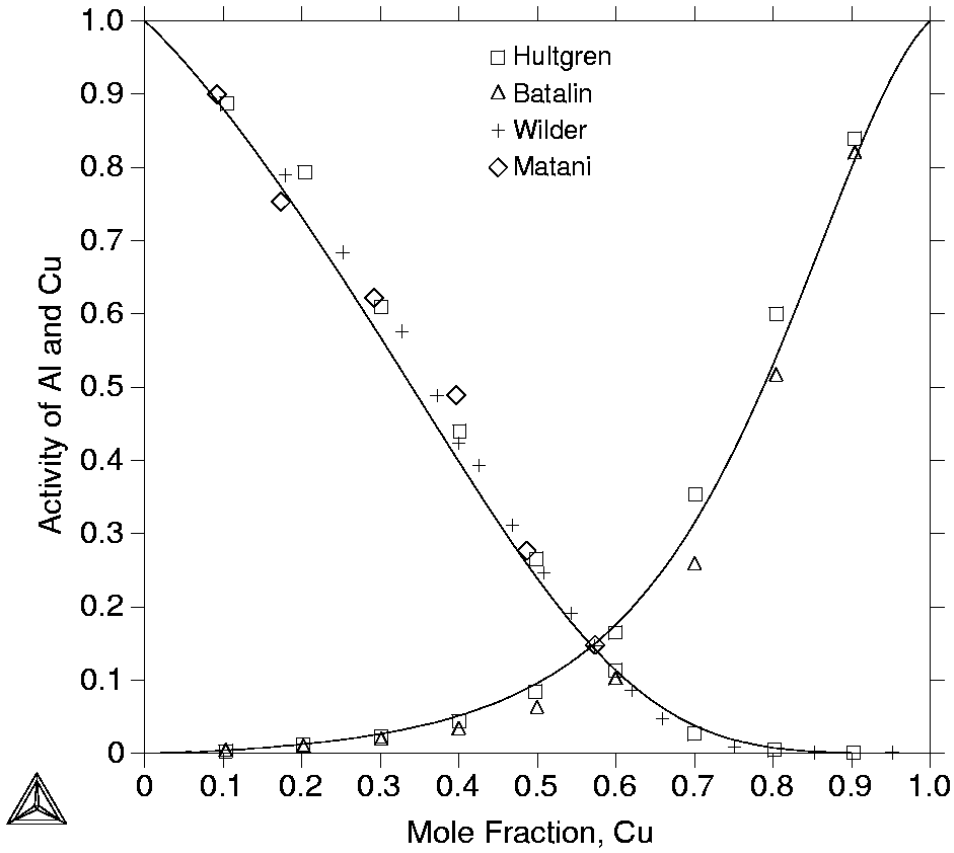

Figure 5.3. The calculated activities of Al and Cu in liquid at T=1373K in comparison with the experimental data from Hultgren *et al.* [87], Batalin *et al.* [88], Wilder [89] and Matani and Nagai [90]. Reference states: liquid Al and liquid Cu.

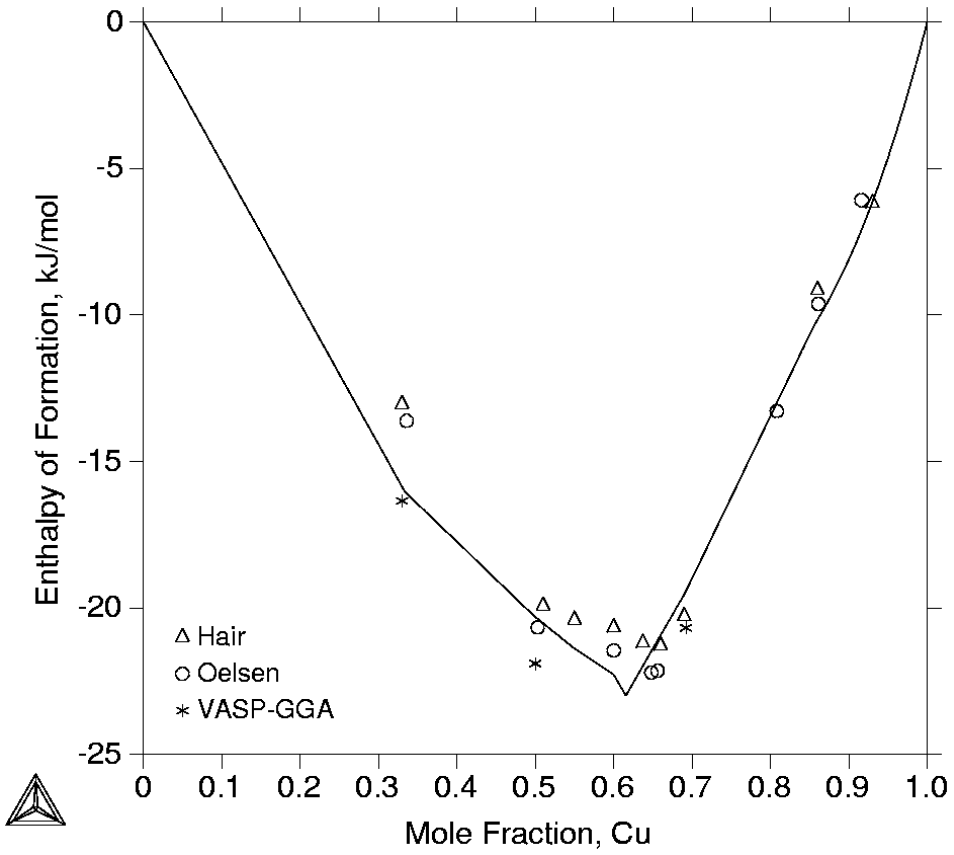

Figure 5.4. The calculated formation enthalpies of Al-Cu solid phases at T=298.15K in comparison with the experimental data from Hair and Downie [76] and Oelsen and Middel [77]. The present VASP-GGA results are also shown. Reference states: fcc Al and fcc Cu.

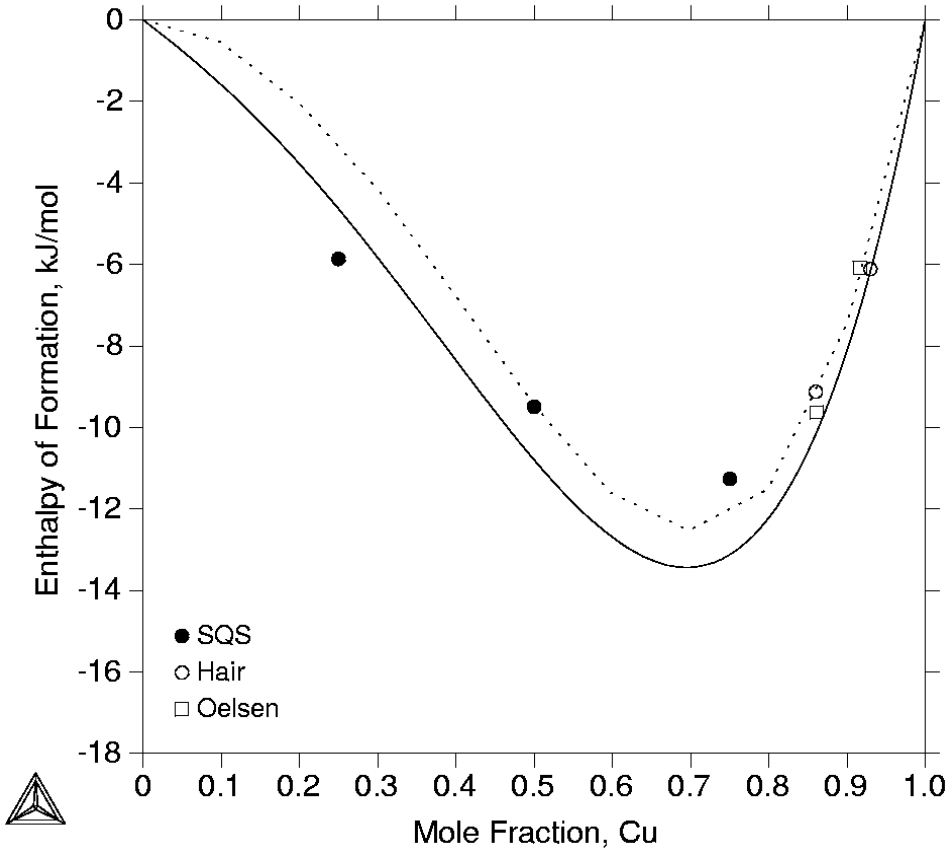

Figure 5.5. The calculated formation enthalpies of Al-Cu fcc alloys in comparison with the experimental data from Hair and Downie [76] and Oelsen and Middel [77] and the present first-principles SQS results. The cluster expansions results from Muller *et al.* [75] are also included and shown as dash line. Reference states: fcc Al and fcc Cu.

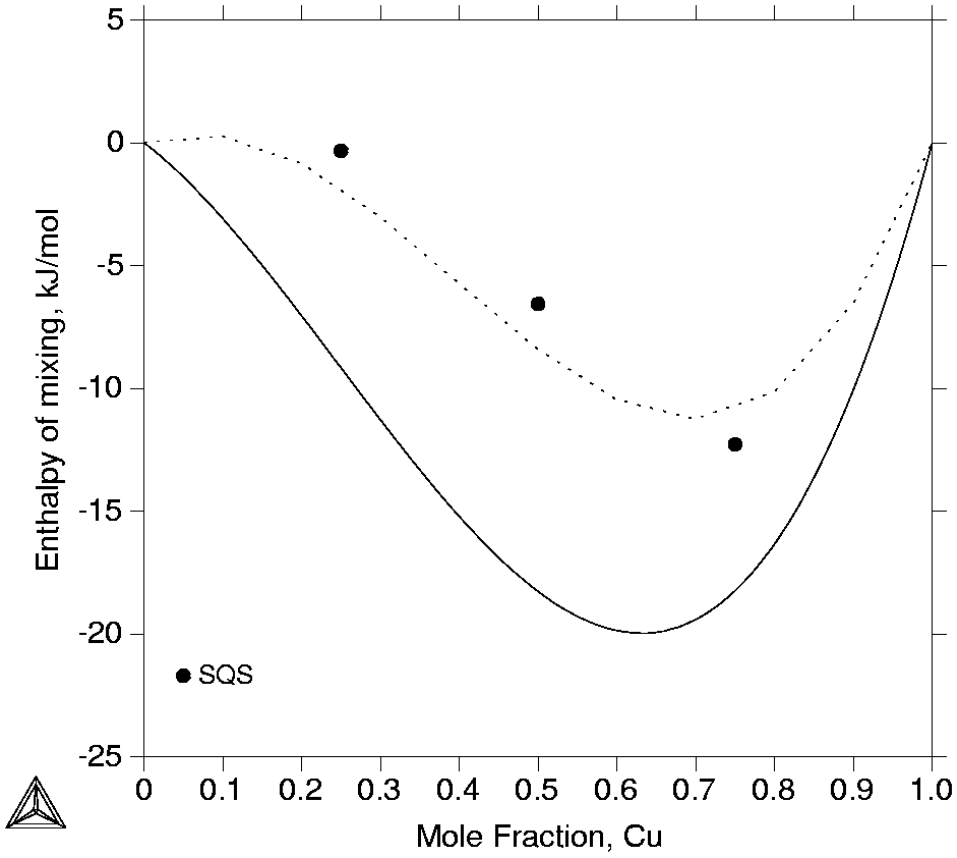

Figure 5.6. The calculated formation enthalpies of Al-Cu bcc alloys in comparison with the first-principles SQS results. The cluster expansions results from the present study are also included and shown as dashed line. Reference states: bcc Al and bcc Cu.

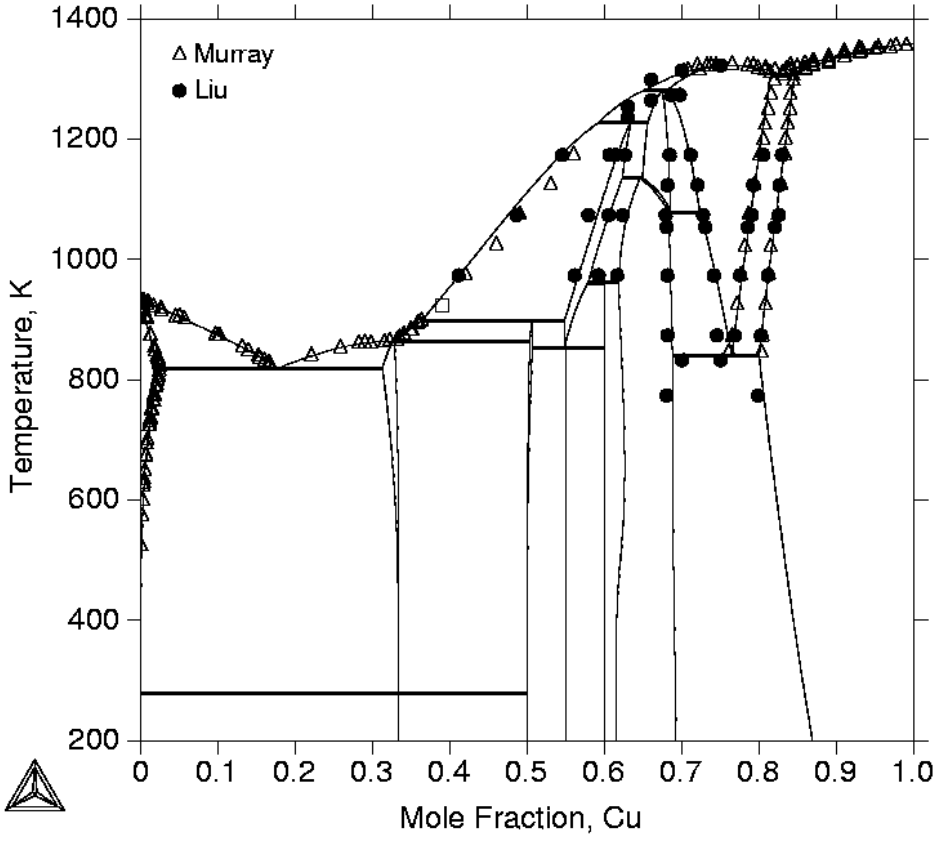

Figure 5.7. The calculated equilibrium Al-Cu phase diagram in comparison with the experiment data from Murray [78] and Liu *et al.* [79].

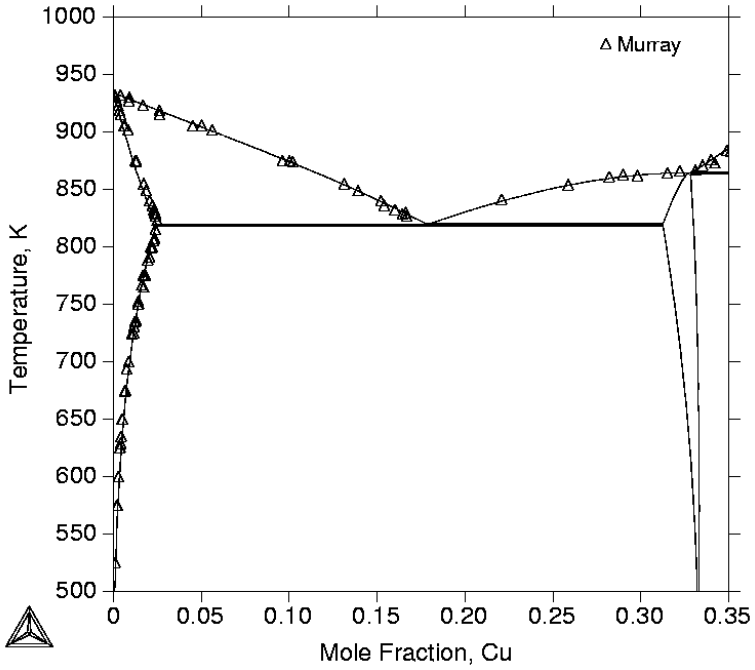

(a) Al-rich corner

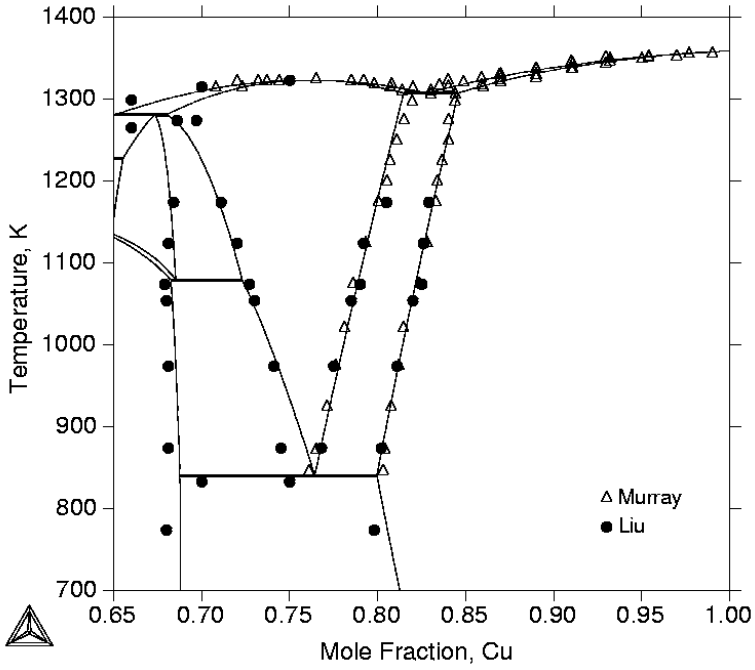

(b) Cu-rich corner

Figure 5.8. The (a) Al-rich and (b) Cu-rich corner of the calculated equilibrium Al-Cu phase diagram in comparison with the experiment data from Murray [78] and Liu *et al.* [79].

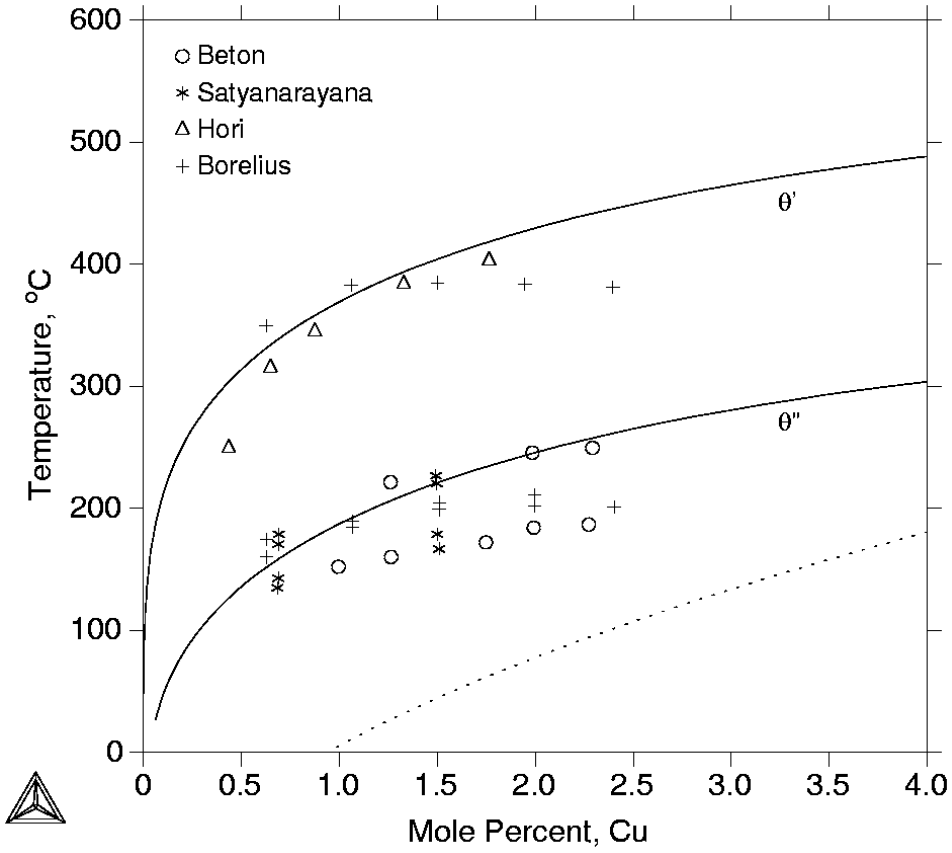

Figure 5.9. The calculated metastable θ′ and θ″ solvus of Al-Cu system in comparison with the experiment solvus data from Beton and Rollason [26], Satyanarayana *et al.* [27], Hori and Hirano [91] and Borelius *et al.* [92]. The incoherent metastable fcc miscibility gap is also calculated and shown as dashed line.

Chapter 6. KINETIC MODELING OF CONSTITUTIONAL LIQUATION IN AL-CU ALLOYS

6.1. Background

The mechanism of constitutional liquation was first proposed by Pepe and Savage [4] to interpret the heat-affected zone (HAZ) hot cracking in weldments, a phenomenon existing in many commercial alloy systems. It is defined as the sub-solidus, non-equilibrium local eutectic melting of chemically heterogeneous regions of the matrix, e.g. second-phase particles or inclusions. It is a non-equilibrium phenomenon in that at the temperature where constitutional liquation occurs, the second phase and the liquid phase are not stable in the alloy. However, due to the rapid heating rate experienced during welding operations, the second-phase particles may not be dissolved completely at the time the eutectic temperature is reached in the HAZ. Metastable liquid may thus nucleate heterogeneously at the interfaces between the remaining second-phase particles and the matrix, followed by rapid melting of the second-phase particles and part of the surrounding matrix. After prolonged annealing, the metastable liquid droplets will slowly dissolve back into the surrounding matrix, the rate of which is controlled by the volume diffusion in the matrix.

In this chapter, the diffusion processes of both the solid-state dissolution and the constitutional liquation in the model Al-Cu alloy system are computationally investigated using the DICTRA program [15] coupled with critically assessed thermodynamic and

kinetic databases. In order to avoid constitutional liquation, all the second-phase particles in the HAZ have to be completely dissolved before reaching the eutectic temperature during the heating cycle. Based on this criterion, computer simulations were conducted under the condition of constant heating rate to obtain the critical heating rates, beyond which constitutional liquation will occur, for a series of Al-Cu alloys with different compositions and θ (Al_2Cu) precipitate sizes. The relationship between the microstructure of an alloy and its critical heating rate is thus quantitatively established.

6.2. Literature Review

The solid-state dissolution and constitutional liquation of the θ phase in binary Al-Cu alloys were experimentally studied by Reiso *et al.* [93] and Wilson [94]. In both studies, samples consisting of intragranular θ precipitates dispersed in the Al-rich fcc (α) matrix were rapidly heated to temperatures both below and above the eutectic temperature of 547°C, followed by isothermal holding at that temperature for various periods of time. Their experimental conditions are listed in Figure 6.1. The samples were then air-cooled by Reiso *et al.* [93] and water-quenched by Wilson [94]. Both used optical and SEM microscopy coupled with quantitative image analysis tools to examine the area fraction and surface number density of the θ particles and the eutectic regions in the quenched samples. In both studies, particles on the grain boundaries were excluded from the measurements. The chemical compositions of various phases were measured by Reiso *et al.* [93] and Wilson [94] using wavelength dispersive spectrometer (WDS) and electron probe microanalysis (EPMA), respectively.

In both studies, it was experimentally observed that at temperatures below the eutectic temperature, i.e. 535°C and 546°C, only solid-state dissolution of the intragranular θ precipitates in the α matrix occurred. While at temperatures above the eutectic temperature but still below the solidus, i.e. 555°C, 565°C and 585°C, the θ precipitates melted rapidly (~1 second) together with part of the surrounding α matrix, producing spherical liquid droplets in the matrix. After sufficiently long annealing, the liquid droplets were redissolved by the surrounding matrix and the final microstructure consisted of single-phase α grains only.

However, in Reiso *et al.* [93]'s air-cooled samples annealed at 555°C, most liquid droplets solidified into lamellar eutectic structures, only few particles were featureless, i.e. without any internal structure. While in Wilson [94]'s water-quenched samples, vast majority of the solidified droplets appeared uniform in contrast and had no internal structure. Only few exhibited lamellar eutectic structure. Reiso *et al.* [93] found the compositions of the particles without internal structure always to be 54 wt.% Cu, indicating that they are pure θ particles. This was confirmed by Chattopadhyay *et al.* [95]'s microhardness measurements in their study of the solidification behavior of the Al-Cu liquid droplets embedded in an α matrix. However, Wilson [94] measured the composition of the solidified droplets with no internal structure to be 45.5±2.2 wt.% Cu, much lower than the expected 54 wt.% Cu. This may be due to the inadvertent contributions from the surrounding α matrix when doing EPMA measurements since the θ particles in Wilson [94]'s study are rather small.

As shown in Figure 6.1, the measured eutectic compositions in Reiso *et al.* [93]'s samples fall in a range from 35 to 43 wt.% Cu with a weighted average of 38.25 wt.% Cu, considerably higher than the anticipated equilibrium eutectic composition of 33 wt.% Cu. From the calculated metastable α liquidus shown in Figure 6.2, this average composition of 38.25 wt.% Cu corresponds to a large undercooling of 27°C of the liquid phase. Chattopadhyay *et al.* [95] and Kim and Cantor [96] both experimentally measured the undercooling of liquid droplets embedded in an α matrix. Their experimental results are given in Table 6.2. As can be seen, present prediction of the undercooling agrees well with the experimental observations.

The large undercooling of liquid below the eutectic temperature indicates a difficulty of heterogeneous nucleation of the θ precipitates at the α/liquid interface during solidification. As the liquid droplets undercool below the eutectic temperature without nucleation of the θ phase, the α phase continues to grow epitaxially from the pre-existing matrix, i.e. with the same crystal orientation as the matrix, and consumes part of the liquid phase. The compositions of the liquid droplets and the newly formed α phase will follow the metastable α liquidus and solidus (see Figure 6.2), respectively, in order to maintain local equilibrium at the α/liquid interface. As the liquid droplets decrease in size, they get more and more enriched in Cu. At some critical undercooling, the θ phase forms, and the remaining liquid droplets solidify either into a lamellar eutectic structure or into a divorced eutectic structure in which the newly formed α phase grows on the α matrix. As newly formed α phase has a higher Cu concentration, as shown in Figure 6.2, there must exist a Cu concentration gradient in the matrix surrounding the solidified

particles. This has been experimentally observed by Reiso *et al.* [93] and Chattopadhyay *et al.* [95] using aging technique and by Wilson [94] using secondary electron and Cu-K_α x-ray mapping. Wilson [94] also determined the composition of the Cu-rich region surrounding the solidified θ particles in the matrix to be 5.2 wt.% Cu.

However, in Reiso *et al.* [93]'s experiment in which a sample was quenched in air slightly before the temperature 555°C was reached, the compositions of the eutectic particles are always in the range of 32-34 wt.% Cu, i.e. around the equilibrium eutectic composition of 33 wt.% Cu. This is because in this sample, the θ particles were only partially melted and therefore eliminated the need for new nucleation of the θ phase during solidification. The liquid thus solidified into a coarse eutectic structure without any undercooling. It was observed that nucleation of liquid tends to start heterogeneously at the end of the lenticular θ particles. This can be well understood from the classical nucleation theory since the α/θ interfacial energy is higher at those parts, and therefore lower energy barrier for liquid nucleation.

6.3. Computer Modeling

6.3.1. Thermodynamic Data

For studying constitutional liquation in Al-Cu system, the existing COST 507 [23] database suffices since only the Gibbs energies of fcc, liquid and θ phases are needed. Their Gibbs energies can be found in Table 5.1.

Figure 6.2 shows the Al-rich corner of the Al-Cu phase diagram calculated by Thermo-Calc. The Gibbs energy curves of liquid, fcc and θ phases at 565°C are plotted in Figure 6.3. The thermodynamic driving force ΔG for constitutional liquation reaction θ + α = Liquid is graphically shown in Figure 6.3 and calculated as a function of temperature in Figure 6.4, which is approximately a linear function of temperature and is zero at the eutectic point.

6.3.2. DICTRA Simulations

Sharp-Interface model, combined with local equilibrium assumption, proves to be a very powerful tool for the simulation of diffusion-controlled phase trans-formations. The finite-difference code DICTRA [15], a program for simulating one-dimensional diffusion-controlled phase transformations in multi-component alloy systems, was used in the present work. Only simple geometries, i.e. planar, cylindrical or spherical, can be treated. DICTRA is interfaced with Thermo-Calc [14], which handles all the thermodynamic calculations needed by DICTRA, e.g. thermodynamic factors for calculating interdiffusion coefficients and local equilibrium conditions at the phase interfaces. As illustrated in Figure 6.5, typical DICTRA simulations are performed in the following four steps:

1) Calculate the local thermodynamic equilibrium at the phase interface.
2) Solve the multi-component diffusion equations using the finite-difference method.
3) Solve the flux balance equations and obtain the interfacial velocity.

4) Displace the phase interfaces and update all the grid points to their new positions.

DICTRA simulations are performed using the concept of cells. The cell constructions for the present simulations are shown in Figure 6.6. Spherical geometry was used in the present study, which best approximates the actual geometry of the problem. Soft impingement of neighboring diffusion fields is automatically taken into account in the simulations by setting the external cell boundaries to be closed, i.e. zero-flux. Local equilibrium is assumed at all the phase interfaces inside the cell. Since the interface between the θ and α phases is incoherent and mobile, local equilibrium is a good assumption here. This implies that the reaction kinetics is governed by volume diffusion in the α and liquid phases.

Based on absolute-reaction rate theory, the composition-dependent atomic mobilities of Al and Cu in the α phase are represented by the following Arrhenius-type equation:

$$M_i = \frac{M_i^o}{RT}\exp\left(\frac{-Q_i}{RT}\right) \tag{6.1}$$

where M_i is the atomic mobility of element i in the α phase, M_i^o is the frequency factor and Q_i is the activation energy. By defining $\Phi_i = -Q_i + RT\ln M_i^o$, the mobility can then be written as:

$$M_i = \frac{1}{RT}\exp\left(\frac{\Phi_i}{RT}\right) \tag{6.2}$$

In the spirit of the CALPHAD approach, the composition-dependence of Φ_i is expressed in a form similar to Eq. (2.4):

$$\Phi_i = x_{Al}\Phi_i^{Al} + x_{Cu}\Phi_i^{Cu} + x_{Al}x_{Cu}\sum_{k=0}^{n} {}^{k}\Phi_i^{Al,Cu}\left(x_{Al} - x_{Cu}\right)^k \tag{6.3}$$

where Φ_i^j is the mobility parameter of element i in pure j, taken from the DICTRA MOB2 database and shown in Table 6.3. ${}^{k}\Phi_i^{Al,Cu}$ are the interaction parameters for element i and are zero for both Al and Cu.

The composition-dependent interdiffusion coefficient in the α phase can then be calculated using Darken's equation:

$$\widetilde{D} = (x_{Al}M_{Cu} + x_{Cu}M_{Al})x_{Al}x_{Cu}\frac{d^2G_m^{\alpha}}{dx_{Cu}^2} \tag{6.4}$$

In lack of experimental information, the interdiffusion coefficient in the liquid phase was assumed to have a constant value of 10^{-9} m^2/s. Diffusion in the θ phase was neglected in all present simulations.

6.4. Results

6.4.1. Simulation of Isothermal Holding

Table 6.4 gives the initial conditions for DICTRA simulations used in the present study to reproduce Wilson [94] and Reiso *et al.* [93]'s experimental conditions. The initial compositions in the θ and α phase were set to be uniform. The average θ particle radius r_θ was reported by Wilson to be 1.65μm. r_θ in the study by Reiso et al. was estimated as follows:

$$r_\theta = \sqrt{\frac{3f_\theta}{2\pi N_A}} \tag{6.5}$$

where f_θ and N_A are the measured volume fraction and surface number density of θ listed in Table 6.1, respectively. The thickness of the surrounding α matrix was calculated by mass balance such that the overall composition corresponds to that of the alloy.

Using the initial conditions given in Table 6.4, the isothermal solid-state dissolution of the θ phase at 535°C and 546°C without liquation were simulated. The simulated results agree very well with experimental data, as shown in Figure 6.7 to Figure 6.9. As a further check of the validity of the present simulations, the compositional profile in the α matrix on both sides of a dissolving θ plate was simulated by DICTRA and compared with Hall

[97]'s experimental observations. As shown in Figure 6.10 and Figure 6.11, the agreement with experiments is quite good.

Constitutional liquation at 555°C, 565°C and 585°C, all below the solidus but above the eutectic temperature, were then simulated. The concentration profiles during constitutional liquation at 565°C are shown in Figure 6.12 with arrows indicating the direction of interface movement at different times. As can be seen from the simulation, within 1 second, the θ particle transformed into the liquid phase together with part of the surrounding α matrix and the liquid composition quickly homogenized to the equilibrium liquidus composition. As soon as the composition of the liquid phase reached the liquidus composition, the liquid phase began to shrink, the rate of which is controlled by the diffusion rate of Cu in the α matrix. The same is true for the other two temperatures. The variations of liquid volume fractions with time are also plotted in Figure 6.13 to Figure 6.15 for the three different temperatures with the experimental data superimposed. It seems that DICTRA simulations give higher liquid volume fractions than those observed by experiments. This large discrepancy is due to the fact that all experimental measurements of the high temperature liquid volume fractions were made on solidified microstructures. However, the actual size and morphology of the liquid as it existed at the annealing temperature may be changed dramatically during cooling. The final solidified microstructure depends both on the cooling rate and the nucleation of the θ phase. As schematically shown in Figure 6.16, first the proeutectic α' will grow epitaxially from the pre-existing matrix, decreasing the size of the liquid phase and make it more and more enriched in Cu. At some critical undercooling, the remaining liquid droplets L' may either

solidify into a lamellar eutectic structure $\alpha_E + \theta_E$, as in Reiso *et al.* [93]'s case, or into a divorced eutectic structure $\alpha'' + \theta$, as in Wilson [94]'s case. In quantifying the solidified liquid droplet volume fraction, only those regions in the matrix delineated by the θ particles, i.e. lamellar eutectic structures and pure θ precipitates, are actually measured since both α'' and the proeutectic α' are physically and optically indistinguishable from the pre-existing α matrix.

In order to compare the DICTRA simulated results with the experimental measurements by Reiso *et al.* [93], the solidification of liquid from the annealing temperature of 555°C after isothermal holding at that temperature for 1, 10 and 100 seconds was simulated suppressing formation of the θ phase. A cooling rates of 1°C/sec was used to mimic the air-cooling conditions by Reiso *et al.* [93]. The simulated results are given in Figure 6.17 together with results from Scheil simulation by Thermo-Calc [14], which assumes infinite fast diffusion in the liquid and no diffusion in the solid. A high cooling rate of 100°C/sec was also simulated to reproduce Wilson [94]'s water-quenching condition. However, this gives results identical to those from Scheil simulation, as expected. In Figure 6.18, the Cu concentration profiles during the solidification of the liquid phase are also shown at 0, 20 and 40 seconds after 10 seconds of isothermal holding at 555°C. As can be seen, the liquid phase decreases in size with time and at the same time get more and more enriched in Cu. Using the average eutectic composition of 38.25 wt.% Cu from Reiso *et al.* [93], it can be obtained from Figure 6.17 that about 71 percent of original liquid at annealing temperature of 555°C transformed into eutectic structure, the rest goes to proeutectic α'. Therefore, Reiso *et al.* [93]'s experimental data at 555°C were divided by a factor of 0.71

and compared with DICTRA simulations in Figure 6.19. A good agreement was observed after the correction.

As for Wilson [94]'s case, most liquid droplets in the water-quenched samples solidified into a structure consisting of proeutectic α' and divorced eutectic α" + θ, as shown in Figure 6.16(b). Since DICTRA and Scheil simulations give the same results for the case of high cooling rate, for simplicity, Scheil simulations were performed using Thermo-Calc to simulate the solidification of liquid from annealing temperature 565°C and 585°C without formation of the θ phase, respectively. The starting composition of the liquid phase was set to be the equilibrium liquidus composition at the respective annealing temperature. Figure 6.20 shows the simulated volume fraction of liquid transformed into proeutectic α', $f_{\alpha'}$, with respect to the liquid undercooling at both temperatures. At some critical undercooling, the remaining liquid L' then transformed into divorced eutectic α" + θ. Using the level rule, the volume fraction of liquid actually transformed into the θ phase, f_{θ}^{L}, can thus be calculated as follows:

$$f_{\theta}^{L} = (1 - f_{\alpha'}) \frac{x_{L'} - x_{\alpha''}}{x_{\theta} - x_{\alpha''}} \tag{6.6}$$

where $x_{L'}$ and $x_{\alpha''}$ are the mole fraction of Cu in L' and α", and can be read from the metastable liquidus and solidus in Figure 6.2 for a given undercooling, respectively. x_{θ} is the mole fraction of Cu in the θ phase and has a value of 0.333. In Figure 6.21, f_{θ}^{L} is plotted as a function of liquid undercooling for both temperatures. It can be seen that the

value of f_θ^L is almost constant over a large range of undercooling. In our calculations, we assume the same undercooling as in Reiso *et al.* [93]'s case, i.e. 27°C. The final results are given in Table 6.5. Wilson [94]'s experimental data at 565°C and 585°C were then divided by the corresponding f_θ^L value in Table 6.5 and compared with DICTRA simulations in Figure 6.22 and Figure 6.23, respectively. Both DICTRA simulations agree very well with experimental measurements after the correction.

6.4.2. Simulation of Continuous Heating

The critical heating rate to avoid constitutional liquation was further studied through DICTRA simulations. The initial compositions and volume fractions of the α and θ phases were calculated by Thermo-Calc at the room temperature for a series of alloys with composition 1, 2, 3, 4 and 5 wt.% Cu, which serve as inputs to DICTRA simulations. A linear heating profile, i.e. T=25°C+κt, was used in the present study though other types of nonlinear heating profiles can also be used. Here t is time in seconds and κ is the constant heating rate (°C/sec). The critical heating rate can thus be defined as the maximum κ at which the θ particle is completely dissolved into the matrix before the eutectic temperature is reached. Simulations are then performed for each alloy by choosing different initial precipitate sizes for the θ particle and different constant heating rates. The obtained critical heating rate for each alloy is plotted as a function of the precipitate size in Figure 6.24. A linear relationship is observed when we use the logarithmic scale for both axes. Using linear regression, it is found that the critical

heating rate κ is inversely proportional to the square of the precipitate size for each alloy, i.e.

$$\kappa_c = \frac{c}{r_0^2} \tag{6.7}$$

where r_0 is the initial precipitate size, in μm, κ_c is the critical heating rate beyond which constitutional liquation will occur, c is a constant depending on the alloy composition and its value is given in Figure 6.24 for each alloy.

The relationship observed in our numerical simulations can be qualitatively explained by the analytic quasi steady-state solution derived by Frade and Cable [98], which for dissolution of spherical particle in infinite matrix gives:

$$\kappa(r_0^2 - r^2) = \int_{T_1}^{T_2} f(T)dT \tag{6.8}$$

where κ is the constant linear heating rate, T_1 and T_2 are the starting and ending temperature, respectively, f(T) is a function of temperature, and r is the particle radius at the time the temperature reaches T_2. When T_1 and T_2 are fixed to be the room temperature and eutectic temperature, respectively, as in the present case, the right hand side of Eq. (6.8) is a constant. At the critical heating rate, r=0, we thus obtain the relationship $\kappa_c \propto \frac{1}{r_0^2}$, which is consistent with Eq. (6.7).

6.5. Summary

In this chapter, all stages of constitutional liquation were simulated by DICTRA using realistic thermodynamic and kinetic databases. Quantitative agreement had been observed between computer simulations and experimental observations. The relationship between the high temperature liquid droplets and the room temperature solidified microstructure was quantitatively clarified in this study through the consideration that the liquid droplets can either transform into the lamella structure or into the divorced eutectic structure during solidification. The computational procedures for obtaining the critical heating rate to avoid constitutional liquation are demonstrated. We conclude that, constitutional liquation depends both on the heating rate and the average precipitate size in the HAZ. Rapid heating rate and large precipitate size will both promote constitutional liquation. The critical heating rate for avoiding liquation was simulated and found to be inversely proportional to the square of the precipitate size. The present computational procedures can be readily extended to predict the susceptibility of multicomponent commercial alloys to constitutional liquation during welding with available thermodynamic and kinetic databases.

Table 6.1. Experimental conditions.

Source	Composition (wt.% Cu)			θ Volume Fraction	θ Surface Density ($1/\mu m^2$)	Temperature (°C)
	Total	θ	α			
Reiso [93]	4.2	54	3.1	0.015	0.00020	546, 555
Wilson [94]	3.2	52.6	1.7	0.0217	0.00272	535, 565, 585

Table 6.2. Experimental measurements of liquid undercooling.

Source	Alloy Composition (wt.% Cu)	Cooling Rate (°C/min)	Undercooling (°C) $\Delta T=T_{eut}-T$
Chattopadhyay [95]	3.8	4-7	19-28
Kim and Cantor [96]	7	0.5-20	16-25

Table 6.3 Kinetic parameters of the Al-Cu system. Activation energies are in J/mol and frequency factors are in m^2/s, T is in K.

Fcc: (Al,Cu)

Mobility of Al

$$\Phi_{Al}^{Al} = -142000 + RT\ln(1.71\times10^{-4})$$

$$\Phi_{Al}^{Cu} = -181300 + RT\ln(8\times10^{-6})$$

Mobility of Cu

$$\Phi_{Cu}^{Al} = -135100 + RT\ln(6.47\times10^{-5})$$

$$\Phi_{Cu}^{Cu} = -201000 + RT\ln(2.59\times10^{-5})$$

Table 6.4. Initial conditions for DICTRA simulations.

Study	Composition (wt.% Cu)		Size (μm)		Temperature (°C)
	θ	α	r_θ	w_α	
Reiso [93]	54	3.1	5.98	18.13	546, 555
Wilson [94]	54	1.48[a]	1.65	4.15	535, 565, 585

[a]Calculated by Thermo-Calc

Table 6.5. Values used to calculate the volume fraction of liquid transformed into θ.

Temperature (°C)	Mole Fraction of Cu				Volume Fraction	
	x_L	$x_{L'}$	$x_{\alpha''}$	x_θ	$f_{\alpha'}$	f_θ^L
565	0.1518	0.2076	0.0429	0.333	0.31	0.392
585	0.1231	0.2076	0.0429	0.333	0.456	0.309

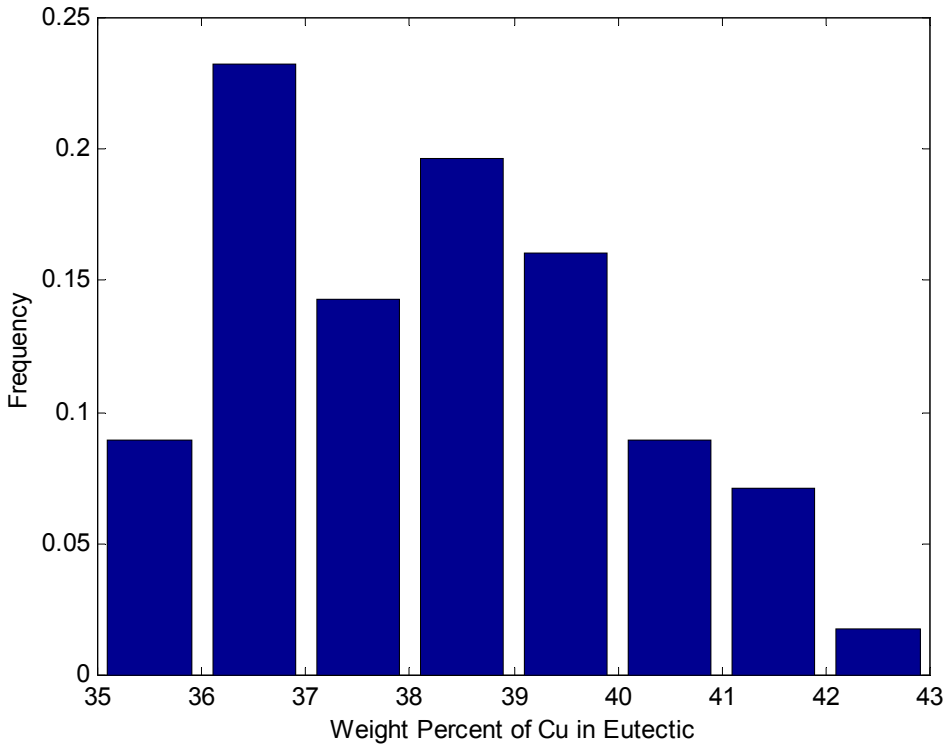

Figure 6.1. Histogram showing the frequency distribution of composition of eutectic particles from the measurements by Reiso *et al.* [93] Weighted average is 38.25 wt.% Cu.

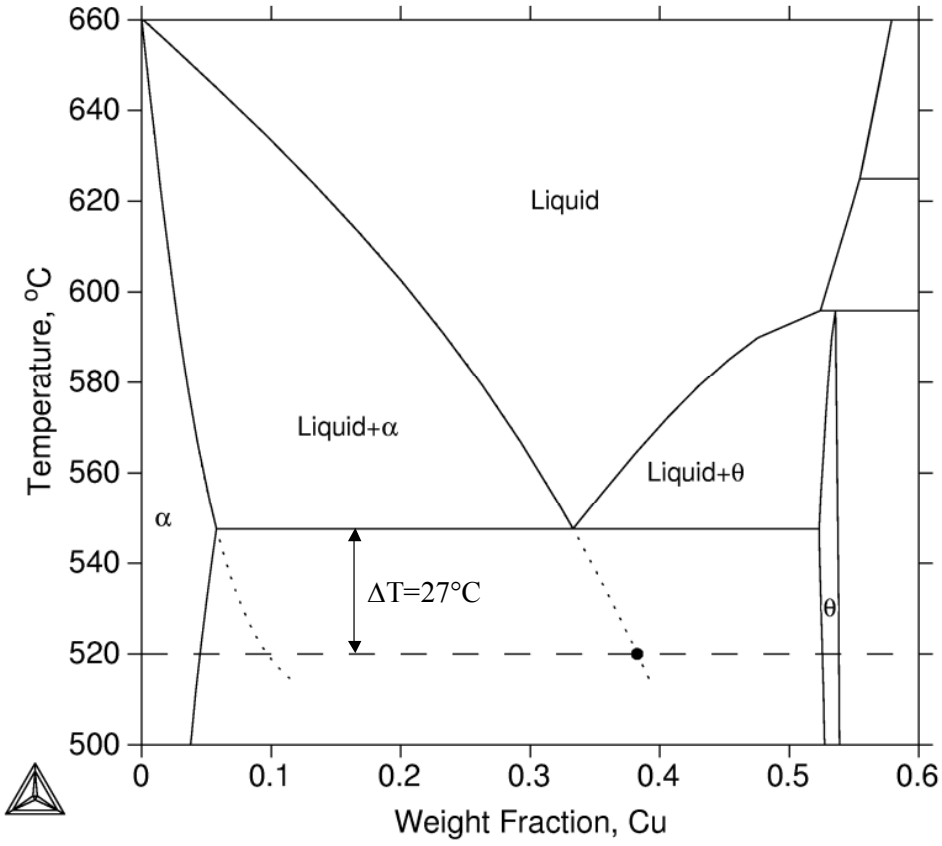

Figure 6.2. Al-rich corner of the calculated stable Al-Cu phase diagram (solid line) and the metastable liquid-fcc two-phase equilibrium (dotted line).

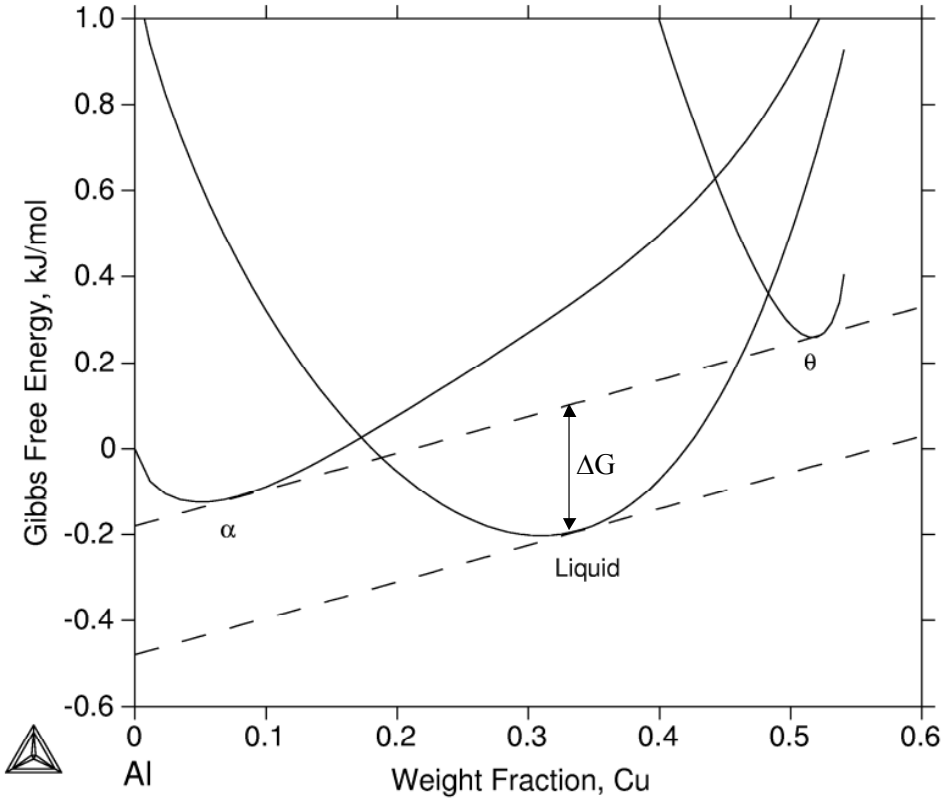

Figure 6.3. Gibbs energy curves of various phases in the Al-Cu system at 565°C. The driving force ΔG for constitutional liquation is also shown.

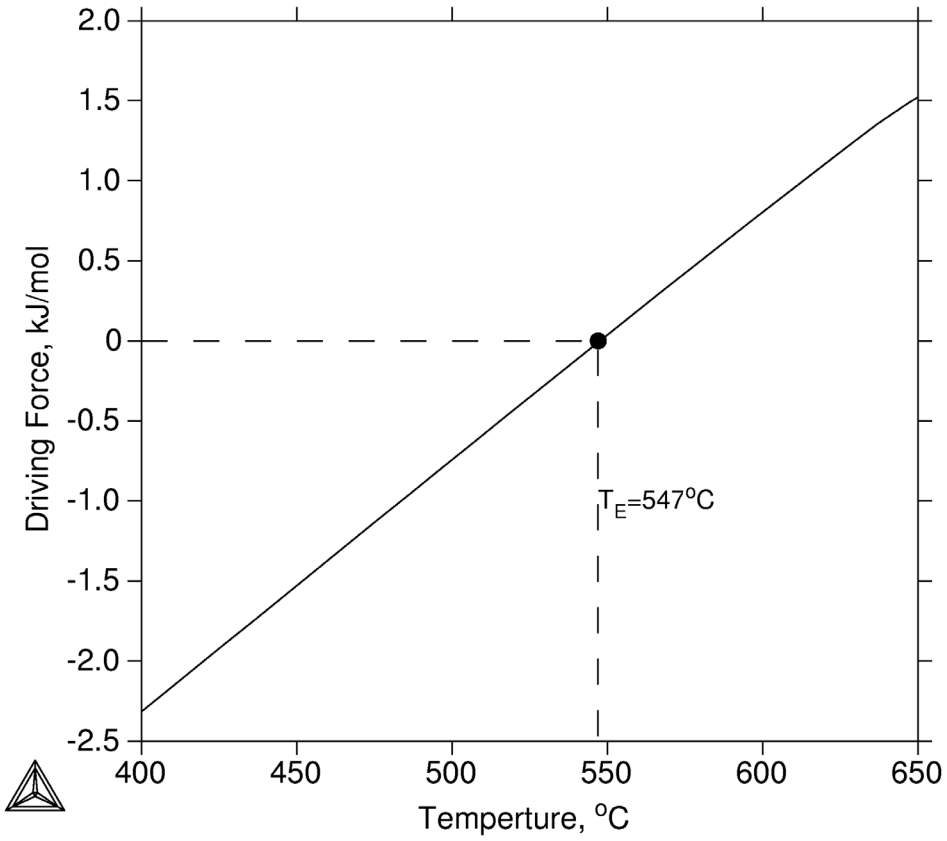

Figure 6.4. Thermodynamic driving force for constitutional liquation in the Al-Cu system calculated using the COST 507 database.

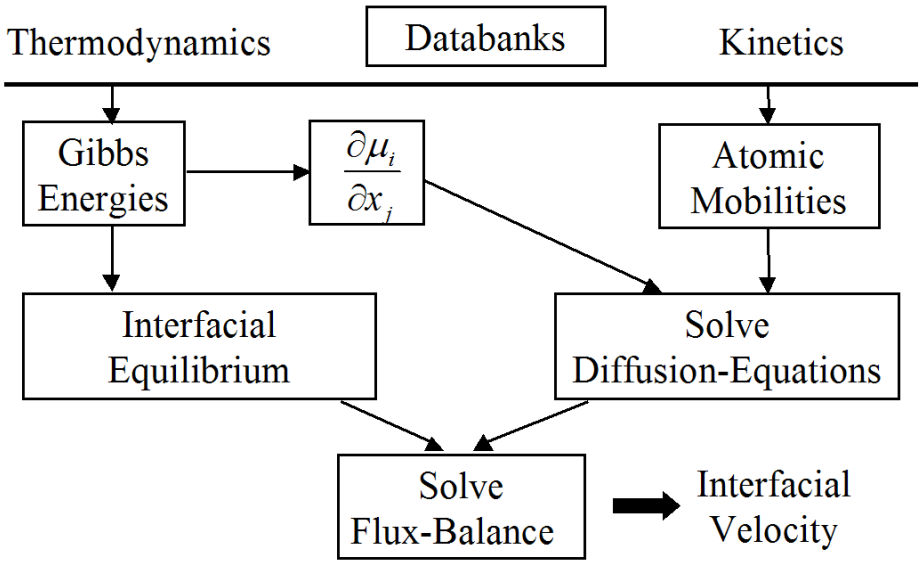

Figure 6.5. The flowchart of DICTRA simulations

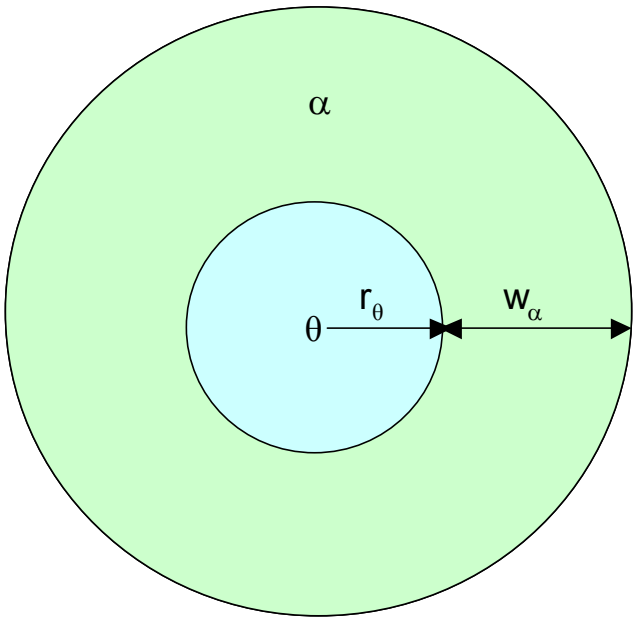

(a) Solid-state dissolution

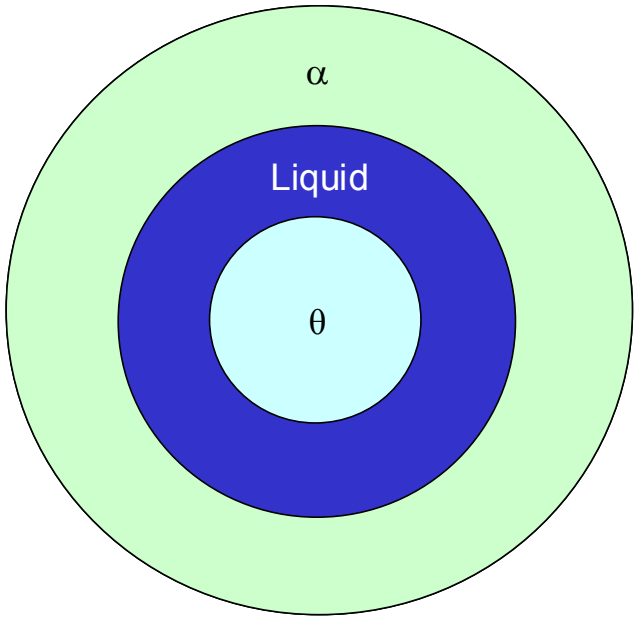

(b) Constitutional liquation

Figure 6.6. Cell setup used in DICTRA simulations.

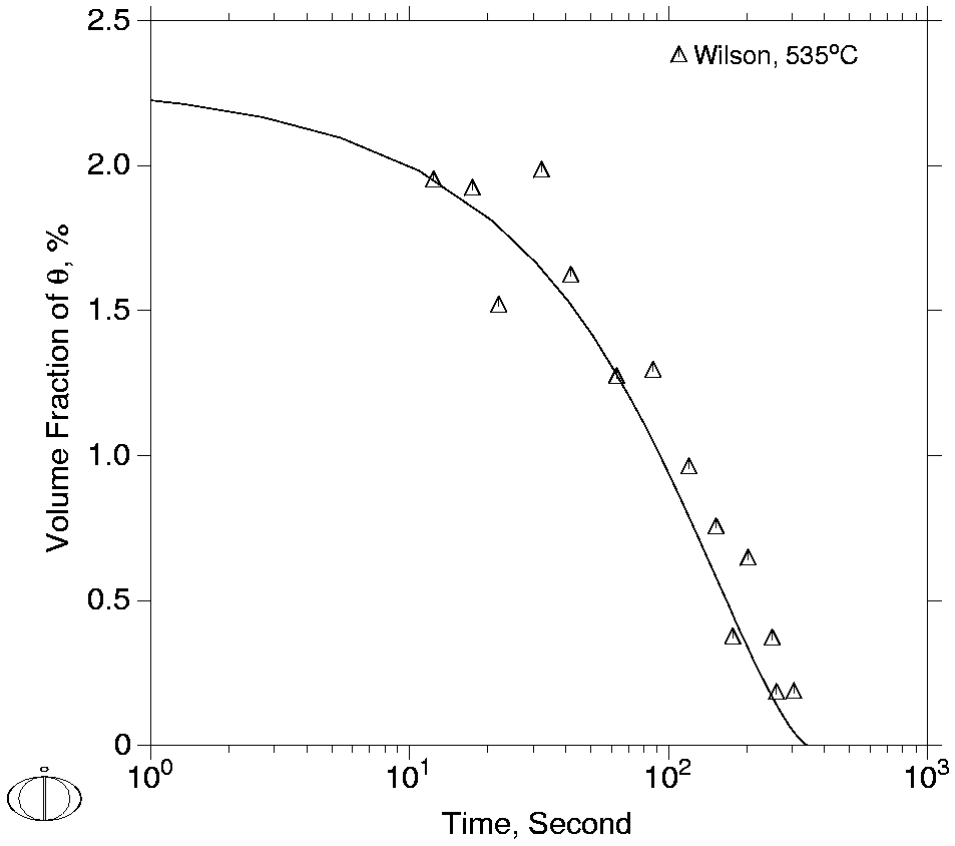

Figure 6.7. Simulated volume fraction of θ as a function of time during solid-state dissolution of θ at 535°C in comparison with the experimental data from Wilson [94].

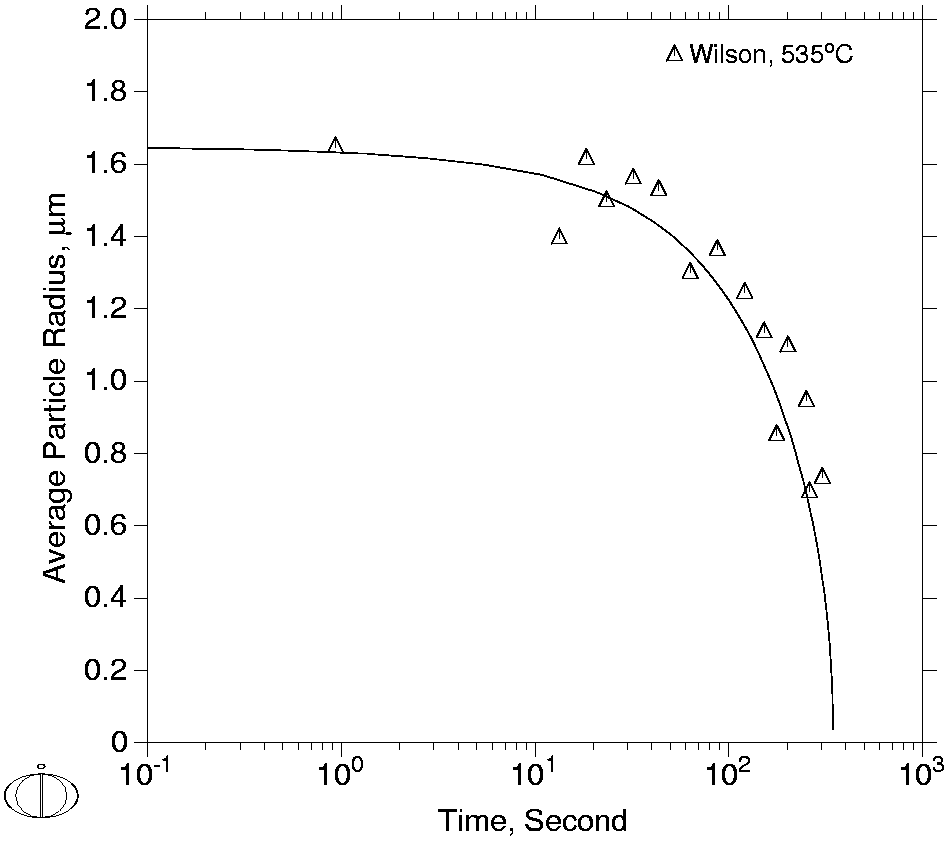

Figure 6.8. Simulated radius of the θ particles as a function of time during solid-state dissolution of θ at 535°C in comparison with the experimental data from Wilson [94].

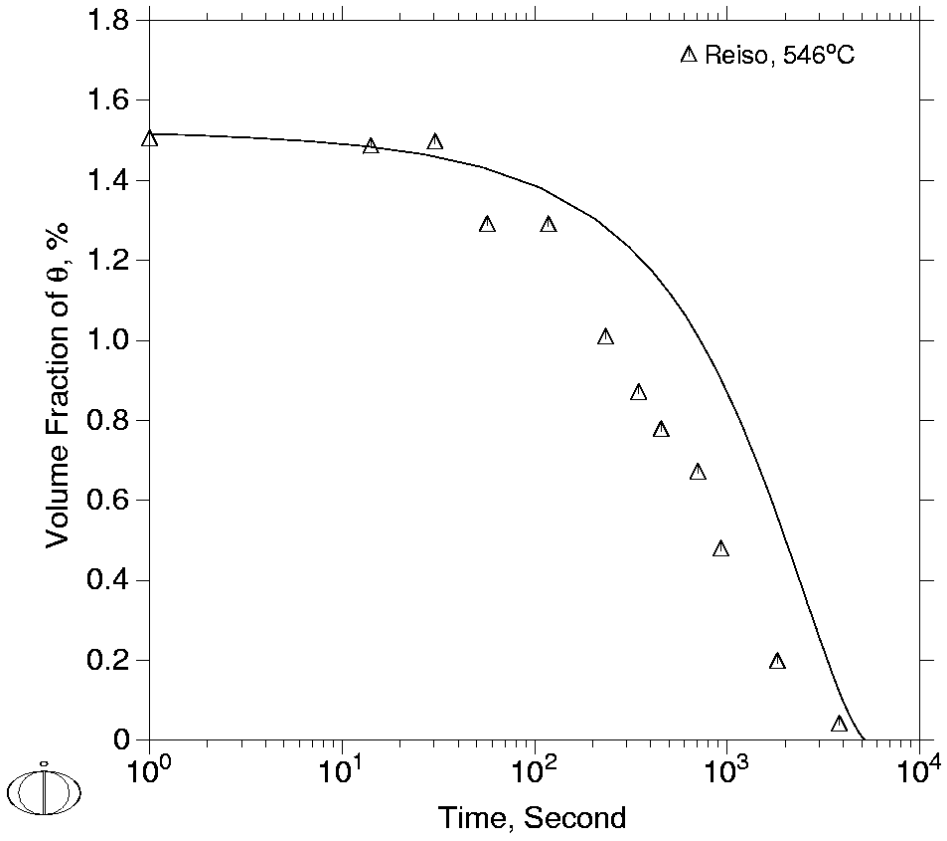

Figure 6.9. Simulated volume fraction of θ as a function of time during solid-state dissolution of θ at 546°C in comparison with the experimental data from Reiso *et al.* [93].

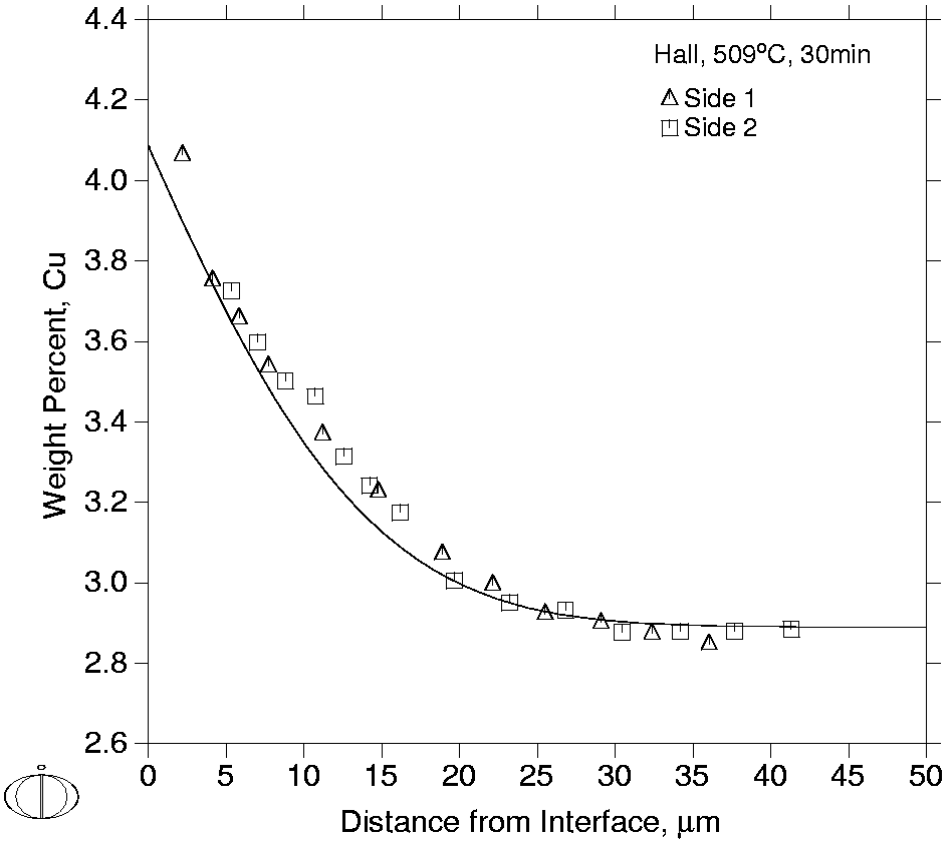

Figure 6.10. Simulated concentration profile in the α matrix at 509°C in comparison with the experimental data from Hall [97].

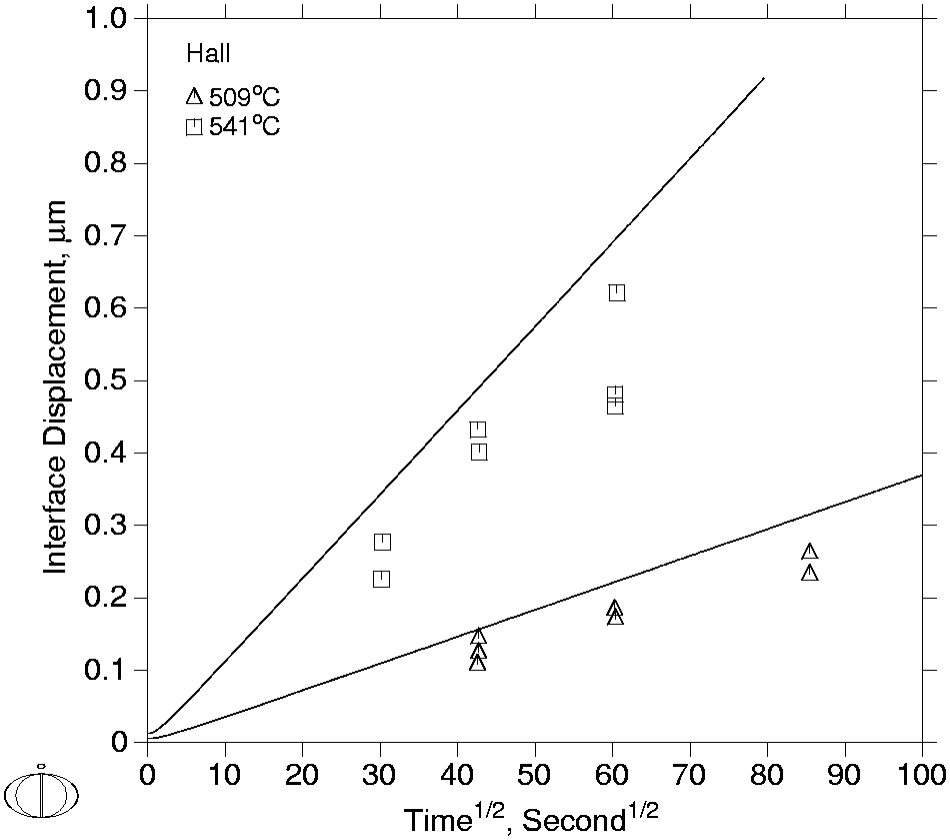

Figure 6.11. Interfacial displacement as a function of time at 509°C and at 541°C in comparison with the experimental data from Hall [97].

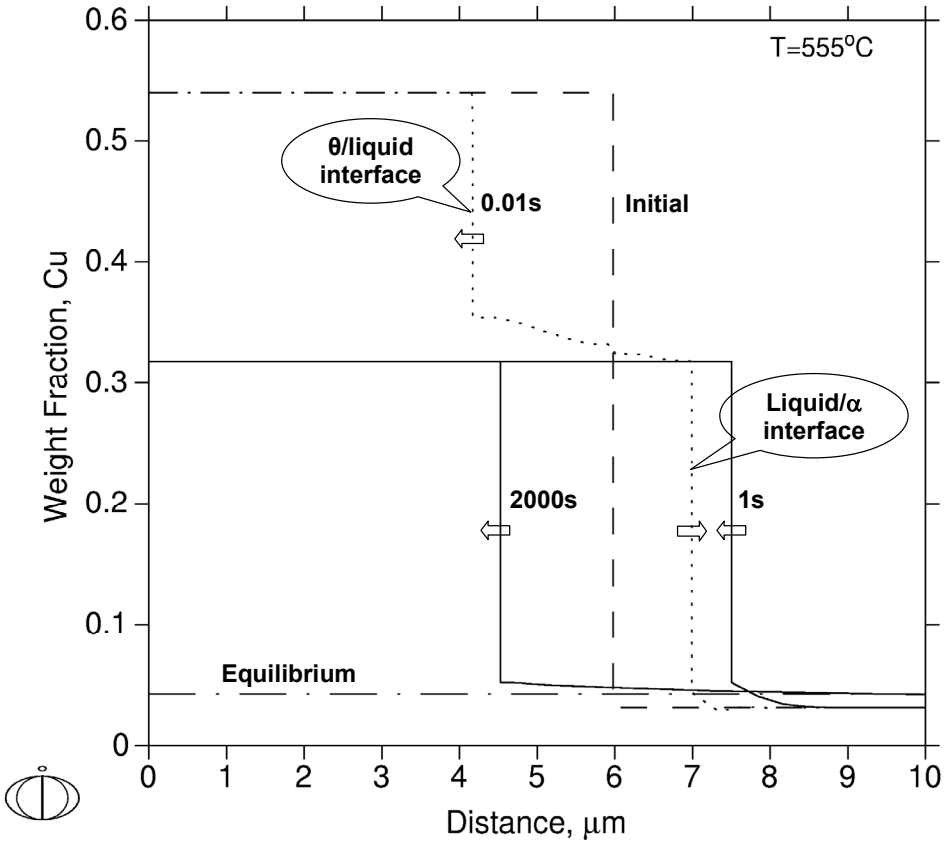

Figure 6.12. Concentration profiles during constitutional liquation at 555°C.

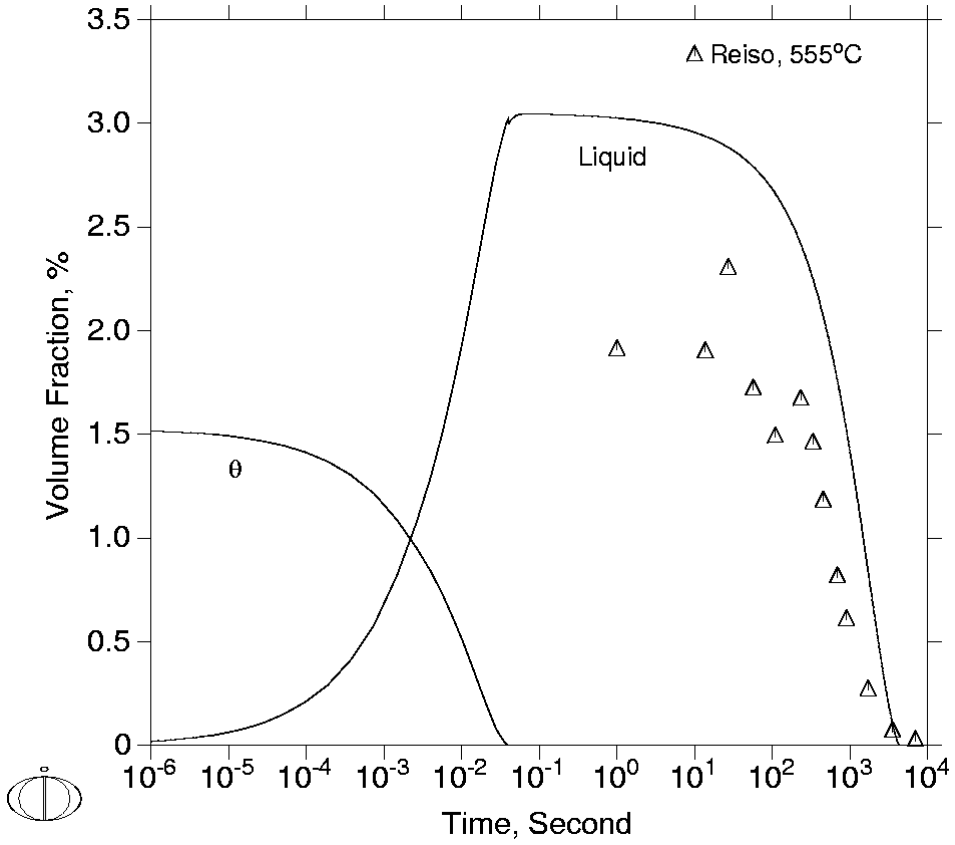

Figure 6.13. Simulated volume fraction of liquid as a function of time during constitutional liquation at 555°C in comparison with the experimental data from Reiso *et al.* [93].

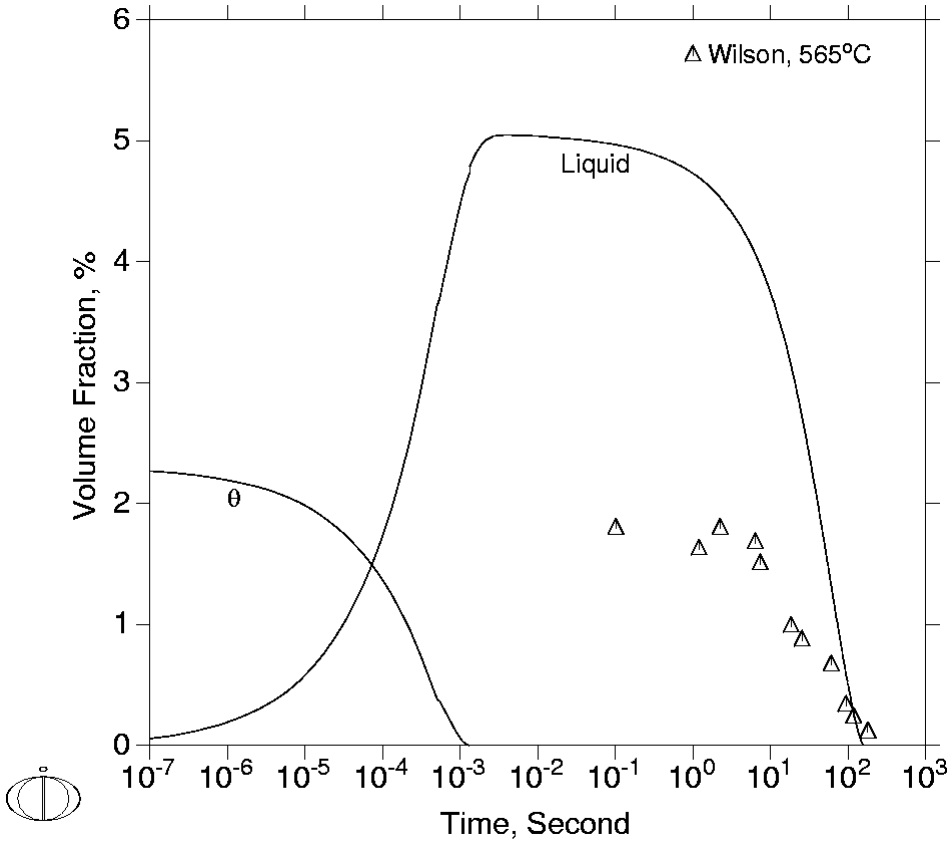

Figure 6.14. Simulated volume fraction of liquid as a function of time during constitutional liquation at 565°C in comparison with the experimental data from Wilson [94].

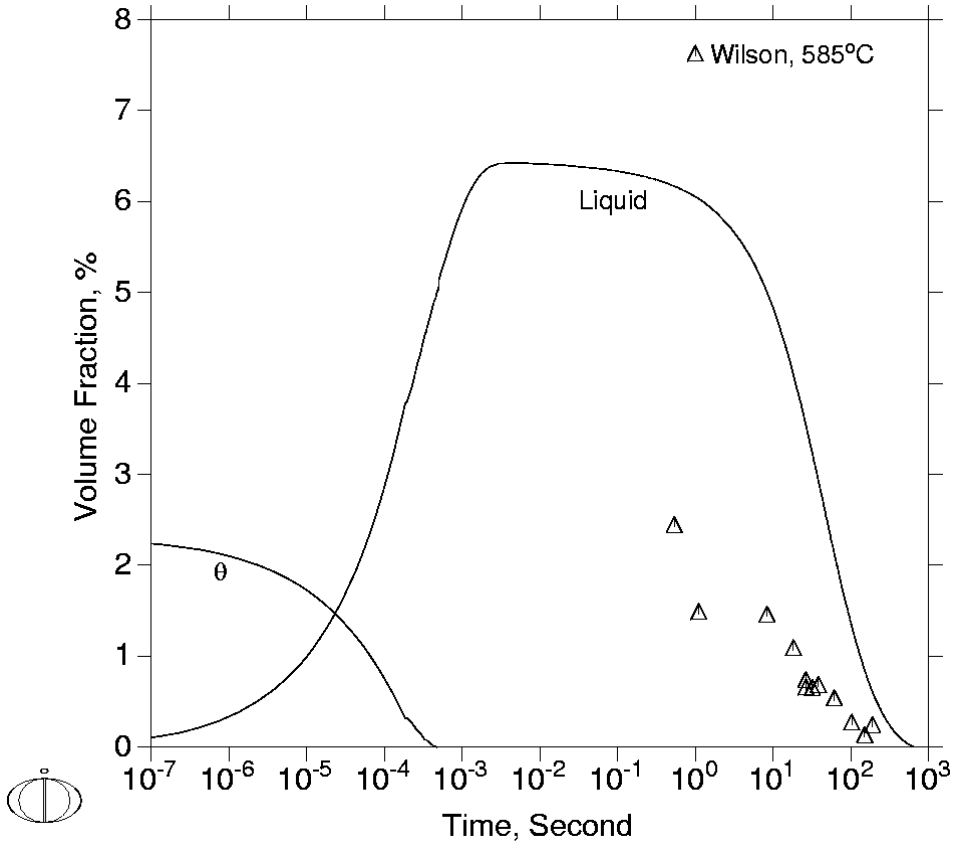

Figure 6.15. Simulated volume fraction of liquid as a function of time during constitutional liquation at 585°C in comparison with the experimental data from Wilson [94].

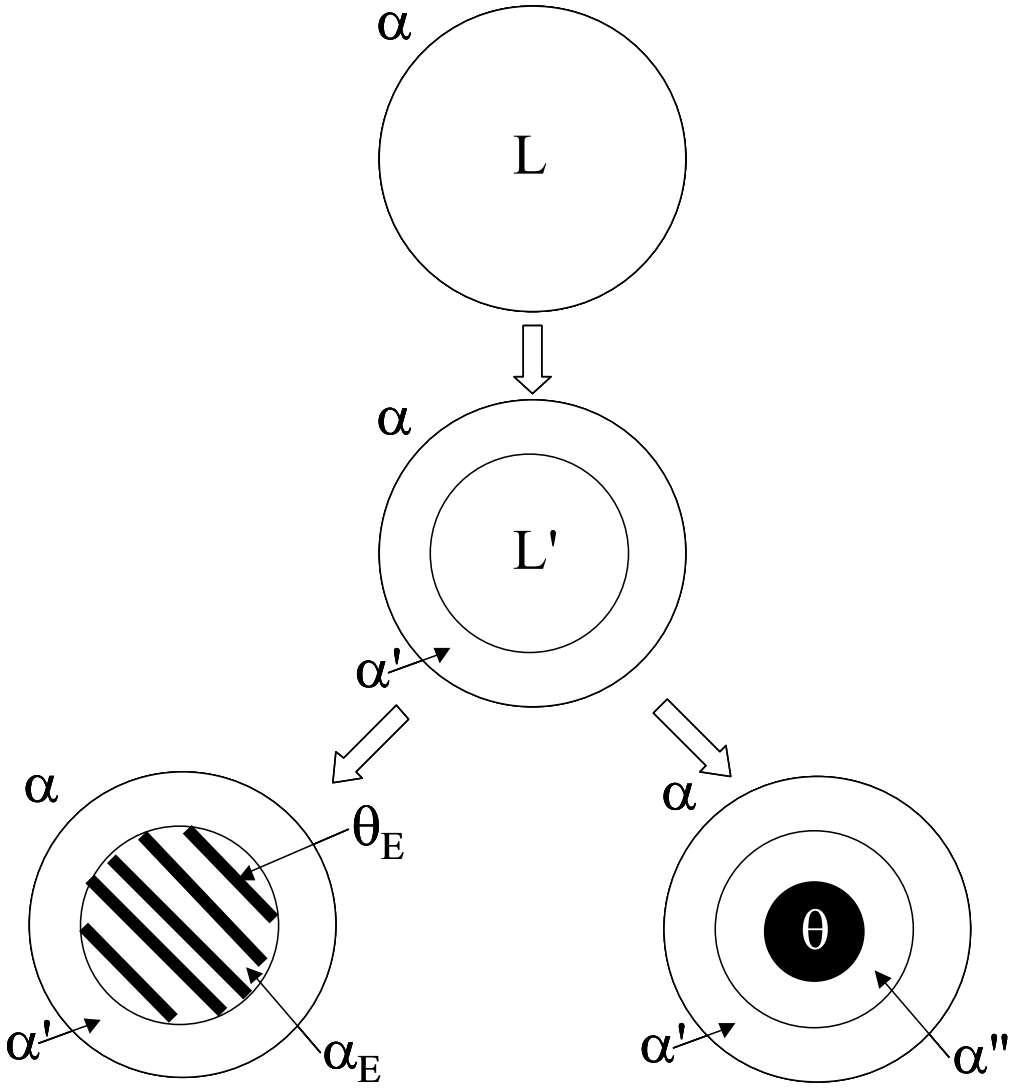

(a) Lamellar eutectic (b) Divorced eutectic

Figure 6.16. Solidification microstructure of liquid droplets.

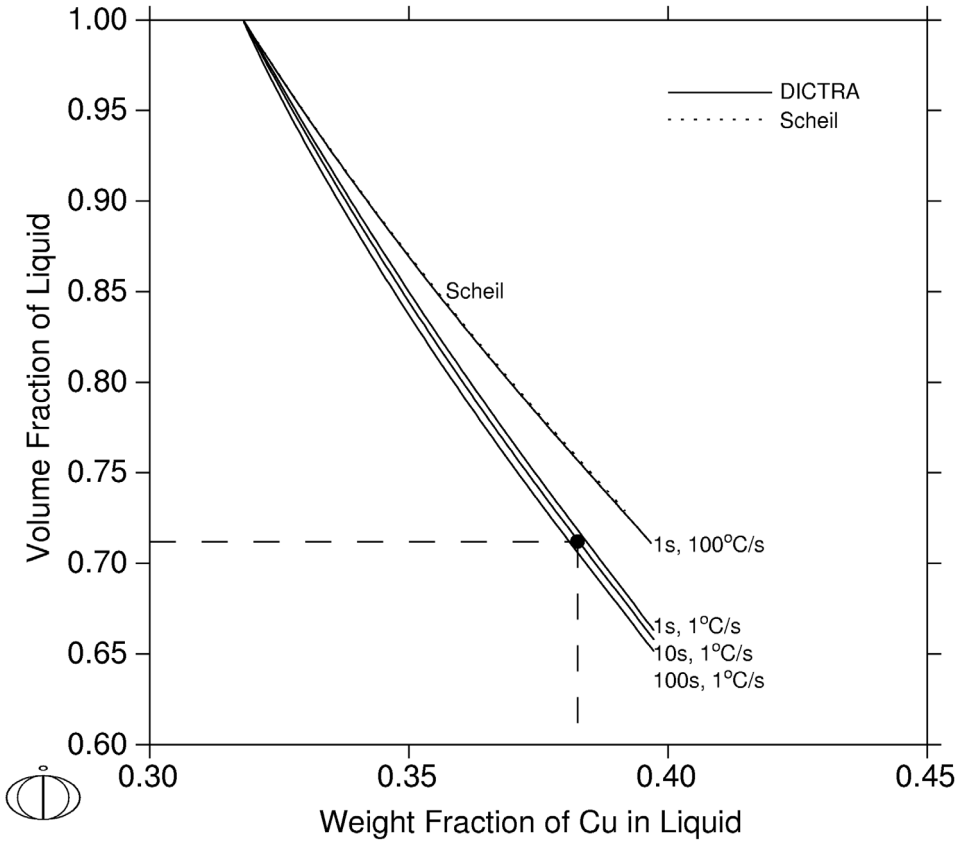

Figure 6.17. Scheil and DICTRA simulation of solidification of liquid from 555°C without formation of the θ phase.

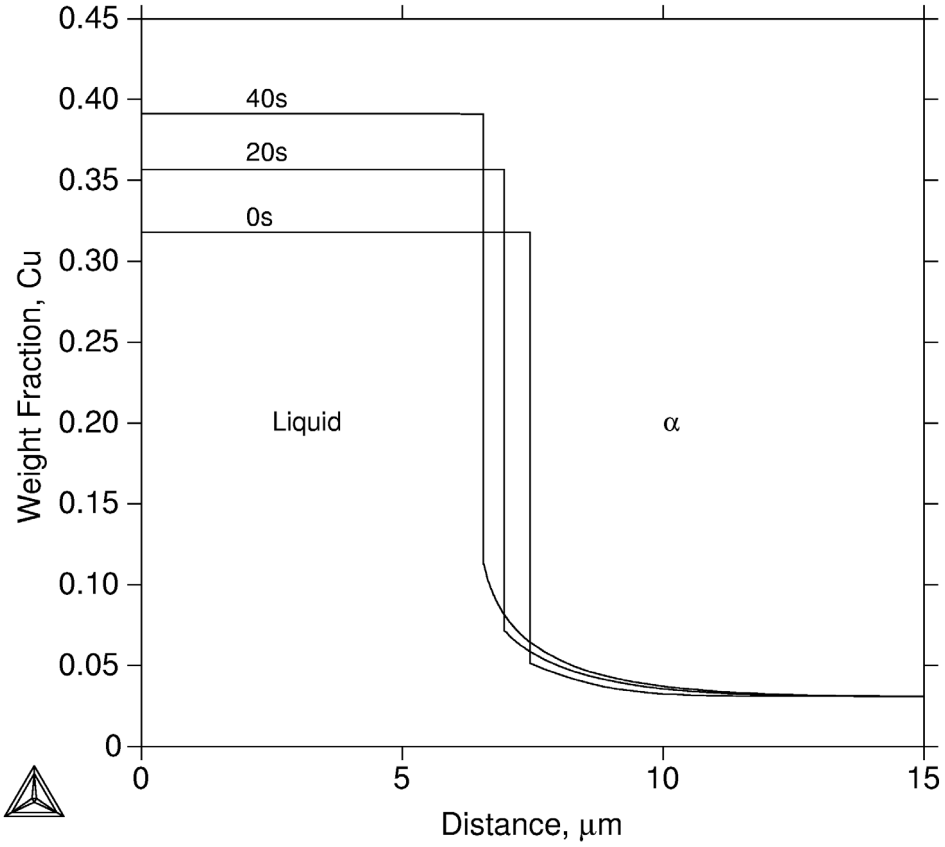

Figure 6.18. DICTRA simulation of solidification of liquid from 555°C without formation of the θ phase. Cooling Rate equals to 1°C/sec.

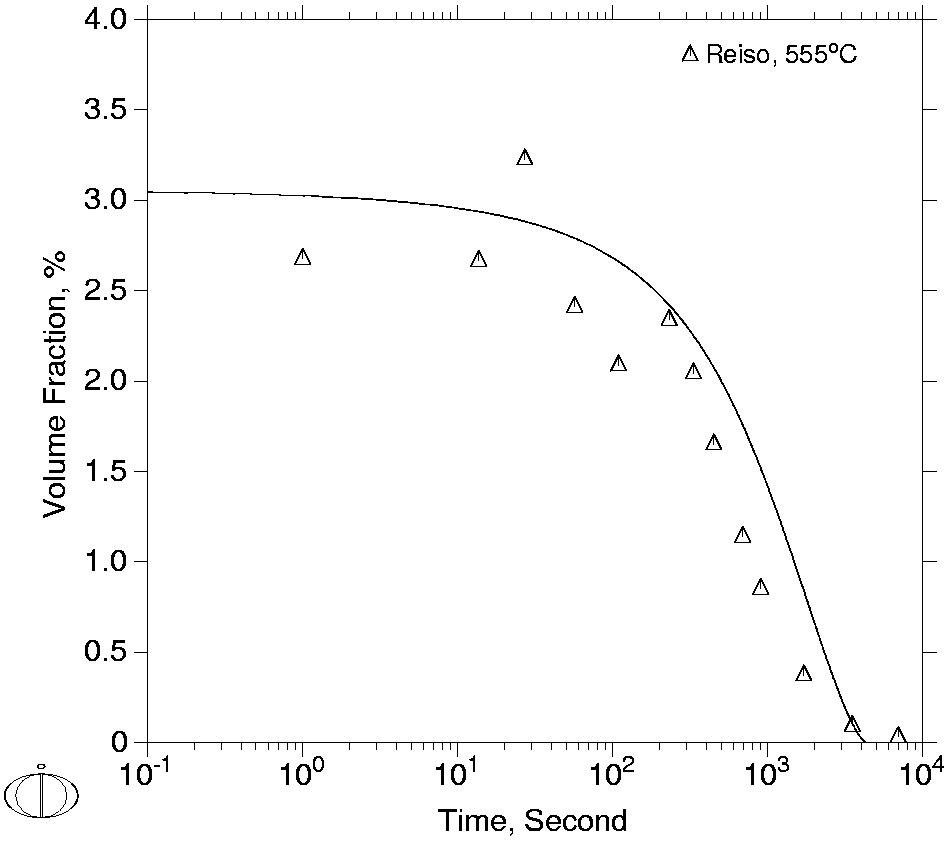

Figure 6.19. Simulated volume fraction of liquid as a function of time during constitutional liquation at 555°C with corrected experimental data in comparison with the experimental data from Reiso *et al.* [93].

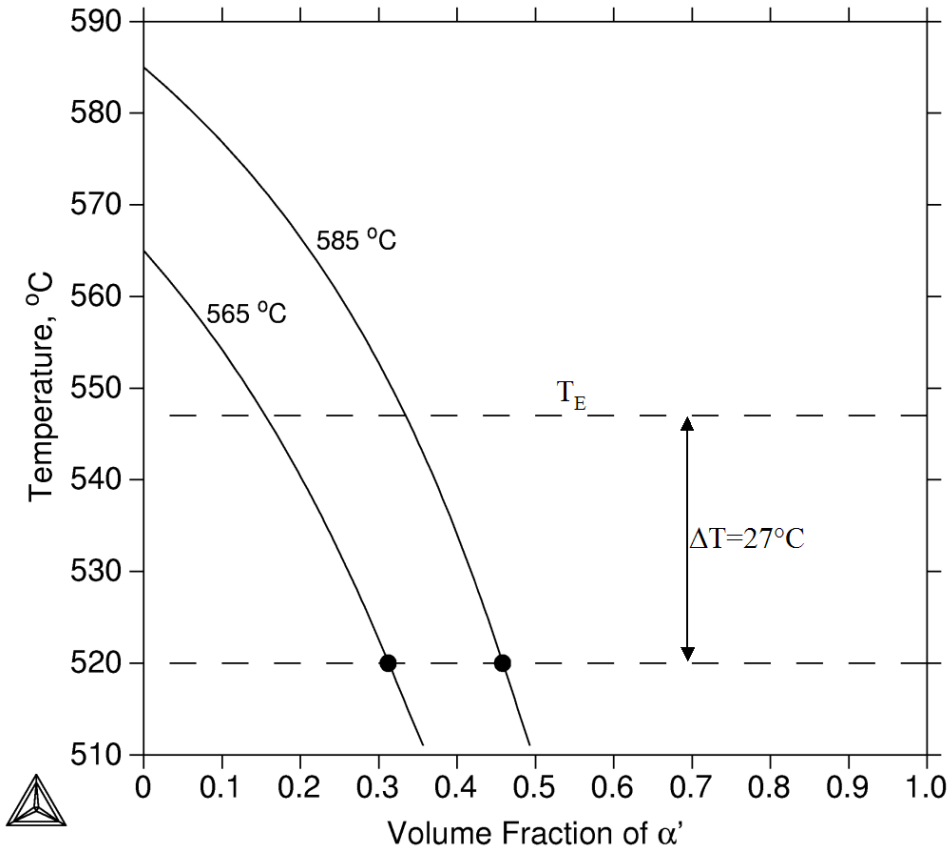

Figure 6.20. Scheil simulations of solidification of liquid from 565°C and 585°C, respectively, without formation of the θ phase.

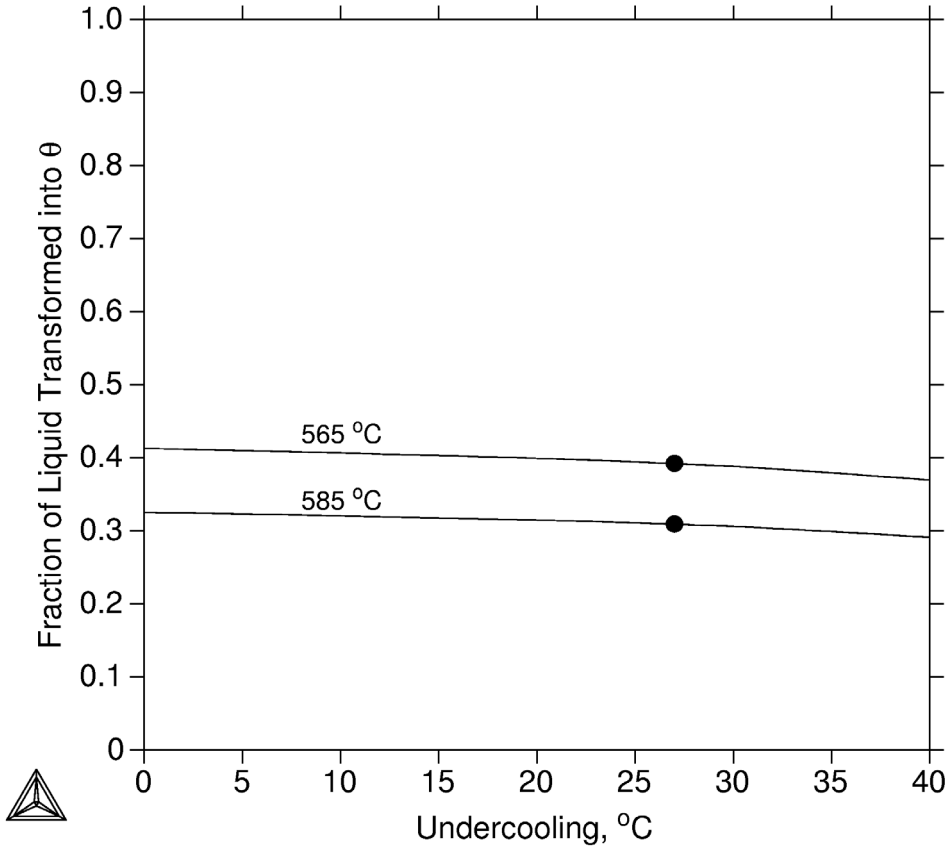

Figure 6.21. Calculated fraction of liquid transformed into θ with respect to undercooling.

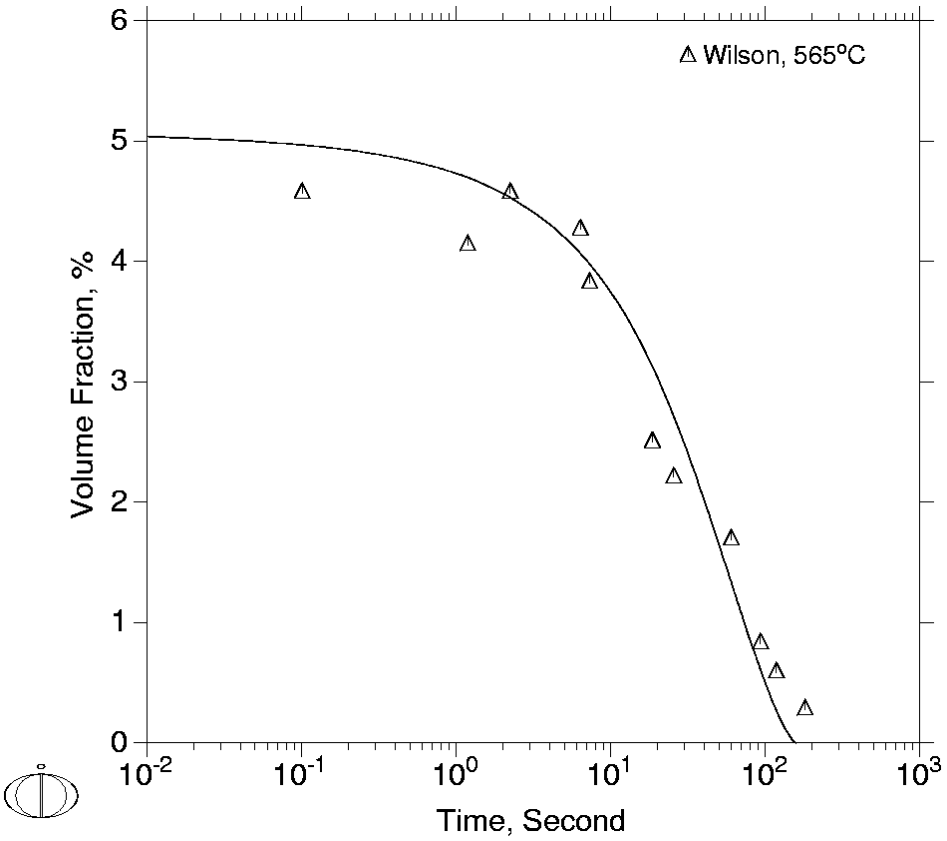

Figure 6.22. Simulated volume fraction of liquid as a function of time during constitutional liquation at 565°C with corrected experimental data in comparison with the experimental data from Wilson [94].

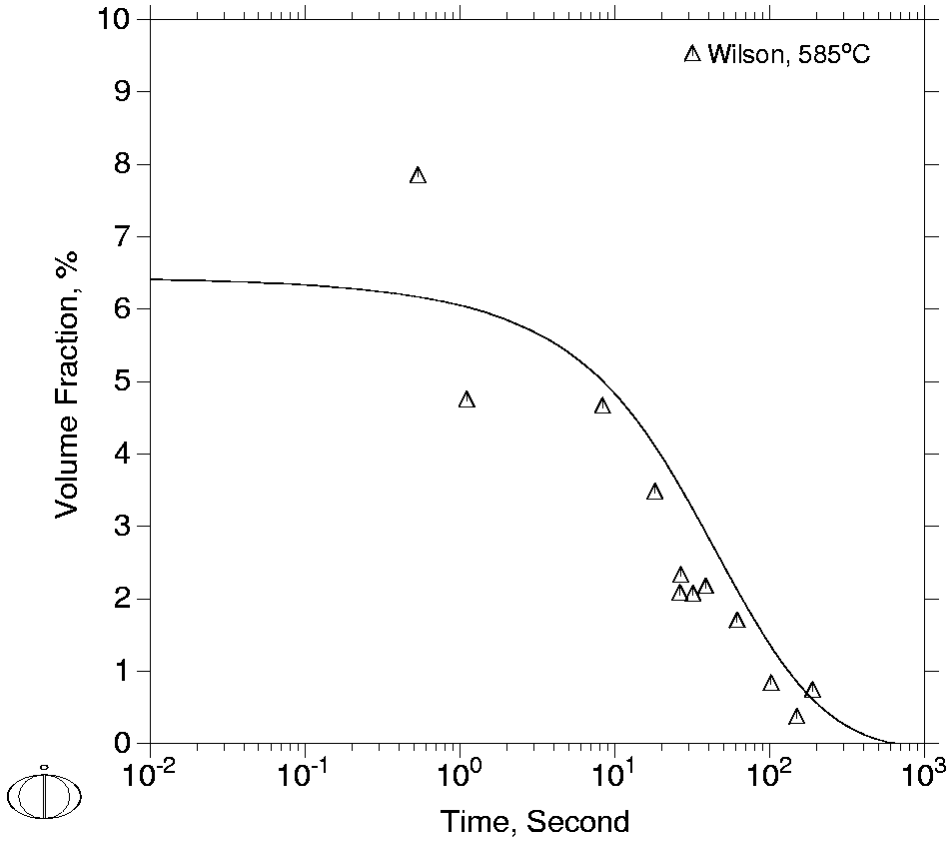

Figure 6.23. Simulated volume fraction of liquid as a function of time during constitutional liquation at 585°C with corrected experimental data in comparison with the experimental data from Wilson [94].

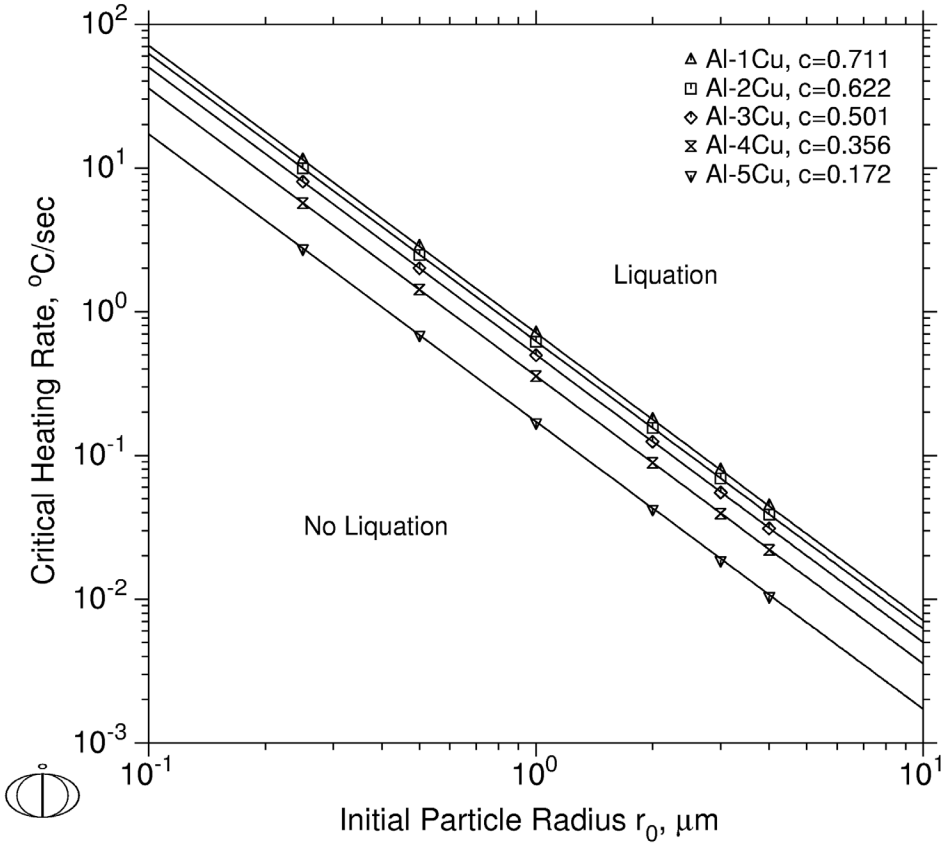

Figure 6.24. Simulated results showing the susceptibility of a series of Al-Cu alloys to constitutional liquation as a function of heating rate and particle size.

Chapter 7. FIRST-PRINCIPLES STUDY OF POINT DEFECTS IN B2 NIAL

7.1. The SQS Approach

The brute-force way to treat non-stoichiometric compounds with concentrated point defects would be to construct a large supercell and randomly distribute the point defects on the host lattice. This would necessarily require very large supercells to adequately mimic the compositional disorder caused by the significant number of point defects. Since density functional methods are computationally constrained by the number of atoms that one can treat, such an approach could be computationally prohibitive. Therefore, in the present study, we adopt the Special Quasirandom Structure (SQS) approach [34, 35] to model the B2 alloys. In Chapter 3, SQS's for the simple binary bcc alloys have already been developed. In this chapter, we further develop various SQS structures for random pseudobinary $A_{1-x}B_xC$ B2 alloys. Here A and B are randomly distributed on one sublattice with the second sublattice completely occupied by C, and thus the substitutional alloy problem is simple-cubic-based [99]. Assuming that only one type of constitutional point defects is present in the maximally ordered state [100] of the non-stoichiometric alloy, as is the case for B2 NiAl, we treat the Al-rich and Ni-rich B2 NiAl as $Ni_{1-x}Va_xAl$ and $Al_{1-x}Ni_xNi$ pseudobinary alloys [8], respectively, with Va denoting constitutional vacancies. For completeness, we also considered the other two possibilities: we treat Al-rich NiAl containing antisite Al atoms as $Ni_{1-x}Al_xAl$ and Ni-rich NiAl containing Al vacancy as $Al_{1-x}Va_xNi$. However, as will be shown later, according to our calculations, those defects are indeed energetically unfavorable with respect to the

stable ones. Admittedly, the present SQS calculations only considered the temperature-independent constitutional defects. At higher temperatures, thermal defects will also be activated in addition to the constitutional ones. Nevertheless, since B2 NiAl is strongly ordered, the concentrations of thermal defects are orders of magnitude smaller than those of the constitutional defects even at high temperatures [101], and can therefore be safely neglected.

We note that the existing first-principles studies of point defects in B2 NiAl [100, 102-104] employed large supercells containing N sites and only one isolated defect. Since those studies considered the behavior of individual point defects, the Wagner-Schottky model [105] (a gas of non-interacting point defects) were often applied, which, in principle, is only applicable when the defect concentrations are small. In contrast, the present SQS approach allows first-principles calculations of binary B2 alloys containing a large concentration of point defects (or ternary substitutional alloying elements) with interactions between the defects of the same kind directly considered in the calculations. Finally, we compare our predicted formation enthalpies, equilibrium lattice parameters and elastic constants of the B2 NiAl with existing experimental data in the literature.

7.2. Generation of the SQS's

In the present study, we have generated various SQS-N structures for the random pseudobinary $A_{1-x}B_xC$ B2 alloys (with N=4 and 16 simple cubic sites per unit cell, or a total of 2N atoms per unit cell including the common C sublattice) at composition x=0.50

and 0.25, respectively. For each composition x, the procedure is the same as described in Chapter 3:

1) Using the *gensqs* code, exhaustively generate all structures based on the simple cubic lattice with N simple cubic sites per unit cell and composition x.

2) Construct the pair and multisite correlation functions $\overline{\Pi}_{k,m}$ for each structure.

3) Finally, search for the structure(s) that best match the correlation functions of random alloys over a specified set of pair and multisite figures.

Our search criterion requires that the pair correlation functions of the structure be identical to those of the random alloy up to the third-nearest neighbor (in the present notation, the simple cubic first-, second- and third-nearest neighbors are equivalent to second-, third- and fifth-nearest neighbors in the B2 structure, respectively). For x=0.5, we find that such SQS's already exist for N=4. For the purpose of convergence test, we also generate one SQS-16 structure whose pair correlation functions are identical to those of the random alloy up to the 14th-nearest neighbor. For x=0.25, however, we found that we need *at least* a SQS-16 structure to satisfy our criterion.

The lattice vectors and atomic positions of the obtained SQS-N structures in their ideal, unrelaxed forms are given in Table 7.1, all in Cartesian coordinates. The positions of all the atoms on the common C sublattice are also included. The definitions of the multisite

figures considered here are given in Table 7.2. In Table 7.3, the pair and multisite correlation functions of the SQS-*N* structures presented in Table 7.1 are compared with those of the corresponding random simple cubic alloys. We note that the SQS-*N* structures for x=0.75 can be obtained simply by switching the A and B atoms in SQS-*N* for x=0.25.

In all present calculations, unless specifically noted, we use SQS-4 and SQS-16 to represent the random $A_{1-x}B_xC$ B2 alloy at composition x=0.5 and 0.25, respectively. SQS-4 for x=0.5 is a trigonal-type 8-atom supercell with space group $R\bar{3}m$ (space group No. 166 in the International Tables of Crystallography), and SQS-16 for x=0.25 is a trigonal-type 32-atom supercell with space group $R3m$ (space group No. 160 in the International Tables of Crystallography) [45]. Their pictures are also given in Figure 7.1 in their ideal, unrelaxed forms.

7.3. First-Principles Method

First-principles calculations were performed using the Blöchl's projector augmented wave (PAW) approach [106, 107] within the generalized gradient approximation (GGA) [50], as implemented in the highly-efficient Vienna *ab initio* simulation package (VASP) [48, 49]. The *k*-point meshes for Brillouin zone sampling were constructed using the Monkhorst–Pack scheme [52] and the total number of *k*-points times the total number of atoms per unit cell was at least 10000 to ensure highly accurate calculations. A plane wave cutoff energy of 459.9 eV was used. Spin-polarized calculations were performed to

account for the ferromagnetic nature of Ni though our calculations showed B2 NiAl as non-magnetic. All calculations include scalar relativistic corrections (i.e., no spin-orbit interaction).

We obtain elastic constants using the approach proposed by Mehl *et al.* [108]. To obtain the equilibrium volume and bulk modulus $B=(C_{11}+2C_{12})/3$ of B2 NiAl, we fitted the first-principles calculated total energies as a function of volume to a Birch-Murnaghan [109] equation of state:

$$E(V) = \sum_{n=0}^{2} a_n V^{-2n/3} \tag{7.1}$$

where V is the volume of the unit cell. The equilibrium volume V_0 is obtained by letting $\frac{\partial E}{\partial V} = 0$, and the bulk modulus is calculated as:

$$B(V) = V\frac{\partial^2 E}{\partial V^2} \tag{7.2}$$

We calculate B at the theoretical equilibrium volume V_0. To obtain shear modulus $C'=(C_{11}-C_{12})/2$, we apply a homogeneous volume-conserving orthorhombic strain to the underlying B2 lattice (the distorted lattice vectors of the SQS unit cells are obtained via a matrix multiplication [108]):

$$\varepsilon(\delta) = \begin{pmatrix} \delta & 0 & 0 \\ 0 & -\delta & 0 \\ 0 & 0 & \delta^2/(1-\delta^2) \end{pmatrix} \tag{7.3}$$

with the distortion energy $\Delta E(\delta) = 2VC'\delta^2 + O(\delta^4)$, defined as $\Delta E(\delta) = E(\delta) - E(0)$, i.e. the total energy difference between the distorted and undistorted structures. It may be argued that, since our SQS's have lower-than-cubic symmetry, in principle they should not be used to calculate the cubic elastic constants. However, we found that both our SQS-4 structure for x=0.5 and SQS-16 structure for x=0.25 do strictly satisfy the condition $E(\delta) = E(-\delta)$ and also the calculated results are independent of the choice of axis. Therefore, despite their seemingly low symmetries, they are still capable of giving unique elastic shear modulus C′ (but not C_{44}). We fit the first-principles calculated distortion energies at δ=0.005, 0.01, 0.15 and 0.02 to the function:

$$\Delta E(\delta) = \sum_{m=1}^{2} b_m \delta^{2m} \tag{7.4}$$

and we obtain $C' = b_1/2V$.

To further study the effects of local atomic relaxations around point defects on formation enthalpies, we also fully relaxed all atoms into their equilibrium positions according to the quantum-mechanical Hellmann-Feynman forces using a Quasi-Newton algorithm, maintaining the overall volume and shape of the unit cell. Due to the limited computing

resources, we did not consider such effects in our elastic constant calculations, i.e. we assume that all the atoms occupy their ideal lattice positions.

Finally, we obtained the formation enthalpies of B2 NiAl as follows:

$$\Delta H(x_{Ni}) = E(Ni_{x_{Ni}} Al_{1-x_{Ni}}) - (1 - x_{Ni})E(Al) - x_{Ni}E(Ni) \tag{7.5}$$

where $E(Al)$, $E(Ni)$ and $E(Ni_{x_{Ni}} Al_{1-x_{Ni}})$ are the first-principles calculated total energies (per atom) of the constituent pure elements Al and Ni and the corresponding SQS, respectively, each relaxed to their equilibrium geometries. Here x_{Ni} is the molar composition of Ni in the alloy. In the present study, fcc Al and ferromagnetic fcc Ni were used as reference states in Eq. (7.5).

7.4. Results

7.4.1. Equilibrium Lattice Parameters

The equilibrium lattice parameters of B2 NiAl obtained from the SQS calculations are plotted in Figure 7.2 together with the experimental X-ray measurements by Bradley and Taylor [8]. The equilibrium lattice parameter of the stoichiometric B2 NiAl was obtained in the present study to be 2.89 Å. In Figure 7.2, there are four branches, each corresponding to one of the four possible types of constitutional point defects. The experimental data can be well explained by our SQS calculations if we assume that Ni

vacancies and antisite Ni atoms are the stable point defects in Al-rich and Ni-rich B2 NiAl, respectively, in accordance with Bradley and Taylor [8].

In order to consider the effects of pressure, we plot in Figure 7.3 the volume per atom of B2 NiAl as a function of composition. Here we consider a canonical ensemble containing a total one mole of Al and Ni atoms and the total number of lattice sites may thus vary when vacancies are present. We observe that constitutional vacancies do always increase the system volume and as a consequence, increasing pressure will always suppress the formation of constitutional vacancies. On the Ni-rich side, increasing pressure will only further increase the stability of antisite Ni atoms. Whereas on the Al-rich side, theoretically, at certain crossover pressure, constitutional vacancies will become unstable with respect to antisite Al atoms, i.e. a reversal of the stable point defects will occur [100, 104].

7.4.2. Formation Enthalpies

In Figure 7.4, the predicted formation enthalpies of B2 NiAl are compared with the experimental measurements by Nash and Kleppa [110] at 298K. The formation enthalpy of the stoichiometric B2 NiAl was obtained in the present study to be -64.2 kJ/mol. We consider a canonical ensemble containing a total one mole of Al and Ni atoms. Again, there are four branches in Figure 7.4, each corresponding to one of the four types of constitutional point defects. The solid and dashed lines correspond to unrelaxed (volume relaxation only) and relaxed (volume + local atomic relaxations) formation enthalpies,

respectively. Our SQS calculations unambiguously show that, at T=0K and zero pressure, Ni vacancies and antisite Ni atoms are indeed the energetically favorable point defects in Al-rich and Ni-rich B2 NiAl, respectively. We also observe that, for the two stable branches, i.e. Ni vacancies and antisite Ni atoms, the effects of local atomic relaxations on formation enthalpies are rather small. We thus believe that their effects on the elastic properties, which are determined by the two stable branches, will also be small.

For each branch, we fitted our SQS calculated formation enthalpies to a quadratic function of alloy composition in the form:

$$\Delta H(\chi) = \Delta H_{NiAl} + c_1\chi + c_2\chi^2 \tag{7.6}$$

where $\chi = |x_{Ni} - 0.5|$ is the absolute deviation from stoichiometry and ΔH_{NiAl} is the formation enthalpy of the stoichiometric B2 NiAl. The coefficients c_1 represents the linear part of the composition dependence of the alloy formation enthalpy, and is directly related to the defect formation enthalpies H_d in stoichiometric B2 NiAl used in the Wagner-Schottky model [105]:

$$\Delta H = \Delta H_{NiAl} + \sum_d H_d x_d \tag{7.7}$$

where defect type d=Va_{Ni}, Al_{Ni}, Va_{Al} and Ni_{Al} , with the subscript denoting sublattice. x_d is the atomic concentration defined as the total number of defects of type d divided by the

total number of atoms. Since $x_d = \chi$ for antisite atoms and $x_d = 2\chi$ and for constitutional vacancies, we get $H_d = c_1$ for antisite atoms and $H_d = c_1/2$ for constitutional vacancies.

In principle, Eq. (7.7) is only applicable when the defect concentrations are small. At high defects concentrations, departure from the Wagner-Schottky model may occur due to the interaction between the defects, as indicated by the nonlinear term c_2 in Eq. (7.6). We note that, our SQS calculations directly considered the interactions between defects of the *same* type. It also needs to be mentioned that, since the defect formation enthalpy H_d is dependent on the choice the reference state of pure elements, it is not meaningful to consider their absolute values. Rather, the formation enthalpies of the thermal defects are independent of the choice of reference states and are thus free of such ambiguities. Since single point defects in ordered alloys alone are not composition-conserving, those thermal defects appear in balanced combinations, e.g. two Ni vacancies and one antisite Ni atom (triple defect), in order to maintain the composition of the alloy. As noted by Mishin *et al* [11], the point defects are grouped into composition-conserving defect complexes only conceptually, not physically. Assuming that those thermal defects are completely dissociated, their formation enthalpies can be calculate using only the formation enthalpies of the individual constituent point defects. In Table 7.4, we compare our results with those from the existing first-principles supercell studies in the literature [100, 102, 103]. Our predicted triple defect formation energy is in good agreement with experiments [111, 112], especially when local atomic relaxations are considered.

7.4.3. Convergence Tests

In Table 7.5, we further investigate the effects of SQS supercell size on our calculated formation enthalpies. Remarkably, our 8-atom SQS-4 structures predicted well within 1.4kJ/mol all the results obtained using 32-atom SQS-16 structures, even when local atomic relaxations are taken into account. Similar rapid convergence behavior of the SQS's were also observed by Zunger *et al.* [34, 35] and our study in Chapter 3 of this thesis.

7.4.4. Elastic Constants Calculations

Figure 7.5 shows our calculated distortion energies as a function of δ^2 for various B2 NiAl alloys. The slopes of the curves at $\delta^2=0$ correspond to the C′ elastic constants (for a truly harmonic crystal, the distortion energies should all fall on a straight line). Figure 7.6 shows our predicted bulk modulus *B* and shear modulus C′ of B2 NiAl in excellent agreements with the room temperature experimental measurements by Rusovic and Warlimont [113] and Davenport *et al.* [114]. Remarkably, we predict that, even though antisite Ni atoms increase the bulk modulus, they rapidly soften shear modulus C′. In other words, excess Ni atoms entering into NiAl rapidly decrease its structural stability. Beyond a critical concentration of $x_{Ni}^{*} \sim 0.68$, C′ becomes negative, i.e. B2 NiAl is mechanically unstable (for a cubic structure to be mechanically stable, all three cubic elastic constants, i.e. *B*, C′ and C_{44}, must be positive). At high temperatures, the single-phase region of B2 NiAl actually extends around 2% beyond this mechanical stability

limit [115], presumably due to the entropy stabilization effect. The rapidly decreasing C′ with the Ni concentration explains well the experimentally observed [116] rapid increase of martensitic transformation temperature of B2 NiAl with Ni concentration (124K per at. % Ni): lower value of C′ indicates weaker resistance of the lattice to $\{110\}<1\bar{1}0>$ shear and thus higher transformation temperature. It is also worth noting that, at the stoichiometric composition, C′ is very positive. As the result, martensitic transformation only occurs in B2 NiAl with high Ni concentrations.

7.5. Summary

In this chapter, we further extend the first-principles SQS methodology to more complex phases with multiple sublattices. We present three Special Quasirandom Structures (SQS's) for substitutionally random pseudobinary $A_{1-x}B_xC$ B2 alloys at compositions x=0.25, 0.5 and 0.75, respectively. The structures possess local pair and multisite correlation functions that mimic those of the corresponding random alloys. The development of these SQS's allows, for the first time, first-principles calculations of binary B2 alloys containing large concentration of constitutional point defects (or ternary substitutional alloying elements). We demonstrate the usefulness of our SQS's by applying them to studying the constitutional point defects in non-stoichiometric B2 NiAl. Our first-principles SQS results provide formation enthalpies, equilibrium lattice parameters and elastic constants of B2 NiAl which agree satisfactorily with the existing experimental data in the literature. Our results unambiguously show that, at T=0K and zero pressure, Ni vacancies and antisite Ni atoms are the energetically favorable point

defects in Al-rich and Ni-rich B2 NiAl, respectively. We also predicted a structural instability of B2 NiAl caused by antisite Ni atoms which explains well the martensitic transformation observed in this compound at high Ni concentrations. Since the present approach is rather general, it can be straightforwardly extended to study other B2 aluminides.

Table 7.1. Structural descriptions of the SQS-*N* structures. Lattice vectors and atomic positions are given in Cartesian coordinates, in units of *a*, the B2 lattice parameter. Atomic positions are given for the ideal, unrelaxed B2 sites.

	$A_{0.5}B_{0.5}C$	$A_{0.75}B_{0.25}C$
SQS-16	Lattice vectors $\vec{a}_1$ =(1.0, 2.0, 1.0), $\vec{a}_2$ =(1.0, 0.0, -1.0) $\vec{a}_3$ =(-3.0, 2.0, -3.0) Atomic positions A - (-1.5, 2.5, -2.5), A - (-1.5, 1.5, -2.5) A - (0.5, 1.5, -1.5), A - (-0.5, 1.5, -2.5) A - (-1.5, 2.5, -3.5), A - (-1.5, 3.5, -2.5) A - (0.5, 0.5, -1.5), A - (0.5, 0.5, -0.5) B - (-0.5, 1.5, -1.5), B - (-0.5, 2.5, -2.5) B - (-0.5, 2.5, -1.5), B - (-0.5, 3.5, -2.5) B - (0.5, 1.5, -0.5), B - (0.5, 2.5, -1.5) B - (0.5, 2.5, -0.5), B - (1.5, 1.5, -0.5) C - (-2.0, 2.0, -3.0), C - (0.0, 3.0, -1.0) C - (-1.0, 2.0, -3.0), C - (-1.0, 2.0, -2.0) C - (-1.0, 3.0, -3.0), C - (-1.0, 3.0, -2.0) C - (0.0, 1.0, -2.0), C - (0.0, 1.0, -1.0) C - (0.0, 2.0, -2.0), C - (0.0, 2.0, -1.0) C - (0.0, 3.0, -2.0), C - (-1.0, 4.0, -3.0) C - (1.0, 1.0, -1.0), C - (1.0, 2.0, -1.0) C - (1.0, 2.0, 0.0), C - (-2.0, 3.0, -3.0)	Lattice vectors $\vec{a}_1$ =(3.0, 1.0, 1.0), $\vec{a}_2$ =(-1.0, -3.0, 1.0) $\vec{a}_3$ =(-1.0, 1.0, -3.0) Atomic positions A - (1.5, -1.5, 0.5), A - (2.5, 0.5, 0.5) A - (0.5, -0.5, -0.5), A - (1.5, 0.5, -0.5) A - (-0.5, 0.5, -2.5), A - (1.5, -0.5, 0.5) A - (1.5, -0.5, -0.5), A - (-0.5, -1.5, -1.5) A - (0.5, -0.5, -1.5), A - (-0.5, -0.5, -1.5) A - (0.5, 0.5, -1.5), A - (0.5, -1.5, -0.5) B - (-0.5, -1.5, -0.5), B - (-0.5, -2.5, 0.5) B - (0.5, -1.5, 0.5), B - (1.5, 0.5, -1.5) C - (2.0, 1.0, -1.0), C - (-1.0, -2.0, -1.0) C - (2.0, 0.0, 0.0), C - (0.0, -1.0, -1.0) C - (0.0, 0.0, -1.0), C - (1.0, 0.0, -1.0) C - (0.0, -2.0, 0.0), C - (2.0, -1.0, 1.0) C - (0.0, -1.0, 0.0), C - (1.0, -1.0, 0.0) C - (1.0, -1.0, -1.0), C - (1.0, 0.0, 0.0) C - (1.0, -2.0, 1.0), C - (-1.0, -1.0, -2.0) C - (0.0, 0.0, -2.0), C - (1.0, 1.0, -2.0)
SQS-4	Lattice vectors $\vec{a}_1$ =(2.0, 1.0, 1.0), $\vec{a}_2$ =(1.0, 1.0, 2.0) $\vec{a}_3$ =(1.0, 2.0, 1.0) Atomic positions A - (0.5, 0.5, 0.5), A - (3.5, 3.5, 3.5) B - (1.5, 1.5, 1.5), B - (2.5, 2.5, 2.5) C - (0.0, 0.0, 0.0), C - (1.0, 1.0, 1.0) C - (2.0, 2.0, 2.0), C - (3.0, 3.0, 3.0)	

Table 7.2. Vertices of the multisite figures, given in units of *a*, the B2 lattice parameter.

Type	Figure designation	Vertices			
Triplets	(3,2)	(0, 0, 0)	(0, 0, 1)	(0, 1, 1)	
Quadruplets	(4,2)	(0, 0, 0)	(1, 1, 0)	(1, 0, 1)	(0, 1, 1)

Table 7.3. Pair and multisite correlation functions of SQS-*N* structures. The number in the square brackets next to $\overline{\Pi}_{k,m}$ gives the degeneracy factor of the corresponding figure.

Figure	x=0.5			x=0.25	
	Random	SQS-16	SQS-4	Random	SQS-16
$\overline{\Pi}_{2,1}$ [3]	0	0	0	0.25	0.25
$\overline{\Pi}_{2,2}$ [6]	0	0	0	0.25	0.25
$\overline{\Pi}_{2,3}$ [4]	0	0	0	0.25	0.25
$\overline{\Pi}_{2,4}$ [3]	0	0	-1	0.25	0
$\overline{\Pi}_{2,5}$ [12]	0	0	0	0.25	0.25
$\overline{\Pi}_{2,6}$ [12]	0	0	0	0.25	0.25
$\overline{\Pi}_{2,7}$ [6]	0	0	1	0.25	0
$\overline{\Pi}_{3,2}$ [12]	0	0	0	-0.125	-0.125
$\overline{\Pi}_{4,2}$ [2]	0	0	-1	0.0625	0

Table 7.4. Formation enthalpies (eV/defect) of isolated point defects and complex composition-conserving defects in stoichiometric B2 NiAl. Reference states: fcc Al and fcc Ni.

Defect type	Designation	Present study		Experiment	[100] (GGA)	[102] (LDA)	[103] (LDA)
		unrelaxed	relaxed				
Ni vacancy	Va_{Ni}	0.44	0.29		0.62		
Antisite Al	Al_{Ni}	2.56	1.90		2.51		
Al vacancy	Va_{Al}	1.88	1.83		1.91		
Antisite Ni	Ni_{Al}	1.09	0.99		1.13		
Triple Ni	$0 \rightarrow 2Va_{Ni} + Ni_{Al}$	1.97	1.57	1.64-1.83 [111] 1.28 [112]	2.36	2.83	2.22
Divacancy	$0 \rightarrow Va_{Ni} + Va_{Al}$	2.32	2.12		2.53	3.07	2.71
Exchange	$0 \rightarrow Al_{Ni} + Ni_{Al}$	3.65	2.89		3.63	3.15	3.10
Triple Al	$0 \rightarrow 2Va_{Al} + Al_{Ni}$	6.32	5.56		6.32	6.46	6.30

Table 7.5. Effects of SQS supercell size on formation enthalpies (kJ/mol).

Alloy	SQS-4		SQS-16		Difference	
	Unrelaxed	Relaxed	Unrelaxed	Relaxed	Unrelaxed	Relaxed
$Ni_{0.5}Va_{0.5}Al$	-42.0	-43.1	-40.6	-42.2	1.4	0.9
$Al_{0.5}Ni_{0.5}Ni$	-32.9	-33.9	-32.5	-33.1	0.4	0.8
$Al_{0.5}Va_{0.5}Ni$	-3.7	-8.0	-2.6	-9.2	1.1	1.2
$Ni_{0.5}Al_{0.5}Al$	-10.9	-18.5	-11.2	-19.8	0.3	1.3

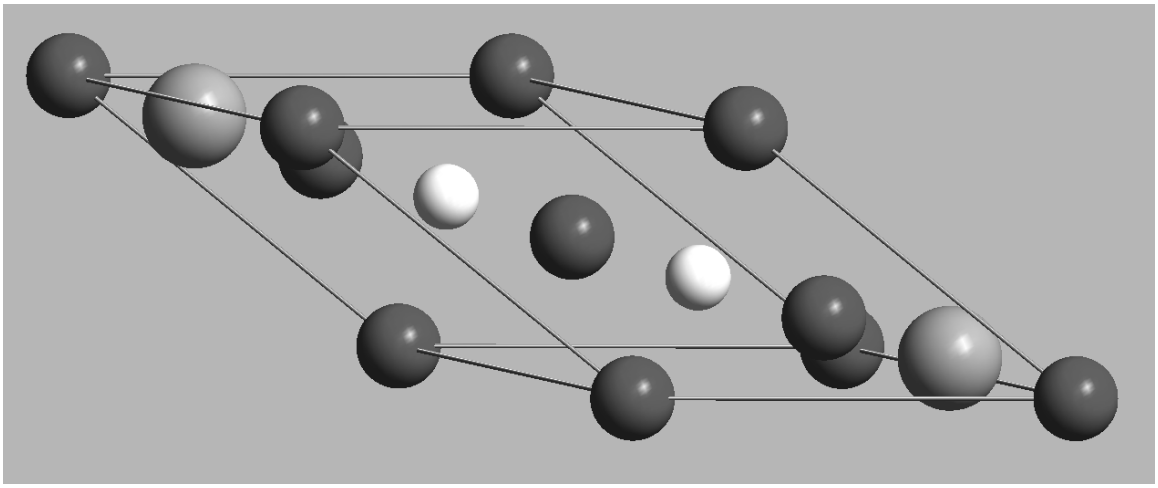

(a) SQS-4 for $A_{0.5}B_{0.5}C$

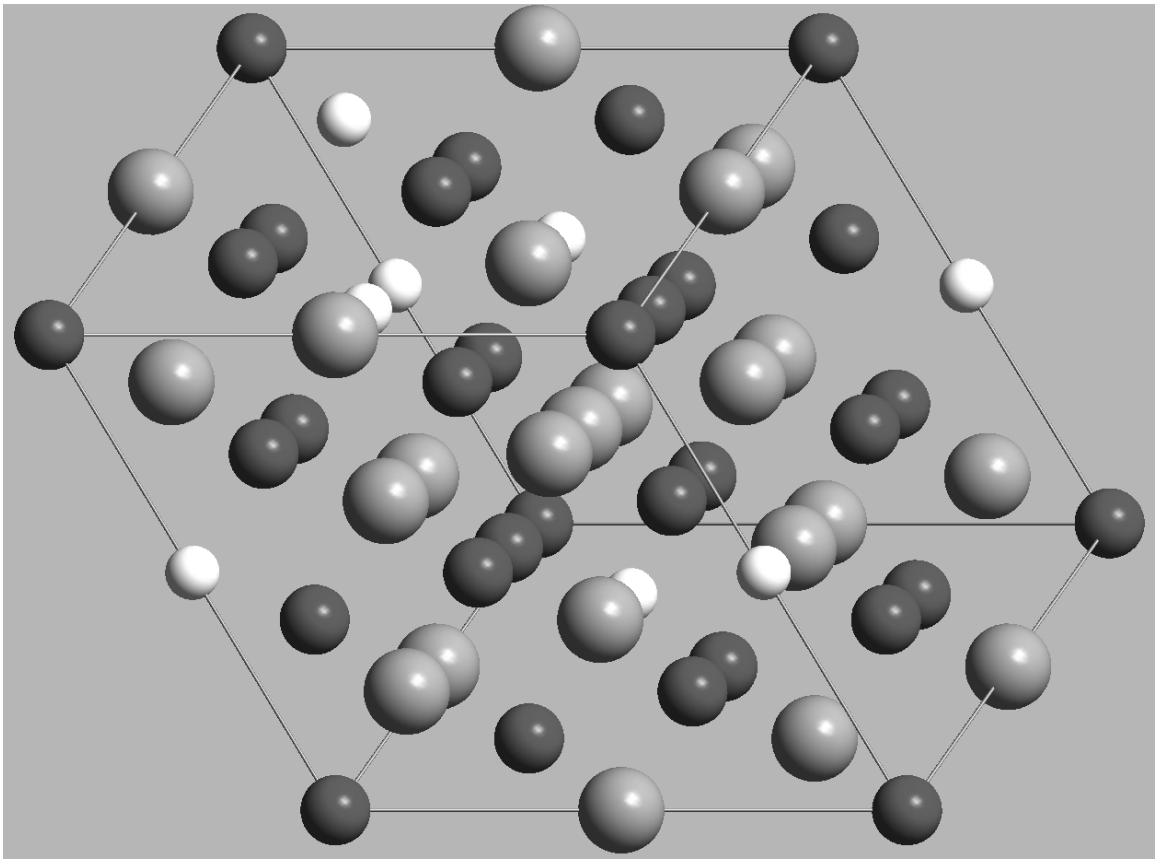

(b) SQS-16 for $A_{0.75}B_{0.25}C$

Figure 7.1. Crystal structure of SQS's in their ideal, unrelaxed forms. Gray, white and dark spheres represent A, B and C atoms, respectively.

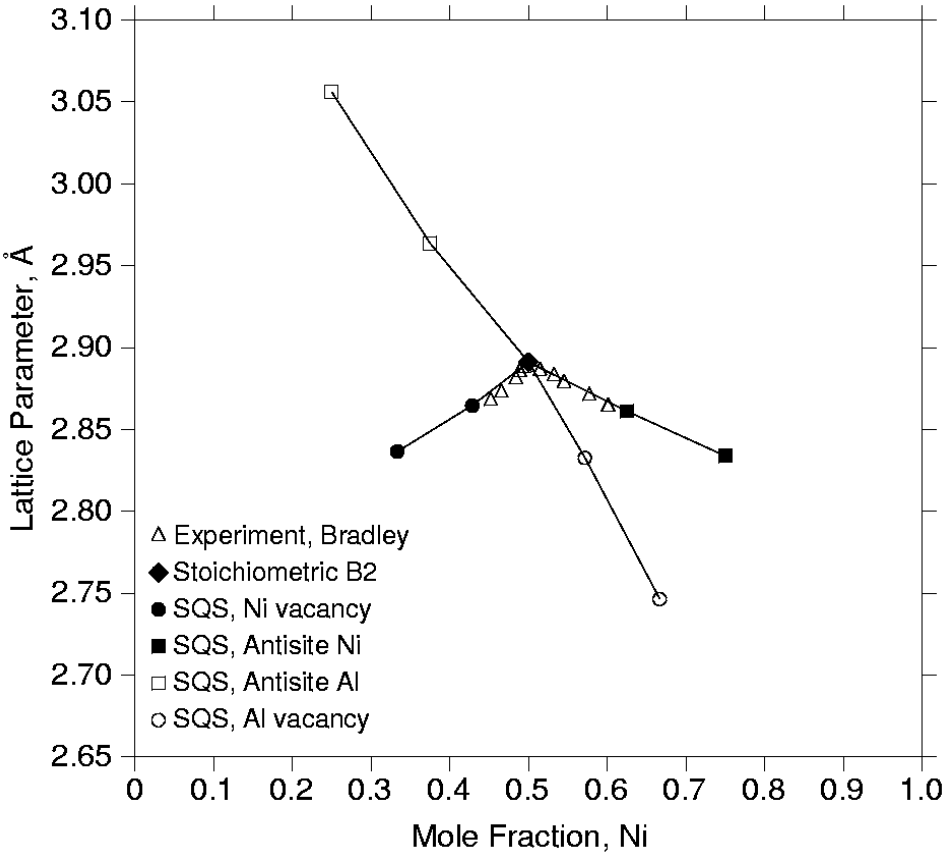

Figure 7.2. Comparison between first-principles calculated and experimentally observed equilibrium lattice parameters of B2 NiAl. Experimental data come from Bradley and Taylor [8].

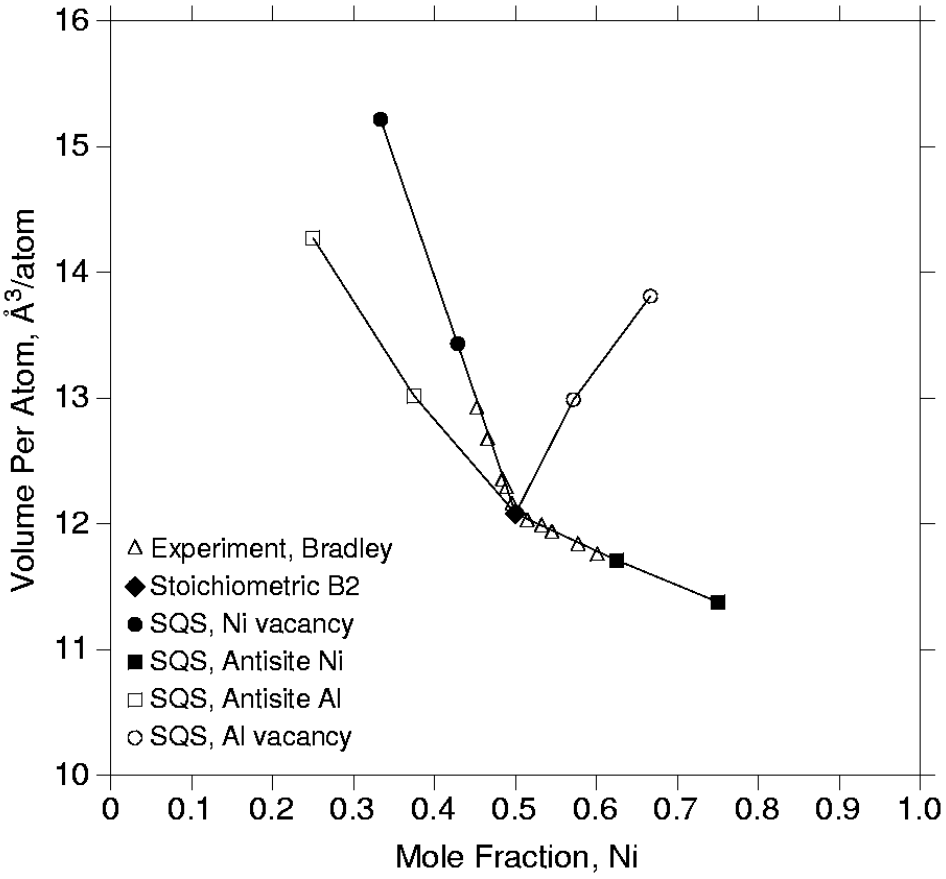

Figure 7.3. Comparison between first-principles calculated and experimentally observed equilibrium volume per atom of B2 NiAl. Experimental data come from Bradley and Taylor [8].

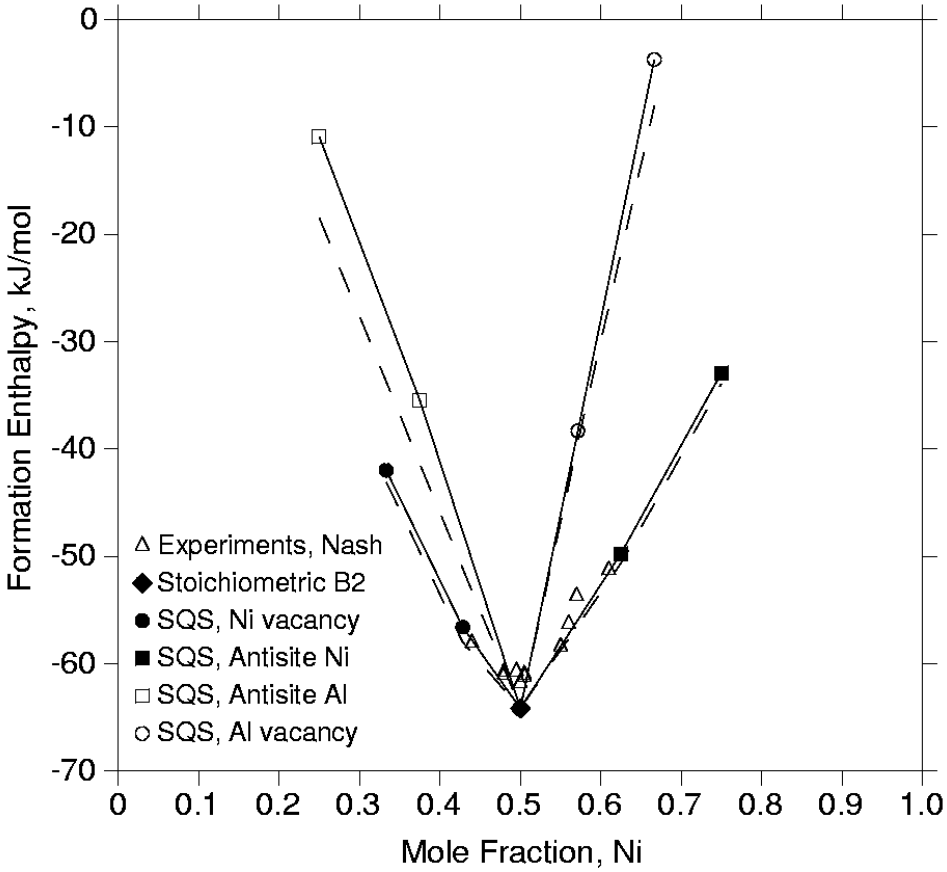

Figure 7.4. Comparison between first-principles calculated and experimentally observed formation enthalpies of B2 NiAl. Experimental data come from Nash and Kleppa [110].

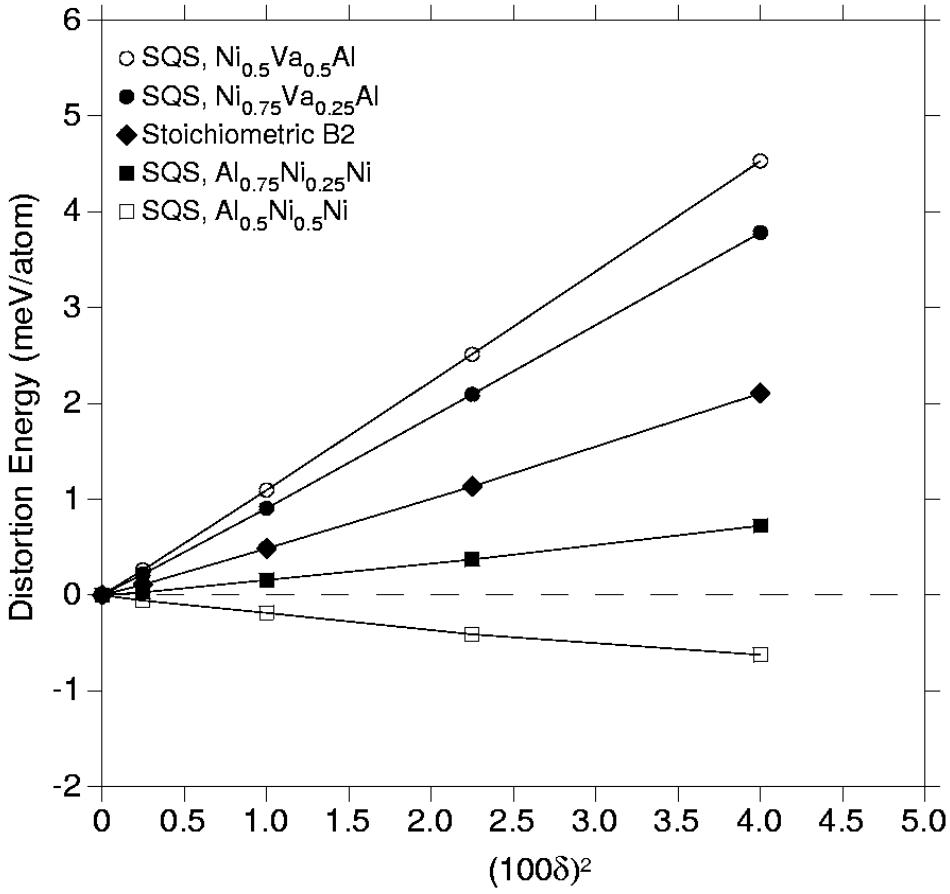

Figure 7.5. Distortion energies of various B2 NiAl alloys under a homogeneous volume-conserving orthorhombic strain.

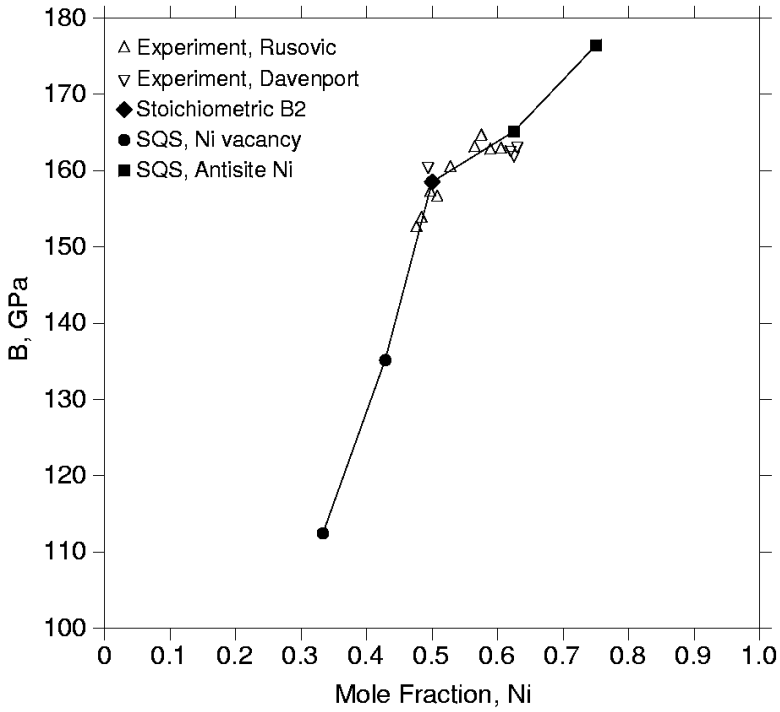

(a) bulk modulus *B*

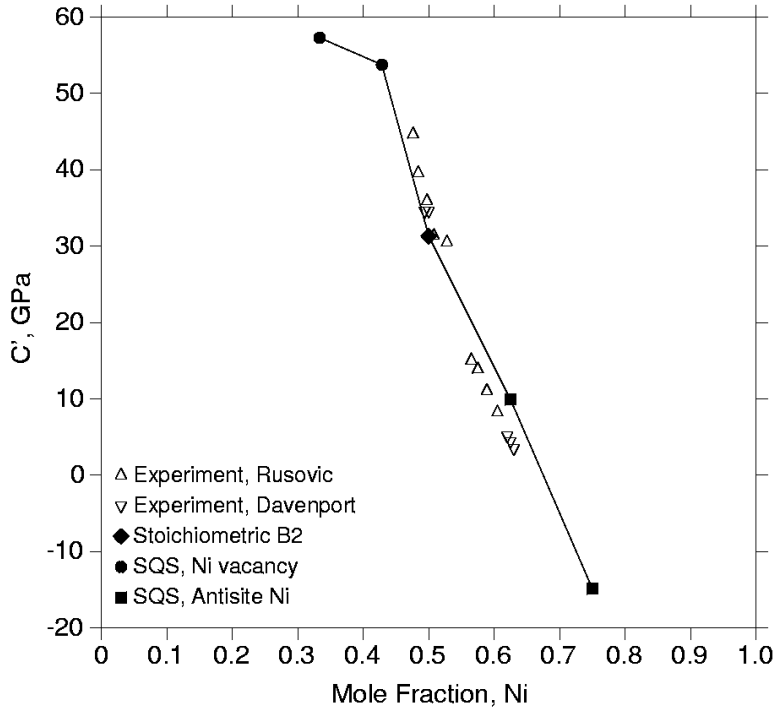

(b) shear modulus C′

Figure 7.6. Comparison between first-principles calculated and experimentally observed (a) bulk modulus *B* and (b) shear modulus C′ of B2 NiAl. Experimental data come from Rusovic and Warlimont [113] and Davenport *et al.* [114].

Chapter 8. CONCLUSIONS AND FUTURE WORKS

8.1. Conclusions

The major accomplishments achieved in the present Ph.D. study can be summarized as follows:

1) Special Quasirandom Structures (SQS's) for random binary bcc alloys have been developed. Those structures allow for the possibility of first-principles calculations of bcc alloys, even those with significant size-mismatch.

2) SQS's for pseudobinary B2 alloys are developed. Those structures allow for the first time direct first-principles calculations of binary B2 alloys containing large concentration of constitutional point defects (or ternary substitutional alloying elements). Remarkably, using the SQS's, it is predicted that high defect concentrations can lead to structural instability of B2 NiAl, which explains well the martensitic transformation observed in this compound at high Ni concentrations.

3) Using the combined CALPHAD and first-principles approach, a self-consistent thermodynamic description of the Al-Cu system including the metastable θ′ and θ″ phases is obtained.

4) The CALPHAD approach has been successfully applied to study the constitutional liquation in the model Al-Cu system. The critical heating rate for avoiding liquation has been obtained through computer simulations. The computational procedures developed in the present study is rather general and can be readily extended to predict the susceptibility of commercial multi-component aluminum alloys to constitutional liquation during welding.

8.2. Future Works

1) Simulating the complete $\theta'' \rightarrow \theta' \rightarrow \theta$ aging process using the Gibbs energies of the metastable phases obtained in the present study will be very useful as such simulations will allow us to predict the final microstructure of the Al-Cu alloy as a function of aging time and temperature.

2) The usefulness of the SQS's approach is highlighted in the present research. It is thus very interesting to further develop SQS's for other structures.

3) It will be straightforward to apply the present B2 SQS's to study other B2 aluminides, e.g. FeAl. Also, it will be interesting to put the SQS energetics in a mean-field sublattice model, which allows us to calculate the point defect concentrations at high temperatures, and thus to study the thermal defects.

APPENDIX A. 16-ATOM SQS'S FOR RANDOM FCC ALLOYS [43]

$A_{0.5}B_{0.5}$	$A_{0.75}B_{0.25}$
Lattice vectors	Lattice vectors
$\vec{a}_1$ =(1.0, 0.5, 0.5)	$\vec{a}_1$ =(1.0, 0.5, 0.5)
$\vec{a}_2$ =(0.0, 1.0, -1.0)	$\vec{a}_2$ =(-0.5, 1.5, 0.0)
$\vec{a}_3$ =(-1.0, 1.5, 1.5)	$\vec{a}_3$ =(-0.5, -0.5, 2.0)
Atomic positions	Atomic positions
A – (0.5, 0.5, 0.0)	A - (0.0, 0.0, 2.0)
A - (0.0, 0.5, 0.5)	A - (-0.5, 0.0, 1.5)
A - (0.0, 1.0, 1.0)	A – (0.0, 0.5, 1.5)
A - (0.0, 1.5, 0.5)	A - (-0.5, 0.5, 1.0)
A - (-0.5, 1.5, 0.0)	A - (0.0, 1.5, 0.5)
A - (-0.5, 1.5, 1.0)	A - (0.5, 1.0, 0.5)
A – (0.0, 2.0, 1.0)	A - (-0.5, 0.5, 2.0)
A - (-0.5, 2.0, 0.5)	A - (0.0, 1.0, 2.0)
B - (0.0, 0.0, 0.0)	A - (-0.5, 1.0, 1.5)
B - (0.0, 0.5,-0.5)	A - (0.0, 1.5, 1.5)
B - (0.5, 1.0,-0.5)	A - (0.0, 0.0, 1.0)
B - (0.5, 1.0, 0.5)	A - (0.5, 0.5, 1.0)
B - (0.0, 1.0, 0.0)	B - (0.0, 0.0, 0.0)
B - (0.5, 1.5, 0.0)	B - (0.0, 1.0, 1.0)
B - (-0.5, 1.0, 0.5)	B – (-0.5, 1.0, 0.5)
B - (0.0, 1.5, 1.5)	B - (0.0, 0.5, 0.5)

All lattice vectors and atomic positions are given in Cartesian coordinates, in units of *a*, the fcc lattice constant. Atomic positions are given for the ideal, unrelaxed fcc sites. SQS-16 for $A_{0.5}B_{0.5}$ reproduces the pair correlation functions of perfectly random fcc alloys accurately up to the seventh-nearest neighbor while SQS-16 for $A_{0.75}B_{0.25}$ reproduces the pair correlation functions of perfectly random fcc alloys accurately up to the third-nearest neighbor. SQS for $A_{0.25}B_{0.75}$ can be simply obtained by switching the A and B atoms in SQS for $A_{0.75}B_{0.25}$.

APPENDIX B. THERMO-CALC INPUT FILE FOR AL-CU SYSTEM

```
DEF-COMPONENT AL CU
ENTER_SYMBOL CONSTANT DX=0.01,DT=10,P0=101325,R=8.314,DH=1000

$ ENTHALPY OF MIXING OF LIQUID [Stolz 1993]
$ REFERENCE STATE: LIQUID AL AND SUPERCOOLED LIQUID CU
TABLE_HEAD 100
CREATE_NEW_EQUILIBRIUM @@,1
CHANGE_STATUS PHASE LIQUID=FIX 1
SET-CONDITION P=P0,T=1467,X(LIQUID,CU)=@1
SET_REFERENCE_STATE AL LIQUID * 1E5
SET_REFERENCE_STATE CU LIQUID * 1E5
EXPERIMENT HMR(LIQUID)=@2:DH
LABEL AHL
SET-ALL-START Y
TABLE_VALUES
$ X(CU)   HMIX[J/MOL]
$ T=1467K
 0.052     -1.7E3
 0.10     -3.32E3
 0.15     -5.04E3
 0.198     -6.84E3
 0.248     -8.55E3
 0.299     -10.3E3
 0.348     -11.8E3
 0.400     -13.5E3
 0.451     -14.9E3
 0.50     -16.1E3
 0.549     -17.1E3
 0.598     -17.7E3
 0.63     -17.9E3
 0.66     -17.6E3
 0.69     -17.1E3
 0.711     -16.5E3
 0.731     -15.7E3
 0.751     -14.7E3
 0.769     -13.9E3
 0.785     -12.8E3
 0.801     -11.8E3
TABLE_END

$ ENTHALPY OF MIXING OF LIQUID [Witusiewicz 1998]
$ REFERENCE STATE: LIQUID AL AND SUPERCOOLED LIQUID CU
TABLE_HEAD 200
CREATE_NEW_EQUILIBRIUM @@,1
CHANGE_STATUS PHASE LIQUID=FIX 1
SET-CONDITION P=P0,T=1450,X(LIQUID,AL)=@1
SET_REFERENCE_STATE AL LIQUID * 1E5
SET_REFERENCE_STATE CU LIQUID * 1E5
EXPERIMENT HMR(LIQUID)=@2:DH
LABEL AHL
SET-ALL-START Y
TABLE_VALUES
```

```
$ X(AL)   HMIX[J/MOL]
$ T=1450K
 0.098     -6.7E3
 0.201     -13.1E3
 0.141     -9.1E3
 0.247     -14.8E3
 0.331     -17.6E3
 0.399     -18.6E3
TABLE_END

TABLE_HEAD 300
CREATE_NEW_EQUILIBRIUM @@,1
CHANGE_STATUS PHASE LIQUID=FIX 1
SET-CONDITION P=P0,T=1073,X(LIQUID,CU)=@1
SET_REFERENCE_STATE AL LIQUID * 1E5
SET_REFERENCE_STATE CU LIQUID * 1E5
EXPERIMENT ACR(AL)=@2:0.05
LABEL AAL
SET-ALL-START Y
TABLE_VALUES
$42GRU
$ T=1073K
0.148487 0.800817
0.316242 0.590531
0.367015 0.451136
0.406861 0.379292
0.427482 0.350254
0.486614 0.279682
TABLE_END

TABLE_HEAD 400
CREATE_NEW_EQUILIBRIUM @@,1
CHANGE_STATUS PHASE LIQUID=FIX 1
SET-CONDITION P=P0,T=1373,X(LIQUID,CU)=@1
SET_REFERENCE_STATE AL LIQUID * 1E5
SET_REFERENCE_STATE CU LIQUID * 1E5
EXPERIMENT ACR(CU)=@2:0.05
LABEL AAL
SET-ALL-START Y
TABLE_VALUES
$73HUL
$ T=1373K
0.903943 0.839302
0.803858 0.599744
0.701031 0.353263
0.599501 0.164876
0.497822 0.0843719
0.400216 0.04399
0.301207 0.0229677
0.202185 0.0116274
0.10316 0.00305318
$72BAT
0.903973 0.817172
0.803975 0.513991
0.699788 0.256441
0.599589 0.0998693
```

```
0.49923 0.0608628
0.400233 0.0315419
0.301215 0.0174353
0.202191 0.00747801
0.103162 0.00167007
TABLE_END

TABLE_HEAD 500
CREATE_NEW_EQUILIBRIUM @@,1
CHANGE_STATUS PHASE LIQUID=FIX 1
SET-CONDITION P=P0,T=1373,X(LIQUID,CU)=@1
SET_REFERENCE_STATE AL LIQUID * 1E5
SET_REFERENCE_STATE CU LIQUID * 1E5
EXPERIMENT ACR(AL)=@2:0.05
LABEL AAL
SET-ALL-START Y
TABLE_VALUES
$85WIL
$ T=1373K
0.179114 0.788877
0.25216 0.683963
0.327961 0.57629
0.372098 0.487893
0.425874 0.392608
0.468626 0.311123
0.508605 0.246227
0.543069 0.190998
0.620241 0.0860956
0.658808 0.0474755
0.751021 0.0090046
0.85282 0.000989033
0.951857 0.00126451
0.57339 0.146823
0.399697 0.422964
$69MIT
0.0923051 0.899285
0.173661 0.752901
0.292135 0.621834
0.396855 0.489345
0.486555 0.276594
0.573388 0.148206
$73HUL
0.104702 0.886872
0.203867 0.793095
0.30178 0.609412
0.40105 0.439565
0.49895 0.265564
0.599571 0.1137
0.700102 0.0268435
0.80192 0.00499681
0.902339 0.00112677
TABLE_END

$ 73Hair 773K
TABLE_HEAD 600
CREATE_NEW_EQUILIBRIUM @@,1
```

```
CHANGE_STATUS PHASE @1=FIX 1
SET-CONDITION P=P0,T=773,X(@1,CU)=@2
SET_REFERENCE_STATE AL FCC * 1E5
SET_REFERENCE_STATE CU FCC * 1E5
EXPERIMENT HMR(@1)=@3:1000
LABEL AHS
SET-ALL-START Y
TABLE_VALUES
 FCC       0.93        -6190
 FCC       0.86        -9150
 GAMMA_D83  0.69        -20290
 GAMMA_D83  0.66        -21290
 GAMMA_D83  0.637       -21190
 ALCU_DELTA 0.60        -20670
 ALCU_ZETA  0.55        -20400
 ALCU_ETA   0.5001      -19920
 ALCU_THETA 0.33        -13050
TABLE_END

TABLE_HEAD 700
CREATE_NEW_EQUILIBRIUM @@,1
CHANGE_STATUS PHASE @1=FIX 1
SET-CONDITION P=P0,T=298,X(@1,CU)=@2
SET_REFERENCE_STATE AL FCC * 1E5
SET_REFERENCE_STATE CU FCC * 1E5
EXPERIMENT HMR(@1)=@3:3000
LABEL AHS
SET-ALL-START Y
TABLE_VALUES
$ First-Principles VASP-GGA
 ALCU_GP    0.25        -9609
 ALCU_PRIME 0.3333      -20467
TABLE_END

CREATE_NEW_EQUILIBRIUM 800,1
CHANGE_STATUS PHASE ALCU_THETA=FIX 1
SET-CONDITION P=P0,T=298.15,X(ALCU_THETA,CU)=0.333
SET_REFERENCE_STATE AL FCC * 1E5
SET_REFERENCE_STATE CU FCC * 1E5
$Wolverton
EXPERIMENT SMR(ALCU_THETA)=-2.079:1
LABEL AHS
SET-ALL-START Y

CREATE_NEW_EQUILIBRIUM 801,1
CHANGE_STATUS PHASE ALCU_PRIME=FIX 1
SET-CONDITION P=P0,T=298.15,X(ALCU_PRIME,CU)=0.3333
SET_REFERENCE_STATE AL FCC * 1E5
SET_REFERENCE_STATE CU FCC * 1E5
$Wolverton
EXPERIMENT SMR(ALCU_PRIME)=-5.155:1
LABEL AHS
SET-ALL-START Y

TABLE_HEAD 900
CREATE_NEW_EQUILIBRIUM @@,1
```

```
CHANGE_STATUS PHASE @1=FIX 1
SET-CONDITION P=P0,T=298,X(@1,CU)=@2
SET_REFERENCE_STATE AL FCC * 1E5
SET_REFERENCE_STATE CU FCC * 1E5
EXPERIMENT HMR(@1)=@3:3000
LABEL AHS
SET-ALL-START Y
TABLE_VALUES
$FCC SQS
  FCC 0.25 -5869.63256
  FCC 0.5  -9495.25715
  FCC 0.75 -11266.64772
TABLE_END

BLOCKEND
$SOLVUS (FCC + Al2Cu)
TABLE_HEAD 1000
CREATE_NEW_EQUILIBRIUM @@,1
CHANGE_STATUS PHASE FCC,ALCU_THETA=FIX 1
ENTER_SYMBOL VARIABLE TK=@2+273.15;
EVALUATE TK
SET-CONDITION P=P0,T=TK
EXPERIMENT X(FCC,CU)=@1:DX
LABEL AS1
S-A-S Y
SET-START-VALUE Y(FCC,CU)=0.001
DELETE TK
TABLE_VALUES
$X(CU)       TEMPERATURE(C)
0.024796       547.8
0.021184       525.0
0.017607       500.0
0.014283       475.0
0.011338       450.0
0.008591       425.0
0.006424       400.0
0.004915       375.0
0.003627       350.0
0.002685       325.0
0.001916       300.0
0.00085        250.0
0.00196        300.0
0.00371        350.0
0.00423        360.0
0.00504        375.0
0.00668        400.0
0.01217        460.0
0.01734        500.0
0.0248         547.8
0.007500       418.8
0.010400       448.8
0.011500       455.8
0.014100       477.8
0.016000       491.8
0.017900       500.8
0.021500       523.8
```

```
0.022000        524.8
0.016800        499.8
0.013900        474.8
0.006700        399.8
0.002000        299.8
0.004200        353.8
0.006200        398.8
0.011500        449.8
0.017900        499.8
0.019400        513.8
0.022700        530.8
0.023800        539.8
0.012800        460.8
0.017100        489.8
0.020500        515.8
0.023300        531.8
TABLE_END

$LIQUIDUS (FCC + LIQUID)
TABLE_HEAD 1100
CREATE_NEW_EQUILIBRIUM @@,1
CHANGE_STATUS PHASE FCC,LIQUID=FIX 1
ENTER_SYMBOL VARIABLE TK=@3+273.15;
EVALUATE TK
SET-CONDITION P=P0,T=TK
EXPERIMENT X(LIQUID,CU)=@1:DX,X(FCC,CU)=@2:DX
LABEL ALF
S-A-S Y
SET-START-VALUE Y(LIQUID,CU)=@1 Y(FCC,CU)=@2
DELETE TK
TABLE_VALUES
$X(LIQUID,CU)   X(FCC,CU)     TEMPERATURE(C)
0.976800        0.990000      1081.4
0.954000        0.969800      1077.9
0.931900        0.950000      1074.9
0.910800        0.929700      1069.4
0.890000        0.909900      1062.4
0.869000        0.890000      1054.9
0.858900        0.890000      1051.9
0.848800        0.869900      1046.9
0.840000        0.859800      1040.9
0.830000        0.844000      1031.9
0.929700        0.954000      1076.9
0.909900        0.931900      1071.9
0.890000        0.910800      1062.9
0.869900        0.890000      1055.9
0.840000        0.869000      1048.9
0.835000        0.858900      1042.9
0.830000        0.844000      1031.9
$Al-rich side
0.008900        0.001000      655.2
0.050000        0.006400      630.8
0.056000        0.008200      626.8
0.100000        0.012800      599.8
0.139000        0.018600      573.8
0.102000        0.012800      598.8
```

```
0.131000        0.017100        579.8
0.152000        0.020500        564.8
0.166000        0.023300        554.8
0.026000        0.003300        643.7
0.016800        0.002500        647.8
0.004000        0.000700        656.8
0.166600        0.024000        551.8
0.164400        0.023900        553.3
0.160000        0.023000        557.3
0.008600        0.001550        652.0
0.026000        0.003830        640.0
0.045000        0.005790        630.0
0.096000        0.012200        600.0
0.154000        0.022200        561.0
TABLE_END

$LIQUIDUS (THETA + LIQUID)
TABLE_HEAD 1200
CREATE_NEW_EQUILIBRIUM @@,1
CHANGE_STATUS PHASE ALCU_THETA,LIQUID=FIX 1
ENTER_SYMBOL VARIABLE TK=@2+273.15;
EVALUATE TK
SET-CONDITION P=P0,T=TK
EXPERIMENT X(LIQUID,CU)=@1:DX
LABEL ALT
S-A-S Y
SET-START-VALUE Y(LIQUID,CU)=0.001
DELETE TK
TABLE_VALUES
$X(LIQUID,CU)   TEMPERATURE(C)
0.220617        566
0.258603        579
0.298048        587
0.31506        589
0.282000        585.8
0.289900        587.8
TABLE_END

$LIQUIDUS (ETA + LIQUID)
TABLE_HEAD 1250
CREATE_NEW_EQUILIBRIUM @@,1
CHANGE_STATUS PHASE ALCU_ETA,LIQUID=FIX 1
ENTER_SYMBOL VARIABLE TK=@3+273.15;
EVALUATE TK
SET-CONDITION P=P0,T=TK
EXPERIMENT X(LIQUID,CU)=@1:DX
LABEL ALET
S-A-S Y
SET-START-VALUE Y(LIQUID,CU)=0.001,Y(ALCU_ETA,CU)=0.01
DELETE TK
TABLE_VALUES
$X(LIQUID,CU)   X(ALCU_ETA,CU)       TEMPERATURE(C)
$33Sto
0.359900        0.5             620.8
0.350900        0.5             607.8
0.342000        0.5             597.8
```

```
$00Unk
0.322000        0.5             590.8
0.331000        0.5             591.8
0.335000        0.5             595.8
0.339800        0.5             600.8
0.348900        0.5             608.8
0.357900        0.5             619.8
0.363000        0.5             623.8
TABLE_END

$ Eutectic: LIQUID = FCC(AL) + AL2CU T=548.2C
CREATE_NEW_EQUILIBRIUM 1301,1
CHANGE_STATUS PHASE LIQUID,FCC,ALCU_THETA=FIX 1
SET-CONDITION P=P0
EXPERIMENT T=821.35:DT
EXPERIMENT X(FCC,CU)=0.0248:DX,X(LIQUID,CU)=0.171:DX
EXPERIMENT X(ALCU_THETA,CU)=0.319:DX
LABEL APE
SET-ALL-START 821.35 Y
SET-START-VALUE T=821.35 Y(LIQUID,CU)=0.171 Y(FCC,CU)=0.0248

$ Peritectic: LIQUID + Eta = AL2CU T=591C
CREATE_NEW_EQUILIBRIUM 1302,1
CHANGE_STATUS PHASE LIQUID,ALCU_ETA,ALCU_THETA=FIX 1
SET-CONDITION P=P0
EXPERIMENT T=864.15:DT
EXPERIMENT X(LIQUID,CU)=0.322:DX,X(ALCU_THETA,CU)=0.328:DX
EXPERIMENT X(ALCU_ETA,CU)=0.498:DX
LABEL APE
SET-ALL-START 864.15 Y
SET-START-VALUE T=864.15 Y(LIQUID,CU)=0.322 Y(ALCU_ETA,CU)=0.01

$ Peritectic: LIQUID + Epsilon = Eta T=624C
CREATE_NEW_EQUILIBRIUM 1303,1
CHANGE_STATUS PHASE LIQUID,ALCU_ETA,ALCU_EPSILON=FIX 1
SET-CONDITION P=P0
EXPERIMENT T=897.15:DT
EXPERIMENT X(LIQUID,CU)=0.363:DX,X(ALCU_EPSILON,CU)=0.55:DX
EXPERIMENT X(ALCU_ETA,CU)=0.518:DX
LABEL APE
SET-ALL-START 897.15 Y
SET-START-VALUE T=897.15 Y(LIQUID,CU)=0.363 Y(ALCU_EPSILON,CU)=0.1
SET-START-VALUE Y(ALCU_ETA,CU)=0.01

$ eutectoid: epsilon=Eta +delta T<580C
CREATE_NEW_EQUILIBRIUM 1304,1
CHANGE_STATUS PHASE ALCU_EPSILON,ALCU_ETA,ALCU_DELTA=FIX 1
SET-CONDITION P=P0
EXPERIMENT T<853:1
LABEL APE
SET-ALL-START 853 Y
SET-START-VALUE T=853 Y(ALCU_EPSILON,CU)=0.1 Y(ALCU_ETA,CU)=0.01

$ Congruent  ZETA = EPSILON 590C
CREATE_NEW_EQUILIBRIUM 1305,1
CHANGE_STATUS PHASE ALCU_ZETA,ALCU_EPSILON=FIX 1
```

```
SET-CONDITION P=P0,X(ALCU_ZETA,CU)-X(ALCU_EPSILON,CU)=0
EXPERIMENT T=863:DT
$EXPERIMENT X(ALCU_ZETA,CU)=0.55:DX
LABEL APE
SET-ALL-START 863.15 Y
SET-START-VALUE T=863.15 Y(ALCU_EPSILON,CU)=0.1

$ Peritectic: LIQUID + GAMMA_H = EPSILON T=958C
CREATE_NEW_EQUILIBRIUM 1306,1
CHANGE_STATUS PHASE LIQUID,ALCU_EPSILON,GAMMA_H=FIX 1
SET-CONDITION P=P0
EXPERIMENT T=1231.15:DT
EXPERIMENT X(LIQUID,CU)=0.598:DX,X(ALCU_EPSILON,CU)=0.621:DX
$EXPERIMENT X(GAMMA_H,CU)=0.629:DX
LABEL APE
SET-ALL-START 1231.15 Y
SET-START-VALUE T=1231.15 Y(LIQUID,CU)=0.598 Y(ALCU_EPSILON,CU)=0.24
SET-START-VALUE Y(GAMMA_H,CU)=0.1

$ Peritectoid: Epsilon + GAMMA_D83 = Delta T=686C
CREATE_NEW_EQUILIBRIUM 1307,1
CHANGE_STATUS PHASE ALCU_DELTA,ALCU_EPSILON,GAMMA_D83=FIX 1
SET-CONDITION P=P0
EXPERIMENT T=959.15:DT
EXPERIMENT X(ALCU_EPSILON,CU)=0.592:DX
EXPERIMENT X(GAMMA_D83,CU)=0.628:DX
$EXPERIMENT X(ALCU_DELTA,CU)=0.619:DX
LABEL APE
SET-ALL-START 959.15 Y
SET-START-VALUE T=959.15 Y(GAMMA_D83,CU)=0.1
SET-START-VALUE Y(ALCU_EPSILON,CU)=0.2

$ Congruent Melting: BCC_A2 = LIQUID T=1049C
CREATE_NEW_EQUILIBRIUM 1308,1
CHANGE_STATUS PHASE LIQUID,BCC_A2=FIX 1
SET-CONDITION P=P0,X(LIQUID,CU)-X(BCC_A2,CU)=0
EXPERIMENT T=1322.15:DT
EXPERIMENT X(BCC_A2,CU)=0.75:DX
LABEL APE
SET-ALL-START 1322.15 Y
SET-START-VALUE T=1322.15 Y(LIQUID,CU)=0.9 Y(BCC_A2,CU)=0.9

$ Eutectoid: BCC_A2 = FCC(CU) + GAMMA_D83 T=567C
CREATE_NEW_EQUILIBRIUM 1309,1
CHANGE_STATUS PHASE BCC_A2,FCC,GAMMA_D83=FIX 1
SET-CONDITION P=P0
EXPERIMENT T=840.15:DT
EXPERIMENT X(FCC,CU)=0.803:DX,X(GAMMA_D83,CU)=0.69:DX
EXPERIMENT X(BCC_A2,CU)=0.761:DX
LABEL APE
SET-ALL-START 840.15 Y
SET-START-VALUE T=840.15 Y(BCC_A2,CU)=0.761 Y(FCC,CU)=0.803

$ Eutectic: LIQUID = FCC(CU) + BCC_A2 T=1032C
CREATE_NEW_EQUILIBRIUM 1310,1
CHANGE_STATUS PHASE LIQUID,BCC_A2,FCC=FIX 1
```

```
SET-CONDITION P=P0
EXPERIMENT T=1305.15:DT
EXPERIMENT X(FCC,CU)=0.842:DX,X(LIQUID,CU)=0.83:DX
EXPERIMENT X(BCC_A2,CU)=0.82:DX
LABEL APE
SET-ALL-START 1305.15 Y
SET-START-VALUE Y(FCC,CU)=0.842 Y(LIQUID,CU)=0.83 Y(BCC_A2,CU)=0.82

$SOLVUS (FCC + THETA PRIME)
TABLE_HEAD 1400
CREATE_NEW_EQUILIBRIUM @@,1
CHANGE_STATUS PHASE FCC,ALCU_PRIME=FIX 1
E-SYM VARIA TK=@2+273.15;
EVALUATE TK
SET-CONDITION P=P0,T=TK
EXPERIMENT X(FCC,CU)=@1:DX
LABEL AS2
S-A-S Y
SET-START-VALUE Y(FCC,CU)=@1
DELETE TK
TABLE_VALUES
$73Hor
0.00436468 249.146
0.00650315 314.84
0.00876826 344.716
0.013285   383.415
0.0176503  402.749
TABLE_END

$SOLVUS (FCC + Al3Cu)
TABLE_HEAD 1500
CREATE_NEW_EQUILIBRIUM @@,1
CHANGE_STATUS PHASE FCC,ALCU_GP=FIX 1
E-SYM VARIA TK=@2+273.15;
EVALUATE TK
SET-CONDITION P=P0,T=TK
EXPERIMENT X(FCC,CU)=@1:DX
LABEL AS3
S-A-S Y
SET-START-VALUE Y(FCC,CU)=@1
DELETE TK
TABLE_VALUES
$57Beton high
0.0126178 221.333
0.0198549 245.333
0.0229135 249.333
$73Sat high
0.00690479 178.667
0.00690275 170.667
0.0149331 226.667
0.0149727 220
TABLE_END

TABLE_HEAD 1600
CREATE_NEW_EQUILIBRIUM @@,1
CHANGE_STATUS PHASE LIQUID,GAMMA_H=FIX 1
```

```
E-SYM VARIA TK=@2+273.15;
EVALUATE TK
SET-CONDITION P=P0,X(LIQUID,AL)=@1
EXPERIMENT T=TK:DT
LABEL AGA
SET-ALL-START @2 Y
SET-START-VALUE Y(LIQUID,AL)=@1,Y(GAMMA_H,AL)=0.5
DELETE TK
TABLE_VALUES
$ 98Liu
 0.34        1025
 0.37        980
TABLE_END

TABLE_HEAD 1700
CREATE_NEW_EQUILIBRIUM @@,1
CHANGE_STATUS PHASE LIQUID,GAMMA_H=FIX 1
E-SYM VARIA TK=@2+273.15;
EVALUATE TK
SET-CONDITION P=P0,X(GAMMA_H,AL)=@1
EXPERIMENT T=TK:DT
LABEL AGA
SET-ALL-START @2 Y
SET-START-VALUE Y(LIQUID,AL)=0.4,Y(GAMMA_H,AL)=@1
DELETE TK
TABLE_VALUES
$98Liu
 0.34        991
 0.37        962.4
TABLE_END

$ SOLIDUS (FCC + BCC)
TABLE_HEAD 1800
CREATE_NEW_EQUILIBRIUM @@,1
CHANGE_STATUS PHASE FCC,BCC_A2=FIX 1
E-SYM VARIA TK=@3+273.15;
EVALUATE TK
SET-CONDITION P=P0,T=TK
EXPERIMENT X(FCC,CU)=@1:DX,X(BCC_A2,CU)=@2:DX
LABEL AFB
S-A-S Y
SET-START-VALUE Y(FCC,CU)=@1 Y(BCC_A2,CU)=@2
DELETE TK
TABLE_VALUES
$X(FCC,CU)   X(BCC,CU)    TEMPERATURE(C)
$72Lin
0.8075      0.7712      650.0
0.8120      0.7761      700.0
0.8146      0.7810      747.0
0.8237      0.7859      800.0
0.8281      0.7931      850.0
0.8329      0.8003      900.0
0.8337      0.8051      925.0
0.8364      0.8070      950.0
0.8402      0.8109      975.0
0.8402      0.8150      1000.0
```

```
0.8439      0.8195      1023.0
0.8030      0.7608      572.0
0.8040      0.7651      598.0
TABLE_END

TABLE_HEAD 1900
CREATE_NEW_EQUILIBRIUM @@,1
CHANGE_STATUS PHASE LIQUID,BCC_A2=FIX 1
E-SYM VARIA TK=@3+273.15;
EVALUATE TK
SET-CONDITION P=P0,X(BCC_A2,CU)=@2
EXPERIMENT X(LIQUID,CU)=@1:DX,T=TK:DT
LABEL ALB
$SET-ALL-START TK Y
SET-ALL-START @3 Y
SET-START-VALUE Y(LIQUID,CU)=@1 Y(BCC_A2,CU)=@2
DELETE TK
TABLE_VALUES
$33Sto Phase boundary of liquid + bcc
0.830000   0.814000       1036.0
0.820000   0.807000       1040.0
0.808000   0.798000       1044.0
0.792000   0.785000       1048.0
0.765000   0.765000       1050.0
0.737000   0.744000       1048.0
0.720000   0.732000       1048.0
0.708000   0.723000       1040.0
TABLE_END

$ SOLIDUS (FCC + BCC)
TABLE_HEAD 2000
CREATE_NEW_EQUILIBRIUM @@,1
CHANGE_STATUS PHASE FCC,BCC_A2=FIX 1
E-SYM VARIA TK=@3+273.15;
EVALUATE TK
SET-CONDITION P=P0,T=TK
EXPERIMENT X(FCC,AL)=@1:DX,X(BCC_A2,AL)=@2:DX
LABEL AFB
S-A-S Y
SET-START-VALUE Y(FCC,AL)=@1 Y(BCC_A2,AL)=@2
DELETE TK
TABLE_VALUES
$X(FCC,AL)   X(BCC,AL)     TEMPERATURE(C)
$98Liu
0.171       0.195       900
0.174       0.208       850
0.175       0.210       800
0.180       0.215       780
0.189       0.225       700
0.198       0.232       600
TABLE_END

TABLE_HEAD 2100
CREATE_NEW_EQUILIBRIUM @@,1
CHANGE_STATUS PHASE LIQUID,BCC_A2=FIX 1
E-SYM VARIA TK=@2+273.15;
```

```
EVALUATE TK
SET-CONDITION P=P0,X(LIQUID,AL)=@1
EXPERIMENT T=TK:DT
LABEL ALB
SET-ALL-START @2 Y
SET-START-VALUE Y(LIQUID,AL)=@1,Y(BCC_A2,AL)=@1
DELETE TK
TABLE_VALUES
$98Liu
 0.25        1049
 0.30        1041
TABLE_END

$ FCC+GAMMA_D83
TABLE_HEAD 2200
CREATE_NEW_EQUILIBRIUM @@,1
CHANGE_STATUS PHASE FCC,GAMMA_D83=FIX 1
E-SYM VARIA TK=@3+273.15;
EVALUATE TK
SET-CONDITION P=P0,T=TK
EXPERIMENT X(FCC,AL)=@1:DX,X(GAMMA_D83,AL)=@2:DX
LABEL AGA
S-A-S Y
SET-START-VALUE Y(FCC,AL)=0.2 Y(GAMMA_D83,AL)=0.01
DELETE TK
TABLE_VALUES
$X(FCC,AL)   X(GAMMA_D83,AL)     TEMPERATURE(C)
$98Liu
0.202       0.32              500
TABLE_END

$ LIQUIDUS (LIQUID + EPSILON)
TABLE_HEAD 2300
CREATE_NEW_EQUILIBRIUM @@,1
CHANGE_STATUS PHASE LIQUID,ALCU_EPSILON=FIX 1
E-SYM VARIA TK=@2+273.15;
EVALUATE TK
SET-CONDITION P=P0,T=TK
EXPERIMENT X(LIQUID,CU)=@1:DX
LABEL ALE
S-A-S Y
SET-START-VALUE Y(LIQUID,CU)=0.01 Y(ALCU_EPSILON,CU)=0.2
DELETE TK
TABLE_VALUES
$X(LIQUID,CU)   TEMPERATURE(C)
$85Mur
0.39          650.0
0.42          700.0
0.46          750.0
0.49          800.0
0.53          850.0
0.56          900.0
TABLE_END

$ LIQUIDUS (LIQUID + EPSILON)
TABLE_HEAD 2400
```

```
CREATE_NEW_EQUILIBRIUM @@,1
CHANGE_STATUS PHASE LIQUID,ALCU_EPSILON=FIX 1
E-SYM VARIA TK=@3+273.15;
EVALUATE TK
SET-CONDITION P=P0,T=TK
EXPERIMENT X(LIQUID,AL)=@1:DX,X(ALCU_EPSILON,AL)=@2:DX
LABEL ALE
S-A-S Y
SET-START-VALUE Y(LIQUID,CU)=0.4 Y(ALCU_EPSILON,CU)=0.24
DELETE TK
TABLE_VALUES
$X(LIQUID,AL)   X(ALCU_EPSILON,AL)     TEMPERATURE(C)
$ 98Liu
0.514         0.421              800.0
0.589         0.439              700.0
0.455         0.394              900.0
TABLE_END

$ BCC+GAMMA_D83
TABLE_HEAD 2500
CREATE_NEW_EQUILIBRIUM @@,1
CHANGE_STATUS PHASE BCC_A2,GAMMA_D83=FIX 1
E-SYM VARIA TK=@3+273.15;
EVALUATE TK
SET-CONDITION P=P0,T=TK
EXPERIMENT X(BCC_A2,AL)=@1:DX,X(GAMMA_D83,AL)=@2:DX
LABEL AGA
S-A-S Y
SET-START-VALUE Y(BCC_A2,AL)=0.1 Y(GAMMA_D83,AL)=0.01
DELETE TK
TABLE_VALUES
$X(BCC,AL)   X(GAMMA_D83,AL)     TEMPERATURE(C)
$98Liu
0.255       0.319             600
0.259       0.319             700
0.270       0.32             780
0.273       0.321             800
TABLE_END

$ BCC+GAMMA_H
TABLE_HEAD 2600
CREATE_NEW_EQUILIBRIUM @@,1
CHANGE_STATUS PHASE BCC_A2,GAMMA_H=FIX 1
E-SYM VARIA TK=@3+273.15;
EVALUATE TK
SET-CONDITION P=P0,T=TK
EXPERIMENT X(BCC_A2,AL)=@1:DX,X(GAMMA_H,AL)=@2:DX
LABEL AGA
S-A-S Y
SET-START-VALUE Y(BCC_A2,AL)=0.1 Y(GAMMA_H,AL)=0.01
DELETE TK
TABLE_VALUES
$X(BCC,AL)   X(GAMMA_H,AL)       TEMPERATURE(C)
$98Liu
0.28        0.319             850
0.289       0.316             900
```

```
0.303       0.314             1000
TABLE_END

$ GAMMA_D83+EPSILON
TABLE_HEAD 2700
CREATE_NEW_EQUILIBRIUM @@,1
CHANGE_STATUS PHASE ALCU_EPSILON,GAMMA_D83=FIX 1
E-SYM VARIA TK=@3+273.15;
EVALUATE TK
SET-CONDITION P=P0,T=TK
EXPERIMENT X(ALCU_EPSILON,AL)=@1:DX
EXPERIMENT X(GAMMA_D83,AL)=@2:DX
LABEL AGA
S-A-S Y
SET-START-VALUE Y(ALCU_EPSILON,al)=0.75 Y(GAMMA_D83,AL)=0.9
DELETE TK
TABLE_VALUES
$X(EPSILON,AL)   X(GAMMA_D83,AL)     TEMPERATURE(C)
$98Liu
0.395         0.377            800
0.408         0.384            700
TABLE_END

$ GAMMA_H+EPSILON
TABLE_HEAD 2800
CREATE_NEW_EQUILIBRIUM @@,1
CHANGE_STATUS PHASE ALCU_EPSILON,GAMMA_H=FIX 1
E-SYM VARIA TK=@3+273.15;
EVALUATE TK
SET-CONDITION P=P0,T=TK
EXPERIMENT X(ALCU_EPSILON,AL)=@1:DX
$EXPERIMENT X(GAMMA_H,AL)=@2:DX
LABEL AGA
S-A-S Y
SET-START-VALUE Y(ALCU_EPSILON,CU)=0.24 Y(GAMMA_H,AL)=0.9
DELETE TK
TABLE_VALUES
$X(EPSILON,AL)   X(GAMMA_H,AL)       TEMPERATURE(C)
$98Liu
0.386         0.374            900
TABLE_END

SAVE_WORKSPACES
```

APPENDIX C. THERMO-CALC DATABASE FILE FOR AL-CU SYSTEM

```
ELEMENT VA   VACUUM                0.0000E+00  0.0000E+00  0.0000E+00!
ELEMENT AL   FCC_A1                2.6982E+01  4.5773E+03  2.8322E+01!
ELEMENT CU   FCC_A1                6.3546E+01  5.0041E+03  3.3150E+01!

FUNCTION GHSERAL    298.15  -7976.15+137.071542*T-24.3671976*T*LN(T)
   -.001884662*T**2-8.77664E-07*T**3+74092*T**(-1);  7.00000E+02  Y
    -11276.24+223.02695*T-38.5844296*T*LN(T)+.018531982*T**2
   -5.764227E-06*T**3+74092*T**(-1);  9.33600E+02  Y
    -11277.683+188.661987*T-31.748192*T*LN(T)-1.234264E+28*T**(-9);
   2.90000E+03  N !
FUNCTION GHSERCU    298.15  -7770.458+130.485403*T-24.112392*T*LN(T)
   -.00265684*T**2+1.29223E-07*T**3+52478*T**(-1);  1.35802E+03  Y
    -13542.33+183.804197*T-31.38*T*LN(T)+3.64643E+29*T**(-9);  3.20000E+03
    N !
FUNCTION GCUBCC   298.15  +4017-1.255*T+GHSERCU#;  6000  N !
FUNCTION GALBCC   298.15  +10083-4.813*T+GHSERAL#;  6000 N !

TYPE_DEFINITION % SEQ *!
DEFINE_SYSTEM_DEFAULT SPECIE 2 !
DEFAULT_COMMAND DEF_SYS_ELEMENT VA !

PHASE LIQUID:L %  1  1.0  !
CONSTITUENT LIQUID:L :AL,CU :  !

PARAMETER G(LIQUID,AL;0)  298.15  +11005.553-11.840873*T
  +7.9401E-20*T**7+GHSERAL#;  9.33600E+02  Y
  +10481.974-11.252014*T+1.234264E+28*T**(-9)+GHSERAL#;  2.90000E+03 N !
PARAMETER G(LIQUID,CU;0)  298.15  +12964.84-9.510243*T
  -5.83932E-21*T**7+GHSERCU#;  1.35802E+03  Y
  +13495.4-9.920463*T-3.64643E+29*T**(-9)+GHSERCU#;  3.20000E+03  N !
PARAMETER G(LIQUID,AL,CU;0) 298.15 -66054+8.363*T;   6000   N !
PARAMETER G(LIQUID,AL,CU;1) 298.15 32489-8.524*T;   6000   N !
PARAMETER G(LIQUID,AL,CU;2) 298.15 7420-10.702*T;   6000   N !

TYPE_DEFINITION ( GES A_P_D FCC_A1 MAGNETIC  -3.0    2.80000E-01 !
PHASE FCC_A1  %(  2 1   1 !
CONSTITUENT FCC_A1  :AL%,CU% : VA% :  !

PARAMETER G(FCC_A1,AL:VA;0)  298.15  +GHSERAL#;   6000 N !
PARAMETER G(FCC_A1,CU:VA;0)  298.15  +GHSERCU#;   6000 N !
PARAMETER G(FCC_A1,AL,CU:VA;0) 298.15 -43205-4.630*T; 6000 N !
PARAMETER G(FCC_A1,AL,CU:VA;1) 298.15 45224-6.789*T; 6000 N !
PARAMETER G(FCC_A1,AL,CU:VA;2) 298.15 -16747+11.614*T; 6000 N !

PHASE ALCU_THETA  %  2 0.6667  0.3333 !
CONSTITUENT ALCU_THETA  :AL : AL,CU :  !

PARAMETER G(ALCU_THETA,AL:AL;0)  298.15  +GALBCC#; 6000 N !
PARAMETER G(ALCU_THETA,AL:CU;0)  298.15  -16025+2.719*T
  +0.6667*GHSERAL#+0.3333*GHSERCU#; 6000 N !

PHASE ALCU_PRIME  %  2 0.6667  0.3333 !
```

```
CONSTITUENT ALCU_PRIME  :AL : CU :  !

PARAMETER G(ALCU_PRIME,AL:CU;0)  298.15  -16783+5.434*T
  +0.6667*GHSERAL#+0.3333*GHSERCU#; 6000 N !

PHASE ALCU_GP  %  2 .75   .25 !
CONSTITUENT ALCU_GP  :AL: CU : !

PARAMETER G(ALCU_GP,AL:CU;0) 298.15 -8389+0.385*T
  +.75*GHSERAL#+.25*GHSERCU#;   6000 N !

TYPE_DEFINITION & GES A_P_D BCC_A2 MAGNETIC  -1.0    4.00000E-01 !
PHASE BCC_A2  %&  2 1   3 !
CONSTITUENT BCC_A2  :AL,CU : VA% :  !

PARAMETER G(BCC_A2,AL:VA;0)  298.15  +GALBCC#;  2.90000E+03 N !
PARAMETER G(BCC_A2,CU:VA;0)  298.15  +GCUBCC#;  3.20000E+03 N !
PARAMETER G(BCC_A2,AL,CU:VA;0)  298.15  -73083+4.810*T; 6000 N !
PARAMETER G(BCC_A2,AL,CU:VA;1)  298.15  48345-7.216*T; 6000 N !

PHASE ALCU_EPSILON  %  2 .5   .5 !
CONSTITUENT ALCU_EPSILON  :AL,CU : CU :  !

PARAMETER G(ALCU_EPSILON,AL:CU;0) 298.15 -20313+3.000*T
  +.5*GHSERAL#+.5*GHSERCU#;   6000 N !
PARAMETER G(ALCU_EPSILON,CU:CU;0) 298.15 22019+GHSERCU#; 6000 N !
PARAMETER G(ALCU_EPSILON,AL,CU:CU;0) 298.15 -29635-27.517*T; 6000 N !

PHASE ALCU_ETA  %  2 .5   .5 !
CONSTITUENT ALCU_ETA  :AL,CU : CU :  !

PARAMETER G(ALCU_ETA,AL:CU;0)  298.15  -20315+2.079*T
  +.5*GHSERAL#+.5*GHSERCU#; 6000 N !
PARAMETER G(ALCU_ETA,CU:CU;0)  298.15  +GCUBCC#; 6000 N !
PARAMETER G(ALCU_ETA,AL,CU:CU;0)  298.15 -17953; 6000 N !

PHASE ALCU_DELTA  %  2 .4   .6 !
CONSTITUENT ALCU_DELTA  :AL : CU :  !

PARAMETER G(ALCU_DELTA,AL:CU;0)  298.15  -22278+1.702*T
  +.4*GHSERAL#+.6*GHSERCU#; 6000 N !

PHASE ALCU_ZETA  %  2 .45   .55 !
CONSTITUENT ALCU_ZETA  :AL : CU :  !

PARAMETER G(ALCU_ZETA,AL:CU;0)  298.15  -21384+1.960*T
  +.45*GHSERAL#+.55*GHSERCU#; 6000 N !

PHASE GAMMA_D83  %  3 .3077   .0769   .6154 !
CONSTITUENT GAMMA_D83  :AL : AL,CU : CU :  !

PARAMETER G(GAMMA_D83,AL:AL:CU;0)  298.15  -24185+31*T-4*T*LN(T)
  +.3846*GHSERAL#+.6154*GHSERCU#;   6000   N !
PARAMETER G(GAMMA_D83,AL:CU:CU;0)  298.15  -20622+28.5*T-4*T*LN(T)
  +.3077*GHSERAL#+.6923*GHSERCU#;   6000   N !
```

```
PHASE GAMMA_H  %  3 .3077   .0769   .6154 !
CONSTITUENT GAMMA_H  :AL : AL,CU : CU :  !

PARAMETER G(GAMMA_H,AL:AL:CU;0)  298.15  -16339-4*T+.3846*GHSERAL#
  +.6154*GHSERCU#;   6000   N !
PARAMETER G(GAMMA_H,AL:CU:CU;0)  298.15  -15185-4.5*T+.3077*GHSERAL#
  +.6923*GHSERCU#;   6000   N !
```

REFERENCES

1. A. Guinier, *Nature,* **142** (1938) 569.
2. G. D. Preston, *Proc. Roy. Soc. A,* **167** (1938) 526-538.
3. C. Wolverton, *Philos. Mag. Lett.,* **79** (1999) 683-690.
4. J. J. Pepe and W. F. Savage, *Welding Journal,* **46** (1967) 411-422.
5. D. B. Miracle, *Acta Mater,* **41** (1993) 649-684.
6. M. Kogachia, T. Haraguchia and S. M. Kim, *Intermetallics,* **6** (1998) 499-510.
7. J. L. Jordan and S. C. Deevi, *Intermetallics,* **11** (2003) 507-528.
8. A. J. Bradley and A. Taylor, *Proc. R. Soc. London, Ser. A,* **159** (1937) 56.
9. H. Xiao and I. Baker, *Acta Mater,* **43** (1995) 391-396.
10. I. Baker, *Mater. Sci. Eng. A,* **193** (1995) 1-13.
11. Y. Mishin, A. Y. Lozovoi and A. Alavi, *Phys. Rev. B,* **67** (2003) 014201.
12. M. Fähnle, B. Meyer and G. Bester, *Intermetallics,* **7** (1999) 1307-1308.
13. L. Kaufman and H. Bernstein, *Computer Calculation of Phase Diagrams* (Academic Press, New York, 1970).
14. B. Sundman, B. Jansson and J.-O. Andersson, *CALPHAD,* **9** (1985) 153-190.
15. J.-O. Andersson, T. Helander, L. Hoglund, P. Shi and B. Sundman, *Calphad,* **26** (2002) 273-312.
16. W. Kohn and L. Sham, *Phys. Rev. A,* **140** (1965) 1133.
17. C. Wolverton and A. Zunger, *Phys. Rev. Lett.,* **75** (1995) 3162-3165.
18. A. Zunger, L. G. Wang, G. L. W. Hart and M. Sanati, *Model. Simul. Mater. Sc.,* **10** (2002) 685-706.

19. A. van de Walle and M. Asta, *Model. Simul. Mater. Sc.,* **10** (2002) 521-538.

20. A. van de Walle and G. Ceder, *Journal of Phase Equilibria (USA),* **23** (2002) 348-359.

21. C. Wolverton and V. Ozolins, *Phys. Rev. Lett.,* **86** (2001) 5518-5521.

22. S. Baroni, P. Giannozzi and A. Testa, *Phys. Rev. Lett.,* **58** (1987) 1861.

23. I. Ansara, A. T. Dinsdale and M. H. Rand, Eds., *COST 507: Thermochemical Database for Light Metal Alloys*, vol. 2 (European Commission, 1998).

24. C. Wolverton, X. Y. Yan, R. Vijayaraghavan and V. Ozolins, *Acta Mater.,* **50** (2002) 2187-2197.

25. D. A. Porter and K. E. Easterling, *Phase transformations in metals and alloys*.

26. R. H. Beton and E. C. Rollason, *Journal of the Institute of Metals,* **86** (1957-58) 77-85.

27. K. G. Satyanarayana, K. Jayapalan and T. R. Anantharaman, *Current Science,* **41** (1973) 6-9.

28. A. T. Dinsdale, *CALPHAD,* **15** (1991) 317-425.

29. O. Redlich and A. T. Kister, *Ind. Eng. Chem.,* **40** (1948) 345-348.

30. M. Hillert and L. Staffansson, *Acta Chem. Scand.,* **24** (1970) 3618-3626.

31. D. M. Ceperley and B. J. Alder, *Phys. Rev. Lett.,* **45** (1980) 566.

32. J. P. Perdew and A. Zunger, *Phys. Rev. B,* **23** (1981) 5048.

33. J. W. D. Connolly and A. R. Williams, *Phys. Rev. B,* **27** (1983) 5169-5172.

34. A. Zunger, S. H. Wei, L. G. Ferreira and J. E. Bernard, *Phys. Rev. Lett.,* **65** (1990) 353-356.

35. S. H. Wei, L. G. Ferreira, J. E. Bernard and A. Zunger, *Phys. Rev. B,* **42** (1990) 9622-9649.

36. B. L. Gyorffy, *Phys. Rev. B,* **5** (1972) 2382-2384.

37. Z. W. Lu, S. H. Wei and A. Zunger, *Phys. Rev. B,* **44** (1991) 3387-3390.

38. Z. W. Lu, S. H. Wei and A. Zunger, *Phys. Rev. B,* **45** (1992) 10314-10330.

39. A. V. Ruban, S. I. Simak, S. Shallcross and H. L. Skriver, *Phys. Rev. B,* **67** (2003) 214302.

40. J. C. Mikkelsen and J. B. Boyce, *Phys. Rev. Lett.,* **49** (1982) 1412-1415.

41. K. C. Hass, L. C. Davis and A. Zunger, *Phys. Rev. B,* **42** (1990) 3757-3760.

42. V. Ozolins, C. Wolverton and A. Zunger, *Phys. Rev. B,* **57** (1998) 6427-6443.

43. C. Wolverton, *Acta Mater,* **49** (2001) 3129-3142.

44. A. van de Walle, M. Asta and G. Ceder, *Calphad,* **26** (2003) 539-553.

45. H. T. Stokes and D. M. Hatch, *www.physics.byu.edu/~stokesh/isotropy.html,* FINDSYM, www.physics.byu.edu/~stokesh/isotropy.html (2001),

46. D. Vanderbilt, *Phys. Rev. B,* **41** (1990) 7892-7895.

47. G. Kresse and J. Hafner, *J. Phys.-Condes. Matter,* **6** (1994) 8245-8257.

48. G. Kresse and J. Furthmuller, *Phys. Rev. B,* **54** (1996) 11169-11186.

49. G. Kresse and J. Furthmuller, *Comput. Mater. Sci.,* **6** (1996) 15-50.

50. J. P. Perdew, J. A. Chevary, S. H. Vosko, K. A. Jackson, M. R. Pederson, D. J. Singh and C. Fiolhais, *Phys. Rev. B,* **46** (1992) 6671-6687.

51. C. Amador, W. R. L. Lambrecht and B. Segall, *Phys. Rev. B,* **46** (1992) 1870.

52. H. J. Monkhorst and J. D. Pack, *Phys. Rev. B,* **13** (1972) 5188.

53. P. G. Evans, E. D. Isaacs, G. Aeppli, Z. Cai and B. Lai, *Science,* **295** (2002) 1042.

54. N. Kimura and Y. Kakehashi, *J. Magn. Magn. Mater.,* **226-230** (2001) 1019-1020.

55. E. Fawcett, H. L. Alberts, V. Y. Galkin, D. R. Noakes and J. V. Yakhmi, *Rev. Mod. Phys.,* **66** (1994) 25.

56. S. C. Singhal and W. L. Worrell, *Metall. Trans.,* **4** (1973) 1125-1128.

57. H. J. Goldschmidt and J. A. Brand, *J. Less-Common Met.,* **3** (1961) 44.

58. J. A. Catterall and S. M. Barker, *Plansee Proc.,* (1964) 577.

59. C. Sigli, M. Kosugi and J. M. Sanchez, *Phys. Rev. Lett.,* **57** (1986) 253-256.

60. S. C. Singhal and W. L. Worrell, *Metall. Trans.,* **4** (1973) 895-898.

61. R. Krishnan, S. P. Garg and N. Krishnamurthy, *J. Alloy Phase Diagrams,* **3** (1987) 1.

62. P. E. A. Turchi, A. Gonis, V. Drchal and J. Kudrnovsky, *Phys. Rev. B,* **64** (2001) 085112.

63. N. K. Arkhipova, S. M. Klotsman, I. P. Polikarpova, G. N. Tatarinova, A. N. Timofeev and L. M. Veretennikov, *Phys. Rev. B,* **30** (1984) 1788-1796.

64. V. P. Itkin, in *Phase diagrams of binary iron alloys* H. Okamoto, Ed. (ASM International, Materials Park, OH, 1993) pp. 102-129.

65. G. D. Preston, *Philos. Mag.,* **13** (1932) 419-425.

66. A. T. Aldred, *Phys. Rev. B,* **14** (1976) 219-227.

67. Y. A. Dorofeyev, A. Z. Menshikov and G. A. Takzey, *Phys. Met. Metallogr.,* **55** (1983) 102-109.

68. N. I. Kulikov and C. Demangeat, *Phys. Rev. B,* **55** (1997) 3533-3542.

69. W. A. Dench, *Trans. Faraday Soc.,* **59** (1962) 1279.

70. H. Akai and P. H. Dederichs, *Phys. Rev. B,* **47** (1993) 8739-8747.

71. P. Olsson, I. A. Abrikosov, L. Vitos and J. Wallenius, *J. Nuclear Mat.,* **321** (2003) 84-90.

72. P. J. Craievich, M. Weinert, J. M. Sanchez and R. E. Watson, *Physical Review Letters,* **72** (1994) 3076-3079.

73. M. Sob, L. G. Wang and V. Vitek, *Computational Materials Science,* **8** (1997) 100-106.

74. L. G. Wang, M. Sob and Z. Y. Zhang, *Journal of Physics and Chemistry of Solids,* **64** (2003) 863-872.

75. S. Muller, L. W. Wang, A. Zunger and C. Wolverton, *Phys. Rev. B,* **60** (1999) 16448-16462.

76. J. Hair and D. B. Downie, *Faraday Symp. Chem. Soc.,* **8** (1973) 56-63.

77. W. Oelsen and W. Middel, *Mitt. Kaiser Wilhelm Inst. Eisenforsch. (Dusseldrof),* **19** (1937) 1-26.

78. J. L. Murray, *Int. Met. Rev.,* **30** (1985) 211-233.

79. X. J. Liu, I. Ohnuma, R. Kainuma and K. Ishida, *J. Alloy. Compd.,* **264** (1998) 201-208.

80. U. K. Stolz, I. Arpshofen, F. Sommer and B. Predel, *J. Phase Equilibria,* **14** (1993) 473-478.

81. V. Witusiewicz, U. K. Stolz, I. Arpshofen and F. Sommer, *Z. Metallkd.,* **89** (1998) 704-713.

82. D. S. Kanibolotsky, O. A. Bieloborodova, N. V. Kotova and V. V. Lisnyak, *Journal of thermal analysis and calorimetry,* **70** (2002) 975-983.

83. B. Jansson, *Trita-Mac-0234* (Royal Institute of Technology, Stockholm, Sweden, 1984).

84. Y. Wang, S. Curtarolo, C. Jiang, R. Arroyave, T. Wang, G. Ceder, L. Q. Chen and Z. K. Liu, *CALPHAD,* (2004) in press.

85. R. Hultgren, P. D. Desai, D. T. Hawkins, M. Gleiser and K. K. Kelley, *Selected Value of the Thermodynamic Properties of Binary Alloys* (ASM, Metal Park, OH, 1973).

86. G. Grube and P. Hantelmann, *Z. Elektrochem.,* **48** (1942) 90.

87. R. Hultgren, R. L. Orr and K. K. Kelley, *Supplement to Selected Value of the Thermodynamic Properties of Binary Alloys* (ASM, Metal Park, OH, 1973).

88. G. I. Batalin, E. A. Beloborodova and V. N. Vasilev, *Ukr. Khim. Zh.,* **38** (1972) 920-923.

89. T. C. Wilder, *Trans. Metall. Soc. AIME,* **233** (1965) 1202.

90. H. Mitani and H. Nagai, *J. Jpn. Inst. Met.,* **33** (1969) 344.

91. H. Hori and K. Hirano, *J. Jpn. Inst. Met.,* **37** (1973) 142-148.

92. G. Borelius, J. Anderson and K. Gullberg, *Ing. Vetenskaps Akad. Handl.,* **169** (1943) 5-37.

93. O. Reiso, H. G. Overlie and N. Ryum, *Metall. Trans. A,* **21A** (1990) 1689-1695.

94. A. L. Wilson, PhD Dissertation, The Pennsylvania State University (2001).

95. K. Chattopadhyay, V. T. Swamy and S. L. Agrwala, *Acta Materialia,* **38** (1990) 521-531.

96. W. T. Kim and B. Cantor, *Acta Materialia,* **42** (1994) 3045-3053.

97. M. G. Hall and C. W. Haworth, *Acta Materialia,* **18** (1970) 331-337.

98. J. R. Frade and M. Cable, *J. Am. Ceram. Soc.,* **77** (1994) 999-1004.

99. B. P. Burton, J. E. Osburn and A. Pasturel, *Phys. Rev. B,* **45** (1992) 7677-7683.

100. P. A. Korzhavyi, A. V. Ruban, A. Y. Lozovoi, Y. K. Vekilov, I. A. Abrikosov and B. Johansson, *Phys. Rev. B,* **61** (2000) 6003-6018.

101. L. M. Pike, Y. A. Chang and C. T. Liu, *Acta Mater,* **45** (1997) 3709-3719.

102. C. L. Fu, Y. Y. Ye, M. H. Yoo and K. M. Ho, *Phys. Rev. B,* **48** (1993) 6712.

103. B. Meyer and M. Fahnle, *Phys. Rev. B,* **59** (1999) 6072.

104. A. Alavi, A. Y. Lozovoi and M. W. Finnis, *Phys. Rev. Lett.,* **83** (1999) 979.

105. C. Wagner and W. Schottky, *Z. Physik. Chem. B,* **11** (1930) 163.

106. P. E. Blöchl, *Phys. Rev. B,* **50** (1994) 17953.

107. G. Kresse and J. Joubert, *Phys. Rev. B,* **59** (1999) 1758.

108. M. J. Mehl, J. E. Osburn, D. A. Papaconstantopoulos and B. M. Klein, *Phys. Rev. B,* **41** (1990) 10311-10323.

109. F. Birch, *J. Geophys. Res.,* **83** (1978) 1257.

110. P. Nash and O. Kleppa, *Journal of Alloys and Compounds,* **321** (2001) 228-231.

111. B. Bai and G. S. Collins, in *High-Temperature Ordered Intermetallic Alloys VIII, MRS Symposia Proceedings No. 552* M. J. Mills, Ed. (Materials Research Society, Pittsburgh, 1999) pp. KK8.7.1-6.

112. K. F. McCarty, J. A. Nobel and N. C. Bartelt, *Nature,* **412** (2001) 622-625.

113. N. Rusovic and H. Warlimont, *Phys. Status Solidi,* **44** (1977) 609.

114. T. Davenport, L. Zhou and J. Trivisonno, *Phys. Rev. B,* **59** (1999) 3421-3426.

115. H. Okamoto, *J. Phase Equil.,* **14** (1993) 257-259.

116. J. L. Smialek and R. F. Hehemann, *Metall. Trans.,* **4** (1973) 1571-1575.

VITA

Chao Jiang was born on November 20, 1977. He graduated from Central South University, Changsha, China in 1996 with a B.S. degree in Materials Science and Engineering. He continued his graduate study at the same univerity and got his M.S. degree in Materials Science and Engineering in 1999. He then joined the Pennsylvania State University, University Park, PA, to pursue his Ph.D. degree in Materials Science and Engineering. He is a member of The Minerals, Metals and Materials Society (TMS). Listed below are his publications during his Ph.D. study:

1. C. Jiang and Z. K. Liu, "Thermodynamic Modeling of the Indium-Palladium System", Metall. Trans. A, 33 (2002) 3597-3603.
2. C. Jiang and Z. K. Liu, "Computational Investigation of Constitutional Liquation in Al-Cu Alloys", Acta Materialia, 51 (2003) 4447-4459.
3. C. Jiang, C. Wolverton, J. Sofo, L. Q. Chen and Z. K. Liu, "First-Principles Study of Binary Bcc Alloys using Special Quasirandom Structures", 69 (2004), 214202, Physical Review B.
4. C. Jiang, L. Q. Chen and Z. K. Liu, "First-Principles Study of Constitutional Point Defects in B2 NiAl Using Special Quasirandom Structures", submitted to Physical Review B.